UNIVERSIDAD NACIONAL AUTÓNOMA DE MÉXICO
PROGRAMA DE MAESTRÍA Y DOCTORADO EN INGENIERÍA
INGENIERÍA ELÉCTRICA – TELECOMUNICACIONES

IMPLEMENTATION OF MACHINE LEARNING TECHNIQUES TO OPTIMIZE
THE GROUND SEGMENT FOR HIGH THROUGHPUT SATELLITE SYSTEMS IN
Q/V BAND

T E S I S
QUE PARA OPTAR POR EL GRADO DE:
DOCTOR EN INGENIERÍA

PRESENTA:
IVÁN ANDRÉS CORNEJO GAIBOR

TUTORES PRINCIPALES
DR. SALVADOR LANDEROS AYALA, FI-UNAM
DR. JOSÉ MARÍA MATÍAS MARURI, FI-UNAM
COMITÉ TUTOR
DR. VÍCTOR RANGEL LICEA, FI-UNAM
DR. RAMÓN MARTÍNEZ RODRÍGUEZ-OSORIO, GR-UPM

CIUDAD DE MÉXICO, NOVIEMBRE 2020

JURADO ASIGNADO:

Presidente: Dr. Víctor Rangel Licea

Secretario: Dr. Miguel Moctezuma Flores

1er. Vocal: Dr. José María Matías Maruri

2do. Vocal: Dr. Salvador Landeros Ayala

3er. Vocal: Dr. Ramón Martínez Rodriguez-Osorio

Lugar donde se realizó la tesis: FACULTAD DE INGENIERÍA, UNAM.

TUTOR DE TESIS:

DR. SALVADOR LANDEROS AYALA

FIRMA

To my parents, Iván and Lourdes, for their endless love and encouragement.
To my loving wife, María Fernanda, for her support and patience.
Thank you for making it possible.

Acknowledgements

Abstract

Rain attenuation events are one of the most important drawbacks in satellite communications, impairing directly on satellite link availability. For this reason, it is necessary to foresee rain events in order to avoid an outage of the satellite link. However, the lack of rainfall database hinders the development of a reliable prediction method. In this thesis, we implement an alternative method to generate rain attenuation time-series in the Q/V band for a specific geographic location based on the recommendation of the International Telecommunication Union. With the computed rain-attenuation data, we propose and develop a method to predict rain attenuation events based on deep learning techniques without appealing to complex mathematical models. To be specific, we implement the Long-short term memory network, which is a Machine Learning technique based on supervised learning. Each model is trained and validated by computational experiments, employing statistical metrics to find the most accurate and reliable models. The outcomes of the prediction model are employed and discussed to compare with other related methods and models. In addition to the evaluation of the proposed method, we find that our method could be notably able to improve mechanisms for switching either data traffic or satellite links in order to increase the satellite-link availability.

For this purpose, two methods were proposed to optimize the ground network by the implementation of the deep learning method as well as another method based on the Markov chain. The smart-predictive method is based on the developed deep learning model, where the predictions of the rain attenuation and the carrier-to-noise and interference time series are able to detect, in advance, when one or more gateway feeder uplinks are going to be affected by the rain, so that the smart method can foresee the switching between the affected nominal gateway and an available redundant gateway. This mechanism is applied to all gateways of the ground network so that it is possible to find the number of nominal and redundant gateways needed for outperforming the minimum required availability of 99.9%.

The second method, in essence, employs the same principle but using the Markov chain to find a stationary distribution, which allows us to know the time spent of each state according to its nominal gateway or redundant gateways in the process, in addition to the switching probability between them. The obtained results are discussed and compared with another well-known method to define the ground network scheme, finding a ground network more efficient, lower complexity, and with a lower number of gateways, that take part in the data managing of the satellite system.

Contents

List of Figures

List of Tables

Mathematical Notation

Note: the vectors are denoted by bold lowercase letters whereas the matrices are expressed by bold uppercase letters.

$[N]$ the set $\{1, 2, \ldots, N\}$

$\boldsymbol{x}$ a dataset

$\wedge$ logical conjunction, if statement

$\lfloor x \rfloor$ the floor of a scalar x

$\vee$ logical disjunction

$\mathbb{R}$ the set of real numbers

$\mathbb{U}$ an interval $[0, 1]$

$\mathbf{E}\{\cdot\}$ the mathematical expectation of a random variable

$\mathbf{X}$ a Matrix

$\mathbf{x}$ a vector

$\mathbf{x} \odot \mathbf{y}$ the Hadamard product (element-wise product of either vectors or matrices)

$\mathbf{x}^{(i)}$ the i-th example (input) of a dataset

$\mathbf{X}^{\mathsf{T}}$ the transpose of matrix $\mathbf{X}$

$\mathbf{X}_{:,i}$ the column i of matrix $\mathbf{X}$, (a column vector)

$\mathbf{X}_{i,:}$ the row i of matrix $\mathbf{X}$, (a row vector)

$\mathrm{Var}\{\cdot\}$ the variance of a set of data, σ^2

$|\, x\, |$ absolute value of a scalar x

$\nabla_{\mathbf{X}} y$ the matrix derivatives of y with respect to $\mathbf{X}$

$\nabla_x y$ the gradient of y with respect to x

$\pm\mathbb{U}$ an interval $[-1, 1]$

$\Pr\{\cdot\}$ the probability of a random event

$\rightarrow$ prepositional logic, if ... then ...

$\sigma\{\cdot\}$ the standard deviation of a set of data

$\{0, 1\}$ the set containing 0 and 1

$f(\cdot)$ the general form of the mathematical function

$J_n(\cdot)$ the Bessel function of the n kind

$m\{\cdot\}$ the mean of a set of data

Q complementary cumulative normal distribution

Q^{-1} inverse complementary cumulative normal distribution

$s(t)$ continuous signal, where t is the independent variable

$s[k]$ discrete signal, where k is the independent variable

x a scalar (real or integer)

x_i the element i of a vector $\mathbf{x}$, with indexing starting at 1

$X_{i,j}$ the element i, j of matrix $\mathbf{X}$

Nomenclature and Units

A_c the coverage area, [km²]

A_h the area of the hexagon cell, [km²]

A_i the rain attenuation in the i-th site

A_{offset} the parameter that adjusts the time-series to match the probability rain, [dB]

BW_T total-bandwidth available, [Hz]

Cp_i the capacity of the satellite link, b/s

Cp_T total-capacity available, [b/s]

D distance, [km]

DL the download traffic, [b/s]

D_{ant} the diameter of satellite antenna, [m]

E the signal's average power

$EIRP_{sat}$ the effective isotropic radiated power from satellite antenna, [dBW]

$E_s/\mathcal{N}_0$ the energy per symbol to noise power spectral density, [dB]

F the focal length of the parabolic-reflector-antenna, [m]

$Freq_{s-E}$ the frequency on the space-Earth (s-E) path, [Hz]

G/T antenna gain-to-noise-temperature, [dB/K]

$G_r(\theta)$ the relative gain of the antenna, [dB]

G_{TX} the transmitter-antenna gain, [dBi]

H the offset of the parabolic-reflector-antenna center, [m]

HPA_{sat} the high power amplifier of the satellite in Ka-band, [W]

K the total number of samples, the K-dimensional Euclidean space

LNA low noise amplifier, [W]

MT_{ii} the monthly mean total rainfall data, [mm]

N number of GWs on the Ground Segment

N_b the number of the beams

N_p the potential for polarization reuse

N_{ii} the number of days of each month

N_{sb} the number of the frequency sub-bands

PL the path loss from either s-E or E-s, [dB]

P_a conditional joint probability that the attenuations exceed a_1 and a_2, respectively

P_i the probability of occurrence in the i-th site

P_i^{rain} the annual probability of rain (%) in the i-th site, a.k.a P_{0_i}

P_r joint probability that it is raining at both sites

$P_{0_{ii}}$ the monthly probability of rain, [%]

P_{out} the total probability of a system outage

P_{sw} the switching probability

R the range between HTS and GW, [km]

R_i solution of P_i^{rain} for the i-th site

R_p the rainfall rate exceeded for the desired probability of exceedance, [mm/h]

$R_{0.01}$ the annual rainfall rate data exceeded for 0.01% of an average year, [mm/hr]

R_{sw} the switching rate

S_{avail} the total available spectrum, [Hz]

S_{eff} the spectral efficiency, [b/s/Hz]

T_s the time interval between samples

T_{ii} the monthly mean surfaces temperatures, [K]

T_{sw} the interval between switching instants

UL the upload traffic, [b/s]

$\Gamma_{k,i}$ the k-th value of CNR matrix, $\mathbf{\Gamma}$, according to the i-th feeder link of GW

α the learning rate

α_i phase component of the communication channel for the i-th GW feeder link

$\bar{N}$ number of nominal gateways on the Ground Segment

$\bar{P}$ number of redundant gateways on the Ground Segment

β the parameter that describes the time dynamics, $[s^{-1}]$

β_1 the linear decay factor

β_2 the quadratic decay factor

ℓ the number of iteration

ϵ the small constant in order to avoid division by zero

γ_{cs_i} clear sky CNR for the i-th GW feeder link

κ Boltzmann's constant, $1.380\,649 \times 10^{-23}$ [J/m]

λ the wavelength of the frequency band used in a specific satellite link, [m]

$\mathbf{C}_t$ the collection of all cell state at time step t

$\mathbf{D}$ the distance matrix between pair of locations

$\mathbf{H}_t$ the collection of all hidden state at time step t

$\mathbf{P}$ the state transition matrix

$\mathbf{W_d}$ the weights matrix of the dense layer

$\mathbf{W_h}$ the recurrent weights matrix, $\mathbf{W_{h}}_f, \mathbf{W_{h}}_i, \mathbf{W_{h}}_o$

$\mathbf{W_x}$ the input weights matrix, $\mathbf{W_{x}}_f, \mathbf{W_{x}}_i, \mathbf{W_{x}}_o$

$\mathbf{\Theta}_{\mathcal{D}}$ the concatenation matrix of the dense layer (weights and biases)

$\mathbf{\Theta}_{\mathcal{L}}$ the concatenation matrix of the LSTM layer (weights and biases)

$\mathbf{b_d}$ the bias vector of the dense layer

$\mathbf{b}$ the bias vector of the LSTM layer, $\mathbf{b}_f, \mathbf{b}_i, \mathbf{b}_o$

$\mathbf{c}_t$ the stacked cell states at time step t

$\mathbf{h}_t$ the stacked hidden states at time step t

$\mathcal{D}$ the mathematical function of a dense layer

$\mathcal{F}$ the deep learning model

$\mathcal{I}_i(\phi)$ the function that describes the nature of the interference at the i-th beam, [dB]

$\mathcal{L}_{\mathcal{U}}$ the mathematical function of a LSTM layer

$\mathcal{L}$ the mathematical function of a single LSTM cell

$\mathcal{N}_i$ the noise variance at satellite interface for the i-th GW feeder link

$\mathcal{S}$ the mathematical function of a LSTM multi-layer

ν the system availability, where ν_i is the feeder uplink availability of each NGW

ω the angle that ranges from 0 (beam center) to $\theta_{BW}/2$ (beam edge), [deg]

ϕ the angle between the point T and the center of the i-th beam, [deg]

ψ_B the bisector angle of parabolic-reflector-antenna, [deg]

ψ_C the ψ_f aims to the aperture center at the point C, [deg]

ψ_L the lower angle of parabolic-reflector-antenna, [deg]

ψ_P the angle from the lower edge of dish to feed pointing direction, [deg]

ψ_U the upper angle of parabolic-reflector-antenna, [deg]

ψ_f the angle of feed-antenna-pattern, [deg]

ψ_s the half of the angle subtended of parabolic-reflector-antenna, [deg]

ρ_a the correlation factor for the conditional joint probability

ρ_r the correlation factor for the joint probability

σ_g the gate function activation based on the sigmoid function

θ_0 the beam diameter at the triple beam crossover, [km]

θ_c the closest spacing between beam centers reusing the same frequency, [km]

θ_r the closest spacing between the reuse-beam edges, [km]

θ_s the spacing between adjacent-beam centers, [km]

θ_{3dB} the angle subtended by the half-power points of the main lobe, [deg]

θ_{BW} Beamwidth in degrees, [deg]

ξ_{th} the CNIR threshold

ζ the value of the carrier-to-interference, [dB]

a_i the attenuation threshold in the i-th site, [dB]

c_t the cell state at time step t

c_u the cell candidate of the LSTM block

d_0 GEO distance of 35786 [km] above Earth's surface

f_g the forget gate of the LSTM block

h the offset distance of the parabolic-reflector-antenna, [m]

$h_i[k]$ the kth value of the communication channel for the i-th GW feeder link

h_t the hidden state at time step t

i_g the input gate of the LSTM block

ii the month numbers

k index of each sample

m the number of dataset's examples

n the integer number

$n(t)$ the white gaussian noise process

o_g the output gate of the LSTM block

p the probability of the rain

p_d the desired average annual probability of exceedance

r_c the coverage radius of spot beam, [km]

ro roll-off parameter, [%]

t_{ii} the monthly mean surfaces temperatures, [°C]

v_ℓ the moving average

$\Xi_{k,i}$ the k-th value of CNIR matrix, $\mathbf{\Xi}$, according to the i-th feeder link of GW

$\boldsymbol{t}$ time in seconds, 1 [s]

$\mathbf{b/s}$ rate in bit per second, 1 [b/s]

$\mathbf{dB}$ decibels, 1 [dB]

$\mathbf{Gb/s}$ giga bit per second, 1×10^9 [b/s]

$\mathbf{GHz}$ giga Hertz, 1×10^9 [Hz]

Hz frequency in hertz, 1 [Hz]

km kilometers, 1×10^3 [m]

km² square kilometers, 1×10^6 [m²]

m distance in meters, 1 [m]

Mb/s mega bit per second, 1×10^6 [b/s]

MHz mega Hertz, 1×10^6 [Hz]

mm millimeters, 1×10^{-3} [m]

mW milli watts, 1×10^{-3} [W]

Tb/s tera bit per second, 1×10^{12} [b/s]

W power in watts, 1 [W]

Abbreviations and Acronyms

5G Fifth generation wireless technology for digital cellular networks

a.m.s.l. Height above mean sea level

ACI Adjacent Carrier Isolation factor

ACM Adaptive Coding and Modulation

ADAM Adaptive Moment Estimation Optimizer

ARIMA Autoregressive Integrated Moving Average

BRASILSAT Brazilian communications satellite

BSS Broadcast Satellite Service

CIR Carrier-to-interference ratio

CNIR Carrier-to-noise and interference ratio

CNR Carrier-to-noise ratio

DVB Digital Video Broadcasting

DVB-RCS2 DVB - Return Channel Satellite, Second Generation

DVB-S2X DVB - Second Generation, Extensions

E-s Earth-to-space satellite communication link

EHF Extremely high frequency

EI the edge illuminations which can be both upper and lower, [dB]

EIRP Effective Isotropic Radiated Power

EoC the beam End-of-Coverage

EUTELSAT European Telecommunications Satellite Organization

FMT Fade Mitigation Technique

FRF Frequency Reuse Factor

FS Fixed Service

FSL Free Space Loss

FSS Fixed Satellite Service

FT the feed edge tapers which can be both upper and lower, [dB]

GEO Geostationary Orbit

GPU Graphics Processor Units

GS Ground Segment

GW Gateway Station

HD High Definition Video

HDFSS High-Density application in the Fixed Satellite Services

HPA the High Power Amplifier

HTS High Throughput Satellite

i.i.d Independent and identically distributed random variables

IDU Indoor Unit

IoT Internet of Things

ITU International Telecommunication Union

LDPC Low-Density Parity-Check

LHCP Left Hand Circularly Polarized

LSTM Long Short-Term Memory

M-APSK M-ary Amplitud and Phase-Shift Keying modulation

M-PSK M-ary Phase-Shift Keying modulation

M-QAM M-ary Quadrature Amplitude Modulation

M2M Machine-to-machine communication

MAE Mean Absolute Error

MBA Multiple Beam Antenna

MF-TDMA Multiple-Frequency Time Division Multiple Access

MODCOD Modulation and Coding Scheme

modem Modulator and Demodulator device

MS Mobile Service

MSS Mobile Satellite Service

NCC Network Control Center

NGSO Non-geostationary-satellite orbit systems

NGW Nominal Gateway

ODU Outdoor Unit

PGW Redundant or Backup Gateway

QoS Quality of Service

R-Squared Coefficient of determination, R^2

R2 ITU Region 2

ReLU Rectifier-Linear-Unit Activation Function

RF Radio Frequency

RHCP Right Hand Circularly Polarized

RMSE Root Mean Squared Error

RMSProp Root Mean Square Propagation

s-E space-to-Earth satellite communication link

SaaS Software as a Service

SatCom Satellite Communication

SELU Scaled-Exponential-Linear-Unit Activation Function

SFTSS Standard Frequency and Time Signal-Satellite

SGD Smart Gateway Diversity

SNN Self-Normalizing Neural Networks

SSL Spherical Spreading Loss, [dB]

TDMA Time Division Multiple Access

TPU Tensor Processor Units

UHTS Ultra High Throughput Satellite Systems

ULPC Uplink Power Control

UT User Terminal

VSAT Very Small Aperture Terminal

XP$_{iso}$ Cross-Polar Isolation factor

Chapter 1

Introduction

The thesis is focused on the performance analysis of the ground segment (GS) architecture for a new generation of satellite communications (SatCom) systems. Nowadays, the current requirements of throughput and broadband to users are huge so that the traditional communication infrastructures need to expand their resources and capabilities to cover the service demand. This main idea is also applied to SatCom systems in order to increase their capacity and to become an efficient solution to carry data traffic. Thus, new technological challenges emerge, providing an important research frame for the network architecture on GS. This chapter presents the state-of-the-art related to the problems arisen with the new satellite technology, specifically in areas involved in the feeder link design, multiple beam satellite systems, the frequency reuse, interference evaluations, availability, and reliability. Further, the chapter also brings out the main objectives of the thesis to study the aforementioned areas.

1.1 Traditional Broadband Satellite Systems

A traditional broadband satellite system provides communication services in remote areas wherein the terrestrial infrastructures do not reach them, especially in rural areas. The services offered by a broadband satellite system range from Internet access to multimedia services [1, 2]. Figure 1.1 depicts the architecture of a traditional broadband satellite system. Each network component accomplishes a specific role in the broadband satellite architecture. However, the satellite GS network has not undergone a major change in its architecture, but there are some parameters to take into account which are explained in the following subsections in detail [3].

- **Satellite:** The broadband satellite is placed in a geostationary orbit (GEO) in order to cover a wider area. Also, the GEO satellite is able to connect a gateway station (GW) to the user terminals (UTs) using radio frequency (RF) links (feeder and user links). This link connection is also known as bent-pipe satellite architecture, however, it is important to note that the amplification and frequency translations are only executed by satellite onboard processing.
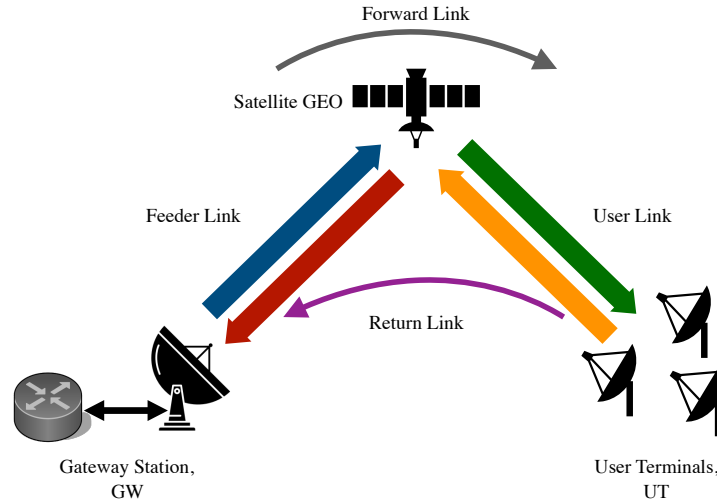
Figure 1.1: Architecture of a broadband satellite system.

- **Gateway Station:** The gateway (GW) station is capable of transmitting and receiving data. That is, the GW is responsible for controlling, managing and operating data traffic to and from user terminals (UT), via satellite links. In satellite networks, GWs are also known as gateway earth stations. Further, the GS network architecture can be made up of multiple GWs when the gateway diversity is considered necessary.

- **User Terminal:** The user terminal (UT), also referred to as user earth station, is a two-way broadband terminal, i.e., the UT can both transmit and receive data to and from the satellite employing a very small aperture terminal (VSAT). Moreover, the UT is a device that consists of two main units, the indoor unit (IDU) and the outdoor unit (ODU) [1]. The ODU is made up of the antenna, the RF transmitter, and one or more RF receivers. Meanwhile, the IDU contains the modulator and demodulator (modem), and the interface to the local network.

- **Feeder Link:** It is a RF link between the GW and satellite. The feeder link consists of both uplink and downlink. Currently, feeder links work in Ka-band[1] for broadband satellite systems.

- **User Link:** The RF link between the satellite and UTs is also known as the user link, which is made up of both uplink and downlink. It is important to mention that time division multiple access (TDMA) [1] and multi-frequency time division multiple access (MF-TDMA) [1,5] are employed to access from satellite to UTs and vise versa. Not only do the feeder link uses Ka-band but also the user link.

---

[1]The Ka-band is a frequency band of millimeter waves ranges from 17.70–21.20 GHz for downlink, whereas from 24.75–30.00 GHz for uplink. Both frequency ranges are available for ITU Region 2 (R2), [4].

- **Forward Link:** The link from GW towards UTs is described as the forward link. The forward link is also called the end-to-end link, which includes uplink of the feeder link, satellite, and downlink of the user link. Therefore, a GW transmits data to the UTs via the forward link. In this work, the digital video broadcasting (DVB), with its standard (DVB-S2X), is employed by the forward link to communicate from GW to UT [6].

- **Return Link:** On the other hand, the link from UT towards the GW is named as return link, which is made up of the uplink of the user link, satellite, and downlink of the feeder link. The UT transmits RF signals to the GW by using the DVB-RCS2 standard, which has the specification for the return link where the data traffic flow from UT to GW [7].

1.2   Multiple Spot Beam Satellite Systems

Satellite systems have been an efficient solution to cover remote and rural areas due to their ubiquitous links. Nevertheless, it is very tough to compete with terrestrial communications because the transmitted bit has a high cost so that it is necessary to reduce the cost by increasing the total capacity of the satellite systems [8]. Most of the satellite systems solely cover a large area by using a single beam, especially in L^2 , C^3 and Ku^4 bands.

Although the area is entirely covered by a single beam, the system capacity is limited as well as its efficiency. Currently, modern SatCom systems have multiple spot beams which increase the system capacity by using frequency reuse among beams. This architecture is also known as multiple beam architecture which is inspired by traditional cellular networks. Therefore, the inter-beam interference must be maintained within the typical values and admissible limits in order to achieve high spectral efficiency on the satellite link.

It is important to note that the latest satellite systems are at the technological cutting edge to cover a region by generating multiple spot beams. This means that satellites have multiple beam antennas (MBA). Reflector MBAs are usually used for SatComs due to their excellent RF performance in terms of coverage gain and the carrier-to-interference ratio (CIR), payload simplicity, reduced cost, and mature technology. These MBAs are classified into three types: (a) single reflector with a single feed per beam, (b) single reflector with over-lapping feed clusters, and (c)

---

[2]The L band is a frequency band in the radio spectrum from 1–2 GHz. The mobile satellite services use L band carriers where the downlink ranges from 1518.0–1559.0 MHz, 2180.0–2200.0 MHz, and 2483.5–2500.0 MHz, whereas the uplink ranges from 1610.0–1660.5 MHz, 1668.0–1675.0 MHz, and 2000.0–2025.0 MHz, [4].

[3]The C band in communication satellites uses the frequency band from 3.40–4.20 GHz and 4.50–4.80 GHz for the downlink, whereas the uplink ranges from 5.091–5.250 GHz and 5.850–7.075 GHz. Both frequency ranges are available for ITU region 2 (R2), [4].

[4]The Ku band in communication satellites uses the frequency band from 10.70–12.70 GHz for the downlink, whereas the uplink ranges from 12.70–13.25 GHz, 13.75–14.80 GHz, and 15.43–15.63 GHz. Both frequency ranges are available for ITU region 2 (R2), [4].

multiple reflectors with a single element per beam, [9]. In particular, the reflectors are generally offset-fed parabolic reflectors where the feed elements are horns.

Thus, Type (a) MBA has a straightforward architecture, where the reflector is illuminated by a dedicated feed in order to generate a beam pattern due to radiating the radio waves reflected from the antenna. This technique offers both good isolation and high radiation efficiency between the different beams. Type (b) MBA design needs low-level beamforming networks to provide element sharing among beams and beam combining functions. In fact, Type (b) antenna is usually used for mobile satellite services at low frequencies such as L-band and S-band[5].

Finally, Type (c) MBA is made up of multiple reflectors where each reflector is illuminated with its own feed array. These apertures are either 3 or 4 units, which are independent of each other. Here, each feed horn generates a single beam, therefore, the feed is able to provide optimal illumination on the reflector. Type (c) MBAs are often used at frequency bands such as the Ku band, Ka-band, and Extremely High Frequency (EHF) band.

At the satellite, each beam is generated by a specific feed horn, where the beams with the same frequency sub-bands are radiated from the same reflector. That is, each frequency sub-band corresponds to a segment (also known as a color), consequently, the frequency-reuse scheme in the MBA is usually known as either three-color or four-color schemes. Figure 1.2 details the architecture of a satellite system with a 4-color frequency-reuse scheme.

Particularly, a 4-color scheme is defined by partitioning the available frequency and polarization resources into four segments (colors), i.e, each color belongs to half the available bandwidth and one polarization. It is important to mention that frequency-reuse schemes employ the circular polarization, i.e., right hand circularly polarized (RHCP) and left hand circularly polarized (LHCP), therefore, it is available 2 polarization resources. Currently, these modern SatComs are also known as high throughput satellite (HTS) systems.

1.3 Evolution of High Throughput Satellite Systems

The evolution of HTS systems has outperformed many stages since the appearance of the first broadband satellite system in 2005 [10], improving impressively its capacity in order to increase both the coverage area and the quality of service (QoS) requirements of the end-user. Figure 1.3 compares the capacity of some HTS systems in different years. For instance, Spaceway 3 with 24 spot beams has a capacity of 10 Gb/s. Echostar XVII has 60 spot beams and a capacity of 120 Gb/s, whereas Echostar XIX has 120 spot beams and a capacity of 200 Gb/s. Spaceway 3, Echostar XVII, and XIX are part of the Hughes® HTS constellation which has the latest Jupiter™ System technology for broadband satellite access [11,12]. KA-SAT is part of the EUTELSAT fleet which has a capacity of 90 Gb/s and 82 spot beams [13]. By 2021 the Echostar

---

[5]The S-band is part of the microwave band in the electromagnetic spectrum, whose frequency band ranges from 2.0–4.0 GHz [4].
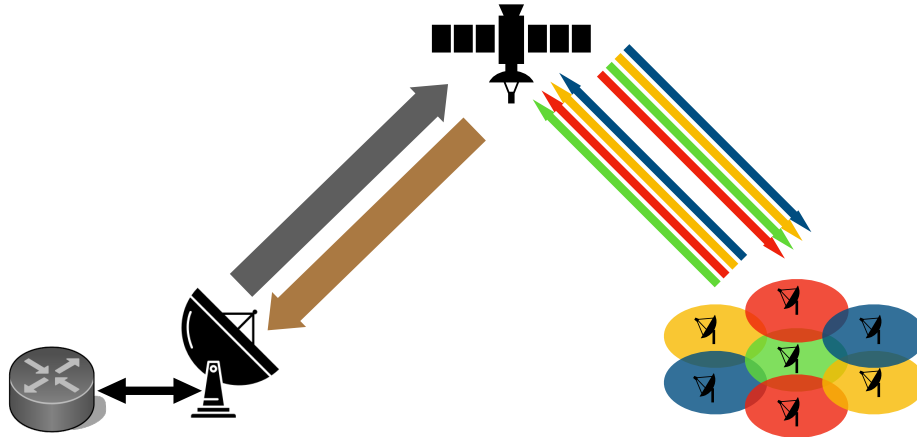
Figure 1.2: Architecture of a multiple spot beams satellite system with 4-color frequency reuse scheme.

XXIV will have been launching with a capacity up to 500 Gb/s and multiple spot beams in Ka-band.
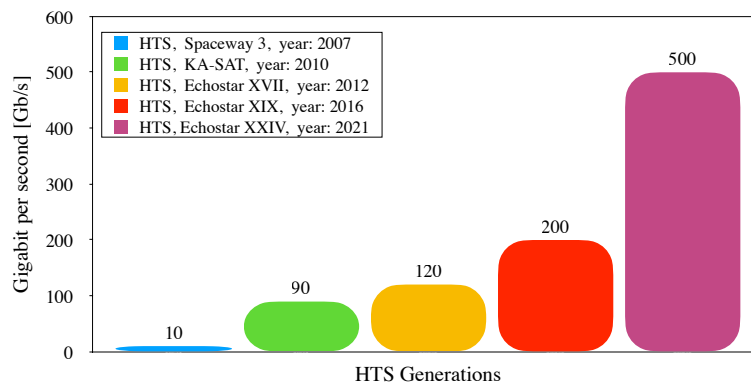
Figure 1.3: Capacity Evolution of HTS systems.

From 2021 onwards, it is estimated that next-generation HTS systems will require capacity equal to or greater than 1 Tb/s, which will reduce the cost per transmitted bit. However, the bandwidth is limited due to the lack of available spectrum in the Ka-band. In the following section, three alternatives are detailed in order to overcome the spectrum constraint and technical limitations, which are given an excellent background for this research.

1.4 State-of-art in current HTS systems

1.4.1 Feeder Link Design in Q/V band

As stated above in Section 1.3, the capacity of HTS systems is continually increasing due to the demand for data traffic. Therefore, it is necessary to design a reliable feeder link in terms of higher bandwidth and frequency bands. A first alternative is to move the feeder link from the Ka-band to the Q/V band[6] whose bandwidths are available for satellite communications [4, 8, 14]. It is important to mention that the feeder link needs more available spectrum, for this reason, up to 5 GHz are available for both feeder uplink and feeder downlink, respectively. As a result, the whole Ka-band spectrum is feasible for the user link, i.e., 3.50 GHz are available for both user uplink and user downlink, respectively. Indeed, it is a very important solution for satellite operators, however, the feeder link turns into a very susceptible link due to the heavy rain attenuation [8, 15]. Although the fade mitigation technique (FMT) is used as an uplink power control (ULPC), it can only compensate a few decibels (dB) during short-term fades.

For this reason, it is necessary to design a Q/V band feeder link with availability in excess of 99.9% [16]. Thus, multiple GWs are used by using transmit diversity in order to achieve the required availability [13, 14]. This design of feeder links must be reliable so that each feeder link can operate in its corresponding GW, therefore, it is a key-feature in the development of this research.

1.4.2 Aggressive Frequency Reuse

As already mentioned, current HTS systems use a 4-color multiple spot beam structure in order to increase the total capacity in the satellite system. Nevertheless, each beam utilizes only 1/4 of the total resources in terms of frequency and polarization, therefore, it is not an efficient scheme. Nowadays, a lot of research aims to improve the conventional 4-color frequency-reuse scheme in order to achieve full frequency reuse with advanced systems [14, 17–19]. Although the main idea is that each beam can utilize the whole available resources, this leads to an increase in the inter-beam interference among the adjacent beams.

In fact, it has been explored 3-color and 4-color frequency reuse scheme with both simple and double polarization [18], as well as the incidence in the interference among user and feeder links. To sum up, it is important to know the affectation of these interferences in the Q/V band feeder link in order to guarantee communication from/to the HTS system.

---

[6]Q/V band ranges from 37.50–42.50 GHz for the downlink (Q band), whereas the uplink (V band) ranges from 42.50–51.40, GHz. These frequency bands are within the EHF band for ITU region 2 (R2), [4].

1.4.3 Ground Segment Architecture

In Section 1.4.1, it was mentioned that the transmit diversity was necessary to achieve an availability greater than 99.9% on the feeder link. That is, the ground segment architecture is made up of a number of GWs, which are interconnected by terrestrial links in order to generate an ease routing of feeder link data. Therefore, this architecture is used in diversity way in order to mitigate fades on the feeder link of each GW. The main advantage of this mechanism is when a GW experiences either feeder link outage or reduced capacity, then an available GW receives all data traffic by using terrestrial links [14].

Consequently, some diversity scheme models have been studied by several researchers, one of them has been the $1 + 1$ diversity scheme [20, 21], where a nominal GW was backed up by another redundant GW. Although this architecture is acceptable for low/medium throughput systems, it is not efficient for HTS systems, where high capacities and tens of GWs are necessary.

Further, another transmit diversity scheme is also known as the $N + P$ scheme, which has been studied in [8, 14, 22–26]. This scheme is made up of N active or nominal gateways (NGW), and P idle or redundant gateways (PGW). Whether one of the NGWs is in outage, whole the traffic from the affected NGW is rerouted to one of the PGWs by a switching mechanism. Furthermore, the smart gateway diversity (SGD) is another scheme that has been studied in [22, 26]. The main difference between the SGD and the $N + P$ scheme diversity is that the SGD does not need redundant PGWs, but its disadvantage is when one or more NGWs are in outage, that is, the throughput of users served is reduced by either the GW or GWs affected.

However, this disadvantage can be overcome by adding more capacity for each GW in order to support other GWs in case of an outage. Therefore, GWs need to be oversized in terms of capacity. Moreover, the user terminals require a level of intelligence, increasing the complexity of the network. In this thesis, the research is only focused on the $N + P$ scheme, therefore, the contributions are associated with this scenario.

1.5 Objectives

The objectives of this thesis are to design, allocate, develop and optimize the GS by cutting edge techniques for HTS systems. That is, the main focus on this thesis is related to an adequate design of the Q/V band feeder uplink, allocating properly the GW sites on the GS, and developing techniques to optimize the network architecture on the GS. In this section, a brief description of specific objectives are given as follows,

- **Q/V band Feeder Uplink Design:** As already mentioned, the Q/V band is very susceptible to both rain attenuation and propagation effects. Therefore, the Q/V band feeder uplink must be designed to achieve high reliability in order to provide new broadband services on the user link of an HTS system. Each Q/V band feeder uplink provides a high bandwidth communication to/from the HTS. Therefore, this thesis is focused on the design of a reliable feeder uplink for

each GW in order to operate over the typical availability of an $N + P$ diversity scheme on the GS.

- **Allocating GW Sites on Ground Segment:** An important part of this research is to analyze if the site for each GW is adequate to be considered in an $N + P$ diversity scheme. The performance of this scheme is assessed by a correlated rain fading channel and its impact on the distance between two or more GWs. For this reason, the GW sites are modeled by implementing a dynamic rain attenuation model. It is important to mention that the rain attenuation model is brought by the recommendations of the International Telecommunication Union (ITU). As a result, the total outage probability is determined by a theoretical analysis for each $N + P$ simulated scenario. Also, the effects of other parameters related to the dynamic rain attenuation model are observed and studied by several $N + P$ simulations.

- **Optimization Techniques for Ground Segment Architecture:** Very few works that studied the $N + P$ scheme were developed by deep mathematical analysis. However, it is very important to develop a rigorous mathematical analysis in order to detect and to find the switching-rate performance between N and P GWs. The switching parameter is a key-feature in the system model, which relates directly to the outage probability in the HTS system. Therefore, the lack of a rigorous analysis taking into account dynamic rain attenuation characteristics, spatial correlation between GWs, and switching rate requirements, it motives strong research on the GS for multiple GWs using the Q/V band. In this context, machine learning techniques are implemented in this study in order to optimize the total number of GWs, which are assured efficient switching with an optimal $N + P$ scheme.

1.6 Methodology

In this thesis, the quantitative method is employed by mathematical analysis, statistical data, and computational techniques. The scientific rigor is based on the reliability and validity of data. For this purpose, several models are developed by statistical analysis to later be handled and submitted to an experimental method by advanced computational techniques based on machine learning algorithms. In this context, due to the lack of a historical rainfall database in the gateway locations to be used in this thesis, the ITU Recommendations provides rain attenuation time-series by statistical analysis. Thus, these rain attenuation time-series are employed to develop, generate, train, and validate rain-attenuation models by machine learning algorithms in order to predict rain attenuation events in advance. Currently, computational tools offer up high performance and speed to run and solve complex algorithms.

All found data will be collected and their statistical/computational treatment results as well as all relevant results in relation to the research problem of this thesis. These outcomes are also employed to propose, design, and evaluate an efficient

switching mechanism for sizing and optimizing the ground network segment by smart techniques based on the predictive rain-attenuation models and the Markov process.

Finally, all obtained data from this research are depicted and tabulated by figures and tables which explain and show the nature and behavior of the outcomes from each process in more detail. However, all results are discussed in their respective sections by comparative and analytic methods with other models and researches.

1.7 Contributions of the Research

The contributions of this thesis include modeling the rain attenuation over satellite feeder links, predictive modeling based on machine learning algorithms, and developing optimization techniques for the Ground network segment. A brief description of each of them is detailed as follows:

- The satellite feeder link is modeled in this thesis by mathematical analysis. Further, other models are added to the feeder link model to generate an artificial rain-attenuation dataset for specific geographic locations. This model is essential to find and understand the availability of each gateways station in addition to the ground network availability.

- The available electromagnetic spectrum, maximum capacity, and schemes of the frequency reuse of the high throughput satellite system were approached by theoretical and numerical analysis. For this reason, code scripts using Matlab and Python were developed in this thesis in order to find and evaluate the results in these processes.

- The rain-attenuation dataset is employed to train and validate predictive models by the implementation of Machine Learning algorithms in order to determine in advance when the feeder link is impaired by the heavy rain. For this purpose, code scripts using Python/Tensorflow were developed in this thesis to find and explain the model outcomes.

- Finally, an efficient switching scheme mechanism for the $N+P$ gateway scenario is presented in this thesis. By using predictive rain-attenuation models obtained from Machine Learning algorithms and the Markov Chain process, it is possible to define the number of redundant gateways is necessary to maintain the network availability above 99.9%. These processes optimize the Ground network segment as a function of the number of redundant gateways.

1.8 Thesis Structure

This thesis is organized as follows: Chapter 2 explains the main background concepts and system models to implement in this thesis. In Chapter 3, the quantification of multiple spot beams and the total capacity of the HTS system is detailed. Chapter 4 evaluates the interferences in frequency reuse by using offset-parabolic-reflector

antennas. The deep learning models, developments, implementations, results, and discussions are provided in more detail by Chapter 5. In Chapter 6, the optimization of the Ground Segment is presented and discussed by smart and predictive switching mechanisms. Finally, Chapter 7 concludes this research and its proposals, in addition to remarking about future research studies. Contributions and scientific productions of this thesis are also detailed.

Chapter 2

System Models for the Ground Segment

2.1 Introduction

In this chapter, system models that are used throughout this thesis are introduced and explained. Systems models were briefly mentioned in Chapter 1, showing a problem statement in each case. Therefore, each system model is described in mathematical detail providing an excellent background to the different objectives of this thesis.

The feeder uplink model is presented in Section 2.1, where the mathematical analysis and the main impairments in the feeder uplink are minutely discussed. Moreover, the system parameters are provided to find and discuss the problems that are associated with the Q/V band uplink budget. In Section 2.2, the spatial correlation model is described. This model is based on the ITU-R recommendations, which is used to determine a minimum separation between GWs in order to avoid the rain attenuation in two sites or more at the same time. The dynamic rain attenuation model is presented in Section 2.3, which also is based on an ITU-R recommendation. This model is used to obtain the rain attenuation in each site of the GS. Finally, the $N + P$ diversity model is explained in Section 2.4 which is implemented on the GS by simulated scenarios to understand the behavior of the network.

2.2 Feeder Uplink Model

Each gateway station (GW) is distributed and separated from other GWs by a distance of D km on the ground segment (GS). Hence, each satellite feeder uplink belongs to its respective i-th GW, transmitting the signal $s_i(t)$, where $s_i(t)$ is a function that varies with time. It is important to mention that i indicates the i-th GW site. In this thesis, the modeled satellite-link is the feeder uplink which is between the i-th GW and the high throughput satellite (HTS). It is worth noting that the feeder uplink operates at the EHF band because there is more available spectrum. The frequency band is ranged from 42.50–51.40 GHz which is also known as the V band. This model is based on the Gharanjik's feeder link model [21], but with slight

differences according to the aim of this study.

To begin with, the average power of the feeder-uplink signal is defined as

$$E_i = \mathbf{E}\{|s_i(t)|^2\}, \text{for } i = 1, 2, \ldots, N, \tag{2.1}$$

where N is the number of GWs on the ground network. Thus, the set of GWs, $\{1, 2, \ldots, N\}$, can also be represented by the set notation $[N]$. The continuous signal $s_i(t)$ is sampled by measuring the value of the continuous function every T_s seconds or minutes, i.e., it depends on the sampling period to be used. As a result, the sampled signal is given by $s_i[k]$, where k is the index of each sample, being an integer value, i.e., $k = 1, 2, \ldots, K$, whereas K is the total number of samples, and T_s is the time interval between samples or sampling period. In this case, the numeric value of the k-th number in the sequence is equal to the value of the continuous signal, $s_i(t)$, at time $t = kT_s$, i.e., $s_i[k] = s_i(kT_s)$. By using this analysis, the communication channel between an i-th GW and the satellite at $t = kT_s$ can be represented by

$$h_i[k] = |h_i[k]|e^{j\alpha_i}, \text{for } i = 1, 2, \ldots, N, \tag{2.2}$$

where α_i is the phase component. Moreover, the channel amplitude $|h_i[k]|$ is estimated by a signal beacon from the satellite. The channel expression is obtained from [25], which is explained in more detail. Further, the clear sky carrier-to-noise ratio (CNR) for each feeder uplink at the satellite receiver is expressed as

$$\gamma_{cs_i} = \frac{C_i}{\mathcal{N}_i} = \frac{E_i}{\mathcal{N}_i}\frac{1}{1 + ro}, \text{for } i = 1, 2, \ldots, N, \tag{2.3}$$

where $\mathcal{N}_i$ is the noise variance at satellite interface and ro is the roll-off parameter. Here, the roll-off factor is a measure of the excess bandwidth of the filter, that is, the bandwidth occupies beyond the Nyquist bandwidth. For this purpose, the roll-off value, either 5% or 10%, is obtained from the Digital Video Broadcasting Second Generation with Extensions (DVB-S2X) standard [6]. It is important to note that the DVB-S2X standard is considered as the baseline air interface for the forward link. Based on the previous equations, the actual CNR for the feeder uplink between an i-th GW and the satellite at $t = kT_s$ for $k = 1, 2, \ldots, K$, is denoted by

$$\Gamma_{k,i} = |h_i[k]|^2\frac{C_i}{\mathcal{N}_i} = |h_i[k]|^2\gamma_{cs_i}, \text{for } i = 1, 2, \ldots, N, \tag{2.4}$$

where each value of $\Gamma_{k,i}$ can be stored in a column vector $\mathbf{\Gamma}_{:,i}$ for $i = 1, 2, \ldots, N$, which defines a point in a K-dimensional space called Euclidean space denoted by $\mathbb{R}^K$, therefore, the matrix of CNR can be expressed by $\mathbf{\Gamma} \in \mathbb{R}^{K \times N}$. However, this case is only when the feeder uplink is not affected by either interferences or weather impairments, such as rain, clouds, and fog. Therefore, it is necessary to obtain the carrier-to-noise and interference ratio (CNIR) using both the CNR and the carrier-to-interference ratio (CIR). It is important to mention that CIR is one of the most serious challenges due to the fact that interferences degrades the signal quality, impairing directly to communication system. The CIR can also be represented

by the symbol ζ.

The total CIR, ζ_T, directly impacts on the feeder uplink, which is made up of the co-channel interference, ζ_{co}, adjacent channel interference, ζ_{adj}, and the intermodulation interference, ζ_{im}, [8]. The ζ_T can be calculated by

$$\frac{1}{\zeta_T} = \frac{1}{\zeta_{co}} + \frac{1}{\zeta_{adj}} + \frac{1}{\zeta_{im}} \tag{2.5}$$

Finally, the CNIR for $k = 1, 2, \ldots, K$ is defined as

$$\Xi_{k,i} = \frac{\Gamma_{k,i} \cdot \zeta_T}{\Gamma_{k,i} + \zeta_T}, \text{for } i = 1, 2, \ldots, N, \tag{2.6}$$

where each value of $\Xi_{k,i}$ is also stored in a K-dimensional column vector, $\mathbf{\Xi}_{:,i} \in \mathbb{R}^K$ for $i = 1, 2, \ldots, N$. The matrix of CNIR is given by $\mathbf{\Xi} \in \mathbb{R}^{K \times N}$. To sum up, the signal quality is defined by the CNIR value for each k-th sample, therefore, this is a good measure to know whether the feeder uplink can be able to transmit to the satellite receiver, or if the weather conditions affect the feeder link, then it can not transmit the signal to the satellite, degrading the spectral efficiency on the channel.

2.2.1 Parameters of the Feeder Uplink

Many parameters are involved in the performance of the Q/V band feeder uplink. Table 2.1 shows the basic propagation parameters for the feeder uplink between a GW station and the HTS system. These parameters were used in link simulations for each GW station of the GS. Currently, the BRASILSAT B4 satellite is positioned at 92.0° West. Although the satellite has exceeded its lifespan (19 years), the orbital position is only used for HTS simulation purposes of HTS systems. Furthermore, the specific parameters of the system and the link budget are detailed in Chapters 3 and 4.

Table 2.1: Basic Propagation Parameters

Feeder Uplink	Values
Frequency	50 GHz
Orbital Position	92.0°W
Orbit	GEO, $d_0 = 35786$ km
Polarization	LHCP, RHCP
Boltzmann's constant	$\kappa = 1.380\,649 \times 10^{-23}$ J/m

In order to determine elevation, azimuth, and range between each GW station and the HTS system, it is essential to use geographical coordinates for each site (latitude and longitude) [1,2]. With these parameters, the transmitter antenna of each GW is adequately pointed towards the HTS receiver antenna.

It is important to mention that each feeder uplink is also affected by the user downlinks, therefore, each forward link (Feeder Uplink + User Downlink) is analyzed and calculated. Thus, it is assumed as a mixed Ka and Q/V band solution [8, 14, 18].

Although the study of the Ka-band user link is not the aim of this thesis, it is necessary to know its implication in this system. The Ka-band implications are approached in more detail in Chapter 4.

2.3   Spatial Correlation Model

Spatial correlation is a measure that analyzes the relationship between near spatial units. For this purpose, the Recommendation ITU-R P.1815 indicates the method to obtain the spatial correlation model, which is able to estimate the correlation of rain rate to determine differential rain attenuation on satellite paths between the HTS and multiple locations on the surface of the Earth [27]. The Recommendation ITU-R P.618 includes the spatial correlation model [28], (See §2.2.4.1), whose objective is generally to calculate propagation data for the design of Earth-space telecommunication systems. Here, a set of ITU Recommendations were neatly employed to implement the obtained spatial-correlation-model for our study [29–35]. It is important to mention that the use of Recommendations ITU-R 1815 and ITU-R 618 are valid for antenna elevations above $10°$, frequencies up to 55 GHz, and site separations D between 0 and at least 250 km.

Log-normal distribution of rain intensity and rain attenuation level are assumed by the differential rain attenuation method [27, 28]. Thus, this method determines the joint probability (%) that the attenuation on the path to the first site is greater than the attenuation threshold (a_1) and the attenuation on the path to the second site is greater than the attenuation threshold (a_2). The probability is the product of two joint probabilities and is expressed as,

$$\Pr\{A_1 \geq a_1, A_2 \geq a_2\} = 100 \times P_r \times P_a, \tag{2.7}$$

where P_r is the joint probability that it is raining at both sites, P_a is the conditional joint probability that the A_1 and A_2 attenuations exceed a_1 and a_2, respectively [27]. In general terms, the attenuation threshold for every i-th site can be denoted as a_i. The discrete rain attenuation process and the channel gain, for each i-th site and $k = 1, 2, \ldots, K$, are related as

$$A_i[k] = -10 \log_{10} |h_i[k]|^2, \text{ for } i = 1, 2, \ldots, N \tag{2.8}$$

Both probabilities (P_r and P_a) are complementary bivariate normal distributions, which are expressed as

$$P_r = \frac{1}{2\pi \sqrt{1 - \rho_r^2}} \int_{R_1}^{\infty} \int_{R_2}^{\infty} \exp\left[-\left(\frac{r_1^2 - 2\rho_r r_1 r_2 + r_2^2}{2(1 - \rho_r^2)} \right) \right] dr_2 \, dr_1, \tag{2.9}$$

$$P_a = \frac{1}{2\pi \sqrt{1 - \rho_a^2}} \int_{\frac{\ln a_1 - m_{\ln A_1}}{\sigma_{\ln A_1}}}^{\infty} \int_{\frac{\ln a_2 - m_{\ln A_2}}{\sigma_{\ln A_2}}}^{\infty} \exp\left[-\left(\frac{b_1^2 - 2\rho_a b_1 b_2 + b_2^2}{2(1 - \rho_a^2)} \right) \right] db_2 \, db_1, \tag{2.10}$$

where r_1 and r_2 are independent variables of the function P_r whereas b_1 and b_2 are independent variables of the function P_a. The correlation coefficients ρ_r and ρ_a are respectively denoted as

$$\rho_r = 0.7 \exp\left(-\frac{D}{60}\right) + 0.3 \exp\left[-\left(\frac{D}{700}\right)^2\right], \tag{2.11}$$

$$\rho_a = 0.94 \exp\left(-\frac{D}{30}\right) + 0.06 \exp\left[-\left(\frac{D}{500}\right)^2\right]. \tag{2.12}$$

In Eq. (2.11) and Eq. (2.12), D is the distance between two sites in km, whereas in Eq. (2.9), the thresholds R_1 and R_2 are the solutions of rain probability (P_i^{rain}) for a particular i location, which is calculated from step 3 of Annex 1 in [29] by the following equation:

$$P_i^{rain} = 100 \times Q(R_i) = 100 \times \frac{1}{\sqrt{2\pi}} \int_{R_i}^{\infty} \exp\left(-\frac{r^2}{2}\right) dr, \text{for } i = 1, 2\ldots, N. \tag{2.13}$$

Once obtained P_i^{rain} (%), it is possible to calculate the threshold R_i using the inverse complementary cumulative normal distribution, Q^{-1}, as follows $R_i = Q^{-1}(P_i^{rain}/100)$. Finally, the parameters $m_{\ln A_1}$, $m_{\ln A_2}$, $\sigma_{\ln A_1}$ and $\sigma_{\ln A_2}$ are computed by fitting each i-th site rain attenuation, A_i, versus probability of occurrence, P_i, to the log-normal distribution:

$$P_i = P_i^{rain} Q\left(\frac{\ln A_i - m_{\ln A_i}}{\sigma_{\ln A_i}}\right), \text{for } i = 1, 2, \ldots, N. \tag{2.14}$$

This method is described in §2.2.1.1 from [28].

   Nevertheless, the inclusion of spatial correlation makes the analysis very complex so that it is necessary to assume spatially independent and identically distributed (i.i.d) links. Indeed, a typical diversity scheme of multiple gateways has a few tens of GWs dispersed over the GS, where each i-th site is only separated a few tens kilometers from each other. In a sense, the rain attenuation at each i-th site must be uncorrelated to avoid link outages in two or more GWs at the same time. Therefore, applying the correlation coefficient, ρ_a, by Eq. (2.12), it is possible to find uncorrelated distances for $\rho_a \leq 0.1$ [25]. Figure 2.1 depicts the correlation coefficient ρ_a between two sites, where the correlation drops to 0.1 at a distance of 80 km, therefore, it takes solely a few tens of kilometers to carry through the decorrelation of rain attenuation.

2.4   The Dynamic Rain Attenuation Model

In the Q/V band, the link impairment is mainly related to the rain attenuation, which is traditionally modeled and validated by using a log-normal distribution [36]. Eq. (2.8) expresses the relation between the rain attenuation and the channel gain, where $h_i[k]$ is the communication channel between a GW and the HTS. However, the rain attenuation is a time-varying process so that it is necessary to model the dynamic
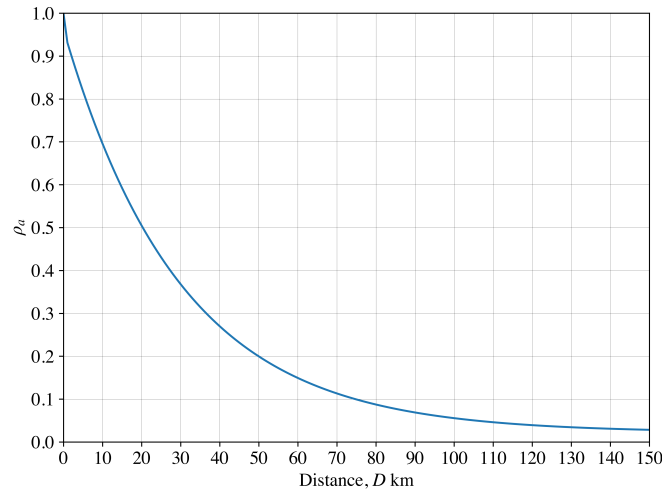
Figure 2.1: The correlation coefficient, ρ_a, between two sites separated by a distance of D km.

behavior of the rain attenuation.

Despite that several time-series models to synthesize rain attenuation samples with temporal properties have been studied and proposed, only one model has been stood out [3]. This model was based on the Maseng-Bakken model [37], which was implemented as a new recommendation by the International Telecommunication Union (ITU), ITU-R P.1853 [38].

The ITU Recommendation P.1853 details how the time series synthesis method generates a time series that reproduces the spectral characteristics, fade slope and fade duration statistics of rain attenuation events. Also, the statistics of the inter-fade duration are reproduced but solely within individual events of the rain-attenuation. Figure 2.2 depicts the block diagram of this process, for this purpose, the rain attenuation, $A(t)$, is synthesized from the white-Gaussian-noise discrete process, $n(t)$. Here, it is important to mention that $A(t)$ is a continuous signal. In this model, the white-Gaussian-noise is filtered by a low-pass filter, which is transformed from a normal distribution to a log-normal distribution in a memoryless nonlinearity, in addition to being calibrated to match the desired rain-attenuation statistics [38].

The time-series synthesizer is made up of five features, where m is the mean of the log-normal rain attenuation distribution, σ is the standard deviation of the log-normal rain attenuation distribution, p is the probability of rain, β is the parameter that describes the time dynamics (s^{-1}), and the A_{offset} that adjusts the time-series to match the probability of rain (dB). This time-series synthesizer is employed in this thesis, therefore, the following procedure is the basis for effective implementation.
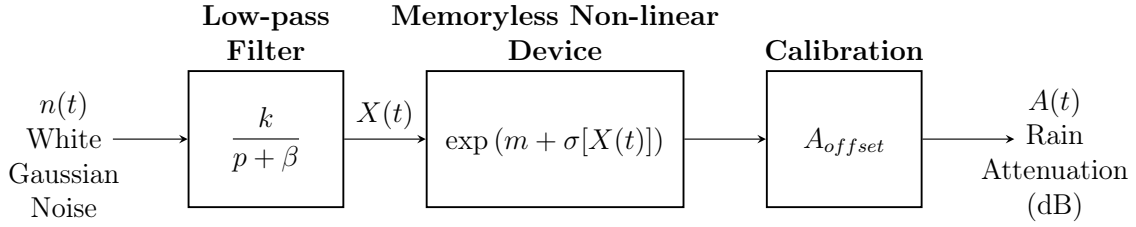
Figure 2.2: Block diagram of the rain attenuation time series synthesizer, ITU-R P.1853.

2.4.1 Procedure to Synthesize the Rain Attenuation Time-series

The following step-by-step method is used to synthesize the attenuation time-series $A_i(kT_s)$ for $k = 1, 2, \ldots, K$, and for $i = 1, 2, \ldots, N$, which is based on the ITU Recommendation P.1853 [38]. The suggested method is apportioned as follows:

A. Estimation of m and σ

The parameters m and σ are obtained by the cumulative distribution of rain attenuation vs. probability of occurrence. In most cases, the development process is extremely difficult due to the lack of rain attenuation statistics from measured data *in situ*. However, the ITU Recommendation P.618 [28] provides excellent rain attenuation data prediction for Earth-space paths, which are also known as artificial rain attenuation data. Therefore for the path and frequency of interest, it was performed a log-normal fit of the rain attenuation vs. probability of occurrence by using the ITU Recommendation P.1057, where the step-by-step procedure to approximate a complementary cumulative distribution by a log-normal complementary cumulative distribution is described in detail [39]. As a result of this procedure, it was possible to obtain m and σ.

B. Low-pass filter parameter

The parameter is configured as, $\beta = 2 \times 10^{-4} \ s^{-1}$

C. Attenuation offset

The attenuation offset for each i-th site is estimated by

$$A_{i_{offset}} = \exp\left[m + \sigma Q^{-1}\left(\frac{P_i^{rain}}{100}\right)\right], \text{for } i = 1, 2, \ldots, N \tag{2.15}$$

D. Time-series synthesis

The rain attenuation time-series, $A_i(kT_s)$, for $k = 1, 2, \ldots, K$, and for $i = 1, 2, \ldots, N$, is synthesized as follows:

- **Step D1:** A white-Gaussian-noise time-series, $n_i(kT_s)$, is synthesized for each i-th GW site, where $k = 1, 2, \ldots, K$, with $m\{n_i(kT_s)\} = 0$ and $\text{Var}\{n_i(kT_s)\} = 1$ at a sampling period, T_s. It is important to mention that the sampling period value can be modified, however, the default value is 1 s.

- **Step D2:** Set $X(0) = 0$

- **Step D3:** The noise time-series, $n_i(kT_s)$, for $k = 1, 2, \ldots, K$, is filtered by a recursive low-pass filter, which is expressed by

$$X_i(kT_s) = \rho X[(k-1)T_s] + n_i(kT_s)\sqrt{1+\rho^2}, \text{for } i = 1, 2, \ldots, N, \qquad (2.16)$$

  where $\rho = \exp(-\beta T_s)$.

- **Step D4:** $Y_i(kT_s)$ for $k = 1, 2, \ldots, K$, and for each i-th GW site, is defined as

$$Y_i(kT_s) = \exp[m + \sigma X_i(kT_s)], \text{for } i = 1, 2, \ldots, N \qquad (2.17)$$

- **Step D5:** The dynamic rain attenuation, $A_i(kT_s)$ (dB) for $k = 1, 2, \ldots, K$, and for each i-th GW site, is computed as follows

$$A_i(kT_s) = \max\lfloor Y_i(kT_s) - A_{i_{offset}}, 0\rfloor, \text{for } i = 1, 2, \ldots, N \qquad (2.18)$$

- **Step D6:** The first 200000 samples are discarded from the synthesized time-series which correspond to the filter transient. Here, rain attenuation events are represented by sequences where, for a consecutive number of samples, values are above 0 dB. Consequently, Eq. (2.8) can be replaced by Eq. (2.18) in order to simulate a dynamic rain attenuation. It is necessary to mention that Eq. (2.18) can be expressed as a discrete signal, $A_i[k]$, where each k-element of rain attenuation, $A_{k,i}$, can be stacked in a K-dimensional column vector, $\mathbf{A}_{:,i} \in \mathbb{R}^K$ for $i = 1, 2, \ldots, N,$. Finally, the matrix of rain-attenuation is given by $\mathbf{A} \in \mathbb{R}^{K \times N}$.

2.5 $N + P$ Diversity Model on Ground Segment

As was previously mentioned in Chapter 1, an important drawback was the seriously increased rain attenuation in the Q/V band compared with Ka-band. Therefore, site diversity is introduced in order to mitigate the impact of rain attenuation [22, 25, 26]. This kind of diversity model uses generally spatial diversity of the feeder links, which has feeder links spatially independent and identically distributed, i.i.d, as already mentioned in Section 2.2. As a result, there is a very small probability that all the

GWs experience heavy rain fading at the same time. However, if a GW is affected by the rain attenuation, another GW under clear sky conditions can take over the capacity from that affected GW [8, 14, 18, 26].

For this process to be possible, the network must have extra resources, e.g. extra GWs, which are also known as redundant or backup PGWs. In other words, this process is also known as the switching mechanism between NGWs and PGWs. The switching mechanism can be performed if a certain switching threshold is reached, which can be a capacity threshold, a carrier-to-noise and interference ratio (CNIR) threshold or a combination of these two cases. In summary, when the switching threshold is reached, the capacity of the NGW affected is transferred (handover) to another PGW with clear sky or in much better conditions [21, 23, 24].

Figure 2.3 shows the gateway diversity scheme to be used in this thesis, which is known as the smart gateway diversity technique 3 and is gathered from [26]. When there are good weather conditions, the nominal gateways (NGW_1 and NGW_2) use the total available bandwidth allowed by the ITU radio regulations [4], as shown in Figure 2.3a. However, when the feeder link of the NGW_1 is affected by a rain fading event, that capacity is taken over by the redundant gateway PGW_1, as illustrated in Figure 2.3b. Therefore, this model expresses adequately the $N + P$ diversity model, which has the following properties:

- **from the system aspect:** the system capacity does not degrade unless too many gateways are impacted at the same time. It is thus important to carefully select switching thresholds and carefully perform system dimensioning. End-to-end availability is improved;

- **from the user aspect:** user terminals served by the impacted gateway do not need to switch to a different carrier. They experience a short switching time because of switching traffic from one GW to the other [26].

Altogether, the $N+P$ model is used to establish a solid base for this thesis in order to approach from a mathematical point of view to the optimization of this model.
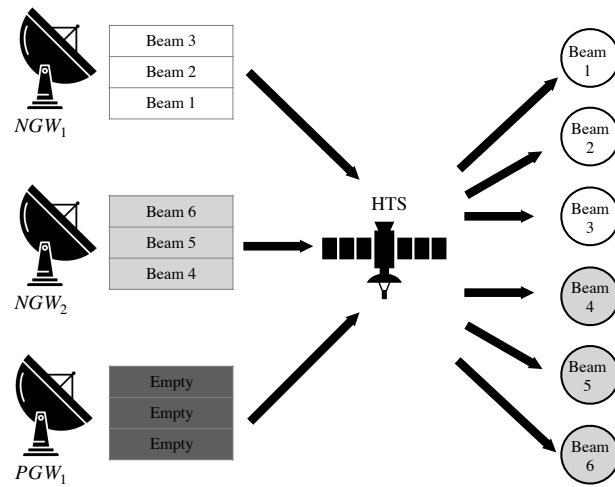
(a) Operation in clear sky conditions
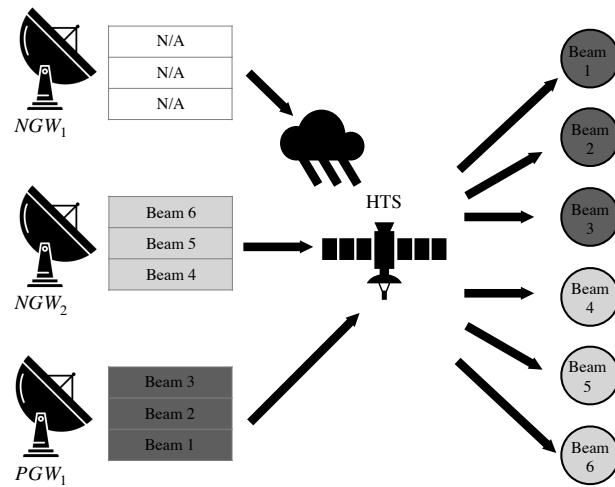
(b) Operation under rain conditions

Figure 2.3: Gateway diversity scheme with a redundant GW.

Chapter 3

Quantification of Multiple Spot Beams for HTS Systems in Ka and Q/V bands

3.1 Introduction

In this Chapter, it is proposed a methodology to quantify the necessary number of HTS spot beams in order to achieve a capacity of 1 Tb/s for the Latin America region by using an HTS system under ideal conditions. Firstly, a mix solution is proposed in order to obtain more available spectrum. Therefore, the Q/V band is used by the Feeder link whereas Ka-band is used by the User link. In this sense, two mechanisms are introduced to this system to find the precise number of spot beams for both Feeder and User links respectively. Moreover, traffic configurations are analyzed by simulations in order to project future needs in terms of capacity. The system capacity is important to supply multiple data services to/from UT such as HD streaming, Big Data, IoT, M2M, etc. At the end of this Chapter, it was assured the theoretical capacity for the HTS system in order to face the main challenges by 2021 and beyond.

3.2 Connectivity in Latin America: A Review

Latin America is one of the biggest regions in the world either in population or territory, however, there is a strong social, economic, and technological gap, influencing especially in the Internet connectivity in urban and rural areas with noteworthy differences. Based on the above, an HTS system could cover this region, close the current gap, and reach remotes areas where terrestrial infrastructures do not deploy their services due to economic and technological factors.

The Internet penetration rate is crucial to size any communication system so that it is also useful in an HTS system. In the last decade, the percentage of inhabitants that use the Internet has increased by 36% on average. In 2016 the 56% of inhabitants accessed to the Internet in Latin America [40]. Moreover, the Latin American region

is characterized by a high heterogeneity between countries. For instance, the number of households connected to the Internet grown by about 103% between 2010 and 2016, however, more than 50% of total households have no Internet connections. For the sake of brevity, the big economic differences between social classes are the reason for the lack of internet connections in Latin America, however, the thesis does not delve into this topic.

Thus, the countries with the highest growth rate of households connected to the Internet in the period 2010–2016 were Nicaragua, Guatemala, Honduras, and Bolivia, which had a lower Internet penetration rate at the beginning of the period. Costa Rica had the highest growth in the total Internet penetration of households (from 24% to 65%), as it is shown in Figure 3.1. There is a lot of difference between urban and
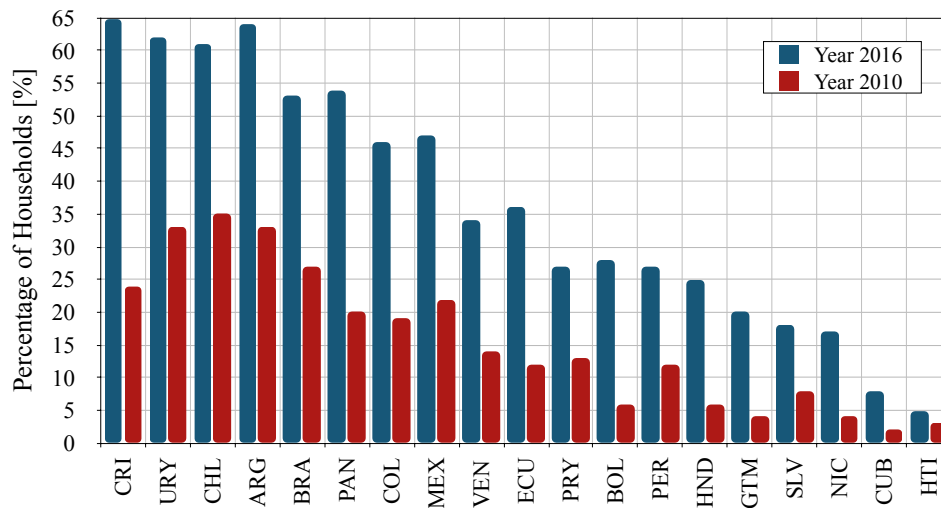
Figure 3.1: Percentage of households with Internet access per country [40].

rural zones in terms of households with an Internet connection. Figure 3.2 illustrates the high inequality between urban and rural households due to social and economic differences in the Latin America region in addition to higher costs of infrastructure deployment in rural areas than urban areas.

As a result, there were 18 million rural households without Internet access in the year 2016, whereas by the year 2020 there will be 20 million rural households without Internet access for all Latin America region. For this reason, it is necessary to reduce the social gap between urban and rural zones generating more opportunities in these areas [40].

Based on above analysis, it is convenient to use high throughput satellite (HTS) systems in order to cover remote zones where the terrestrial infrastructure cannot reach them and be able to face to the access demand (getting higher and higher). This satellite infrastructure can be used either as a high-performance backhaul or be part of a non-geostationary (NGSO) satellite fleet. No doubt this leads to new services and markets in satellite communications and other service providers, being mainly integrators of both Shared and 5G networks by the year 2020 [41–48].
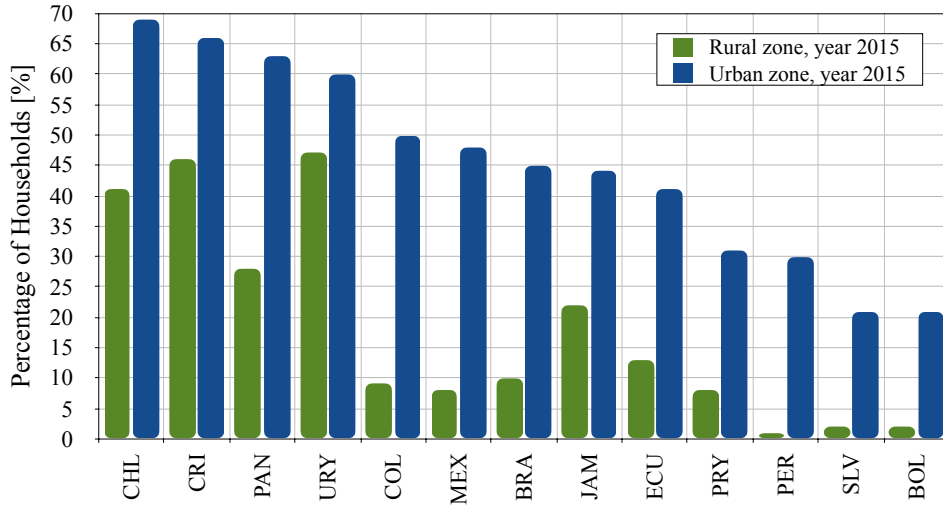
Figure 3.2: Percentage of households with Internet access per geographical zone [40].

3.3 Available Spectrum

Nowadays, the Ku-band does not have sufficient available spectrum for an HTS system, therefore, it is necessary to go to upper bands either the Ka-band or the novel Q/V band, providing enough spectrum in order to achieve a capacity of satellite system above 1 Tb/s. There are some satellite services assigned to the radio spectrum, for instance, Fixed Satellite Service (FSS), Mobile Satellite Service (MSS), Inter-satellite links, Space Research, Radioastronomy, Earth Exploration by Satellite, Standard Frequency and Time Signal-Satellite (SFTSS), and Broadcast Satellite Service (BSS). Also, the satellite services are sharing spectrum with other terrestrial services as Mobile Service (MS) and Fixed Service (FS) [4].

3.3.1 Ka-band Radio Regulations

The current generation of HTS systems is exclusively dedicated to using the Ka-band, where the downlink ranges from 19.70–20.20 GHz and the uplink ranges from 29.50–30.00 GHz. That is, there is an available bandwidth of 2×500 MHz given by ITU Region 2 (R2) [4]. The rest of the frequency allocations in Ka-band are sharing with other services that depend on regulations in each country and coordination between operators.

- **Downlink Frequency Bands:** This frequency band ranges from 17.70–19.70 GHz and shares services such as FSS, MSS, and BSS, however, in some countries could be different assignments so that it is necessary to have adequate coordination. The frequency band of 20.20–21.20 GHz is assigned to military services, therefore, it could be restricted in some countries. It is important to mention that both frequency bands of 18.30–19.30 GHz and 19.70–20.20 GHz are available for High-Density application in the Fixed Satellite Services (HDFSS), which enables to deploy a large number of earth stations (VSATs).

Table 3.1 indicates the frequency allocations for satellite downlink in Ka-band given by ITU Region R2 [4].

- **Uplink Frequency Bands:** In this case, the frequency band ranges from 24.75–25.25 GHz that is exclusively for FSS, therefore, this frequency band is not shared with other services. The frequency band of 27.00–29.50 GHz is shared with other services such as FS, MSS, and Space Exploration. Finally, both frequency bands of 28.35–29.10 GHz and 29.25–30.00 GHz are available for HDFSS. Table 3.2 indicates the frequency allocations for satellite uplink in Ka-band given by ITU Region R2 [4].

3.3.2   Q/V band Radio Regulations

In this case, it does not exist exclusive assignments for FSS services, but it requires coordination for each portion of the spectrum since the ITU suggests that each portion must be assigned to services such as FSS, BSS, MSS, FS, MS, radioastronomy, space research, and exploration.

- **Downlink Frequency Bands (Q band):** This Q band spectrum is divided into two frequency bands, where the first frequency band ranges from 37.50–39.50 GHz, sharing services such as FSS, FS, research, and space exploration. Meanwhile, the frequency band ranges from 40.00–42.50 GHz is sharing services such as FS, FSS, MSS, BSS, research, and space exploration so that this frequency band needs a lot of coordination between regulatory entities in each country. Table 3.3 shows the frequency band portions for satellite downlinks in the Q band for ITU Region R2 [4].

- **Uplink Frequency Bands (V band):** In contrast to the Q band, the V band is divided into three frequency bands, therefore, the first frequency band ranges from 42.50–43.50 GHz, which is shared by other services such as FSS, FS, and radioastronomy. The second frequency band is assigned to both FSS and FS, which ranges from 47.20–50.20 GHz, however, each regulatory entity could issue restrictions in this frequency band. Finally, the third frequency band ranges from 50.40–51.40 GHz, where its spectrum assignment is similar to the previous frequency band. Table 3.4 denotes the frequency band portions for satellite uplinks in the V band for ITU Region R2 [4].

As a result, in the Ka-band are available of 3.500 GHz of the spectrum for downlink and 3.500 GHz for uplink, whereas in the Q/V band are available 5.000 GHz of the spectrum for downlink and 5.000 GHz for uplink, respectively. In both cases, the availability must be subject to coordination from regulatory entities.

As stated above, a mixed solution was proposed in this Thesis, i.e., Ka-band was used for the User Link and the Q/V band was used for the Feeder Link. Nevertheless, it was not possible to use the entire available spectrum, therefore, it was assumed that the analysis was totally theoretical so that 3.000 GHz were available for both

Table 3.1: Frequency Allocations for Satellite Downlink in Ka-band, ITU Region R2 [4].

Ka-band Downlink	17.70–17.80 [GHz]	17.80–18.40 [GHz]	18.40–18.60 [GHz]	18.60–18.80 [GHz]	18.80–19.30 [GHz]	19.30–19.70 [GHz]	19.70–20.20 [GHz]	20.20–21.20 [GHz]	BW [GHz]
FSS(s-E)/BSS/FS	0.100								0.100
FSS(s-E)/FS		0.600	0.200		0.500	0.400			1.700
FSS(s-E)/Earth Exp. Sat./FS/Mobile/Space Research				0.200					0.200
FSS(s-E)							0.500		0.500
FSS(s-E)/MSS(s-E)/SFTSS								1.000	1.000
								Available Bandwidth	**3.500**

Note: Some bandwidths require coordination with other services, especially Fixed Services (FS).

Table 3.2: Frequency Allocations for Satellite Uplink in Ka-band, ITU Region R2 [4].

Ka-band Uplink	24.75–25.25 [GHz]	27.00–27.50 [GHz]	27.50–28.50 [GHz]	28.50–29.10 [GHz]	29.10–29.50 [GHz]	29.50–29.90 [GHz]	29.90–30.00 [GHz]	BW [GHz]
FSS(E-s)	0.500							0.500
FSS(E-s)/FS/Inter-Satellites/MSS		0.500						0.500
FSS(E-s)/FS/MSS			1.000					1.000
FSS(E-s)/Earth Exp. Sat./FS				0.600	0.400			1.000
FSS(E-s)/Earth Exp. Sat.						0.400	0.100	0.500
							Available Bandwidth	**3.500**

Note: Some bandwidths require coordination with other services, especially Fixed Services (FS).

Table 3.3: Frequency Allocations for Satellite Downlink in Q band, ITU Region R2 [4].

Q band Downlink	37.50–38.00 [GHz]	38.00–39.50 [GHz]	39.50–40.00 [GHz]	40.00–40.50 [GHz]	40.50–41.00 [GHz]	41.00–42.50 [GHz]	BW [GHz]
FSS(s-E)/FS/Space Research/MSS/Earth Exp. Sat.	0.500						0.500
FSS(s-E)/FS/MS/Earth Exp. Sat		1.500					1.500
FSS(s-E)/FS//MS/MSS/Earth Exp. Sat.			0.500				0.500
FSS(s-E)/FS//MS/MSS/Earth Exp. Sat./Space Research				0.500			0.500
FSS(s-E)/FS/BSS/MS/MSS					0.500		0.500
FSS(s-E)/FS/BSS/MS						1.500	1.500
						Available Bandwidth	**5.000**

Note: Some bandwidths require coordination with other services, especially Fixed Services (FS).

Table 3.4: Frequency Allocations for Satellite Uplink in V band, ITU Region R2 [4].

V band Uplink	42.50–43.50 [GHz]	47.20–50.20 [GHz]	50.40–51.40 [GHz]	BW [GHz]
FSS(E-s)/FS/MSS/Radioastronomy	1.000			1.000
FSS(E-s)/FS/MS		3.000	1.000	4.000
Available Bandwidth				5.000
Note: Some bandwidths require coordination with other services, especially Fixed Services (FS).				

the downlink and uplink in Ka-band, respectively. Finally, the feeder link employed only 4.000 GHz for the uplink (V band) and 4.000 GHz for the downlink (Q band), taking into account that it was an ideal case.

3.4 Satellite Link Design in Ka and Q/V bands

The satellite links can be designed and calculated by using traditional satellite-links calculations, i.e., the equations for free space loss (FSL), effective isotropic radiated power (EIRP), Range, CNR, etc., are the same for bands C, Ku, Ka, and Q/V [1, 2, 49, 50].

For this satellite link design, it must be taking into account that the sky is in clear conditions. This assumption is necessary to find the maximum limit of the satellite system. However, there are some losses on the path such as attenuation due to fog, clouds, and gases, but without considering the rain attenuation. Moreover, both directions forward link and the return link are analyzed separately and independently.

Despite the sky is in clear conditions, there are some losses on the path that affect the satellite link performance. For this reason, the following ITU-R Recommendations are included in this study:

- **ITU-R P.676:** Attenuation by atmospheric gases and related effects [51].

- **ITU-R P.834:** Effects of tropospheric refraction on radiowave propagation [52].

- **ITU-R P.840:** Attenuation due to clouds and fog [53].

It is important to mention that the found losses on the Earth-space (E-s) satellite links range from 0.5–4.0 dB, which do not affect strongly to satellite links. For this case, satellite links on the E-s path, i.e., satellite uplinks, operate at the V-band. As a result, the carrier-to-noise ratios (CNR) have reasonable power levels so that it is possible to estimate the carrier-to-noise and interference ratio (CNIR) using the carrier-to-interference ratio (CIR), as a value of 20 dB [18].

An initial estimation of capacity and system configuration can only be based on the bandwidth, spectral efficiency, frequency reuse, and polarization reuse. Therefore, the total bandwidth available (BW_T) and the total capacity (Cp_T) are obtained from [18] and are expressed as

$$BW_T = \frac{N_b N_p}{N_{sb}} S_{avail}, \tag{3.1}$$

and

$$Cp_T = BW_T S_{eff}, \tag{3.2}$$

where N_b is the number of the beams, N_p is the potential for polarization reuse, N_{sb} is the number of the frequency sub-bands, S_{avail} is the total available spectrum in the chosen direction, and S_{eff} is the spectral efficiency that is obtained from DVB-S2X.

Table 3.5: Frequency Reuse and Polarization Schemes [18].

Conf.	N_{sb}	N_p	Comments	Scheme
1F2P	1	2	Each spot beam is dual-polarization but it has no frequency reuse.	
3F1P	3	1	Beams are single-polarization and 3 frequency sub-bands (3-color scheme).	
3F2P	3	2	Beams are dual-polarization and 3 frequency sub-bands (3-color scheme).	
4F1P	4	1	Beams are single-polarization and 4 frequency sub-bands (4-color scheme).	
4F2P	4	2	Beams are dual-polarization and 4 frequency sub-bands (4-color scheme).	

Table 3.5 indicates the schemes that use different frequency sub-bands or/and polarizations for multiple spot beams (adjacent beams) on the HTS system. The use of these schemes is popular thereby reducing the interference levels by appropriate filtering and permitting reuse of a sub-band in a non-adjacent beam. The degree of frequency reuse is often described numerically by using a frequency reuse factor (FRF) [18]. It is conventional in frequency reuse to divide the frequency band into several sub-bands, which use different frequencies, usually 3, 4, 7, etc. These frequency sub-bands can be referred to as colors for simplicity, therefore, in this study, the system can have either three or four colors. Moreover, the polarization discrimination between the beams can be used in various patterns. In [18], the author has developed the nomenclature mFnP, who has described the use of m colors and n polarizations, of course, this nomenclature is employed throughout this thesis.

Furthermore, the antenna circular polarization is employed in this study, as a result, the module of the field is constant. It is important to note that circular polarizations are made up of two directions of the rotation field, left (counter-clockwise) and right (clockwise), also known as left hand circularly polarized (LHCP) and right hand circularly polarized (RHCP) respectively.

3.5 Radio Interfaces

In order to achieve high capacities for HTS systems, it is essential to have advanced radio interfaces that permit high performance in satellite links. Thereby, the DVB-S2X standard is used on the forward link [6], whereas the DVB-RCS2 standard is used on the return link [7].

The DVB-S2X standard has 39 modulation and coding schemes (MODCOD), whose modulations varying from QPSK (M-ary Phase-Shift Keying, M-PSK) to 256-APSK (M-ary Amplitud and Phase-Shift Keying, M-APSK) with different coding rates. Also, the standard uses Low-Density Parity-Check (LDPC) which is a linear error-correcting code for transmitting a message over a noisy transmission channel [54,55]. The roll-off can be either 5% or 10%, therefore, it is possible to have excellent spectral efficiency, that is, DVB-S2X has a 51.44% more spectral efficiency than the DVB-S2 standard [56].

On the other hand, the DVB-RCS2 standard uses M-ary Quadrature Amplitude Modulation (M-QAM) and M-PSK schemes, i.e., varying from QPSK to 16-QAM with two bursts, short and long. Moreover, the roll-off takes on 4 different values, which are 20%, 25%, 30%, and 35%. It is important to mention that each MODCOD has a particular coding rate and its error-correcting code is based on turbo-codes [57]. Table 3.6 indicates and compares the maximum spectral efficiencies for each DVB standard where both DVB-S2X and DVB-RCS2 MODCODs are used on the forward link and return link respectively.

Table 3.6: Maximum Spectral Efficiencies

Standard	MODCOD	Roll-off	Spectral Efficiency, [b/s/Hz]	DVB-S2X vs. DVB-S2
DVB-S2	32 APSK 9/10	20%	3.7109	–
DVB-S2X	256 APSK 3/4	5%	5.6199	+51.44%
DVB-RCS2	16 QAM 5/6	20%	2.1417	–

3.6 Methods to Calculate the Performance of Satellite Antennas

The trend is to have satellites of large dimensions, especially in communication capacity as well as size and weight. Indeed, in this thesis were implemented two

methods to calculate the performance of the satellite antenna, aiming to reduce the antenna size, therefore, the antenna is also reduced in weight and assured the desired cover. It is important to mention that if the beamwidth is larger, the power amplifier needs more power and a lower diameter of the antenna. However, the proposal is to use MBAs so that it is possible to reduce the beamwidth and to cover the same region using multiple spot beams. Therefore, there is lower consumption of energy on the satellite's power subsystem but higher coordination in the onboard processing for managing the satellite spot beams, in addition to higher size antennas. Consequently, the two evaluation methods for antenna performance are presented in the following subsections, where the first method is focused on the antenna size evaluation, whereas the second method is approached in the power amplifier performance in Ka-band.

3.6.1 First Method: Antenna Size Evaluation

In this process, the satellite-antenna size (D_{ant}) was numerically calculated by a loop process. The Q band is used in the space-Earth satellite-communication link (s-E), which is denoted by $Freq_{s-E}$. The s-E satellite downlink is established between the HTS and the GW (return link).

To begin with the method execution, the D_{ant} was either increased or decreased in steps of 1 mm until to find the desired beamwidth (θ_{BW}). Here, it was suggested that the θ_{BW} of the satellite antenna might be defined by a value of 0.20° in direction to GW [18]. As a result, the best diameter of the satellite antenna was fitted in 2.63 m by using the illumination law [19], therefore, it was assured a narrow beamwidth with a coverage radius (r_c) about 62.5 km. It is possible to compute r_c by using θ_{BW} and the s-E range (R). Finally, Method 1 is detailed in the pseudocode of the process to size the satellite antenna.

This method can be also applied to size the satellite antenna diameter in Ka-band, D_{ant}, which is a function of antenna beamwidth (θ_{BW}). In this case, the θ_{BW} must be less than 0.5°, therefore, the D_{ant} fluctuates in steps of 1 mm, which is very similar to the calculation process of antenna size in the Q band. In particular, the coverage radius (r_c) of the spot beams can be modified from 80–125 km by using different beamwidths that range from 0.26°–0.40° according to the ground-segment requirements.

3.6.2 Second Method: Calculations for Antenna Gain and EIRP

Here, it is possible to find the transmitter-antenna gain (G_{TX}) and the effective isotropic radiated power ($EIRP_{sat}$) for each spot beam in Ka-band. For this purpose, High Power Amplifier (HPA) was either increased or decreased by steps of 100 mW until reaching the maximum EIRP as a system threshold, whereas the second option was to modify the D_{ant} by steps of 1 mm until reaching the maximum EIRP allowed. As a result, the diameter of the satellite antenna (D_{ant}) was ranged from 2.62–4.10 m, and the HPA was set in 53.0 W, therefore, it was possible to calculate in different coverage cases and to choose the best option for the proposed system. Method 2 is

---

Method 1 Calculation of the Satellite Antenna Diameter

Input: D_{ant}, R, $Freq_{s-E}$
Output: D_{ant}, r_c
  1: $\theta_{BW} \leftarrow compute(Freq_{s-E}, D_{ant})$;
     {For Ka-band: $\leq 0.26°$–$0.40°$}
  2: **if** $(\theta_{BW} \leq 0.20°)$ **then**
  3:    **while** $(\theta_{BW} \leq 0.20°)$ **do**
  4:       $D_{ant} \leftarrow D_{ant} - 0.001$;
  5:       $\theta_{BW} \leftarrow compute(Freq_{s-E}, D_{ant})$;
  6:    **end while**
  7: **else**
  8:    **while** $(\theta_{BW} \geq 0.20°)$ **do**
  9:       $D_{ant} \leftarrow D_{ant} + 0.001$;
10:       $\theta_{BW} \leftarrow compute(Freq_{s-E}, D_{ant})$;
11:    **end while**
12: **end if**
13: $r_c \leftarrow compute(R, \theta_{BW})$;
14: **return** $[D_{ant}, r_c]$

---

detailed in the pseudocode of the process to calculate the satellite antenna size as a function of HPA, EIRP, $Freq_{s-E}$, and θ_{BW}. Moreover, if the EIRP levels exceed the permitted limit in the Q band, this method can be also implemented for satellite antennas in that frequency band.

3.7 Analysis and Quantification of Multiple Spot Beams for HTS Systems in Ka and Q/V bands: Numerical Results and Discussion

Primarily, the analysis to quantify the number of spot beams was based on the bandwidth, spectral efficiency, frequency reuse, polarization, EIRP levels, and data traffic rates. Generally, this first analysis provided a theoretical quantification for the HTS system, however, it was considered neither payload nor power subsystem of the HTS system, since it was not the purpose of this thesis.

As stated above, the scheme $N + P$ was implemented on the Ground Segment, also, the mixed solution was proposed where both Ka and Q/V bands were assigned to user and feeder links, respectively. It is important to mention that 1 Tb/s is the maximum capacity for this numerical analysis. Furthermore, the quantification of multiple spot beams was also evaluated by data-traffic-ratio scenarios at the feeder link. The traffic scenarios can be denoted by $[DL{:}UL]$, where DL is the download traffic and UL is the upload traffic.

Method 2 Calculations for Antenna Gain and EIRP

Input: $D_{ant}, R, option, Freq_{s-E}, EIRP_{max}, HPA_{sat}$

Output: D_{ant}, r_c, HPA_{sat}

 1: $G_{TX} \leftarrow compute(D_{ant}, Freq_{s-E})$;
 2: $EIRP_{sat} \leftarrow compute(G_{TX}, HPA_{sat})$;
 3: **switch** (*option*)
 4: **case** 1**:**
 5:    **while** $(EIRP_{sat} < EIRP_{max})$ **do**
 6:       $HPA_{sat} \leftarrow HPA_{sat} + 0.1$;
 7:       $EIRP_{sat} \leftarrow compute(G_{TX}, HPA_{sat})$;
 8:    **end while**
 9: **case** 2**:**
10:    **while** $(EIRP_{sat} < EIRP_{max})$ **do**
11:       $D_{ant} \leftarrow D_{ant} + 0.001$;
12:       $G_{TX} \leftarrow compute(D_{ant}, Freq_{s-E})$;
13:       $EIRP_{sat} \leftarrow compute(G_{TX}, HPA_{sat})$;
14:       $\theta_{BW} \leftarrow compute(Freq_{e-T}, D_{ant})$;
15:    **end while**
16: **default:**
17:    {This option does not exist}
18: **end switch**
19: $r_c \leftarrow compute(R, \theta_{BW})$;
20: **return** $[D_{ant}, r_c, HPA_{sat}]$

3.7.1   Orbital Position Analysis

In this thesis, several GWs were distributed in the Latin America region, that is, Mexico, Central America, The Caribbean, and South America. For this reason, the orbital position for the HTS system was crucial for this evaluation. The list of possible geographic coordinates for GW locations is provided in Appendix A.1.

First, the energy per symbol to noise power spectral density $(E_s/\mathcal{N}_0)$ must be calculated for each GW feeder uplink by ranging the orbital position from 0°–180° (west longitude). To find the best orbital position, the Monte Carlo Method is employed in this assessment [58], where a domain of possible inputs (window of orbital positions) is used to perform a deterministic computation of the inputs. Thus, each $E_s/\mathcal{N}_0$ is computed regarding the range of orbital positions. As a result, the best orbital position can be interpreted according to the best power levels, which are represented by a set-theoretic intersection. Table 3.7 shows the parameters used for the feeder uplink calculations which were obtained from [8, 13, 14, 18] in addition to the previously mentioned Methods.

In order to obtain the best spectral efficiency for each feeder uplink, the $E_s/\mathcal{N}_0$ levels must be above 20 dB due to the fact that the best MODCOD (256 APSK 3/4) of the DVB-S2X standard requires 19.57 dB of $E_s/\mathcal{N}_0$. Furthermore, the found $E_s/\mathcal{N}_0$ have a positive link margin of 2.5 dB above the reference of 13.5 dB [14]. Figure 3.3

Table 3.7: Feeder Uplink Parameters

HTS System		User Terminal (UT)		Gateway Station (GW)	
Parameter	**Value**	**Parameter**	**Value**	**Parameter**	**Value**
D_{ant} (Q band)	2.63 m	D_{ant} (Ka-band)	0.75 m	D_{ant} (V band)	5 m
D_{ant} (Ka-band)	4.10 m	LNA (Ka-band)	8.8 W	HPA (V band)	16 W
HPA (Q band)	15 W	G/T	20 dB/K		
HPA (Ka-band)	53 W				

depicts the $E_s/\mathcal{N}_0 \geq 20$ dB of each feeder uplink by using the Monte Carlo Method. Therefore, several valid orbital-positions were found from -102.0° to -50.0°, but only one orbital-position encompassed the best $E_s/\mathcal{N}_0$ levels of each feeder uplink.
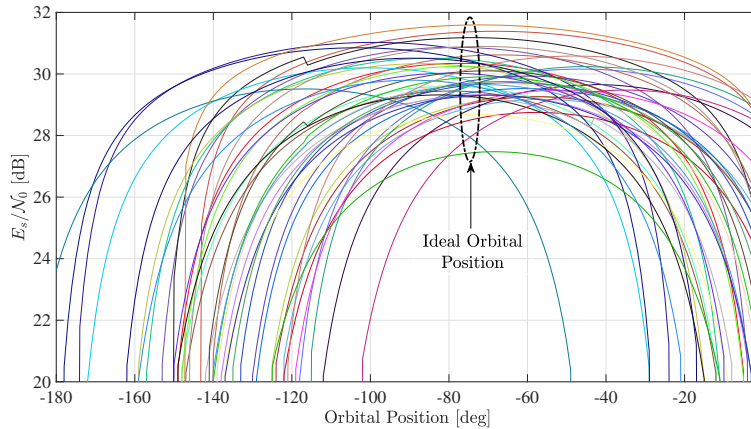
Figure 3.3: $E_s/\mathcal{N}_0$ for each feeder uplink using the Monte Carlo Method.

For this purpose, the Central Limit Theorem was applied to the orbital-position observations, which were obtained from the Monte Carlo Method. It is important to mention that each observation does not depend on the values of the other observations, therefore, the central limit theorem says that the distribution of the average is closely approximated by a normal distribution. Figure 3.4 depicts the normal distribution by using the central limit theorem, providing the best orbital position that is -74.1°. Even though -74.1° is the best orbital position in this evaluation, the range from -80.0° to -70.0° is also a good option for orbital positions due to the orbital positions are true 68% of the time within the 1-σ events. Finally, It is worth noting that the orbital positions must be negotiated with regulatory entities, however, these orbital positions are studied for theoretical purposes. All these calculations are made using computer codes, i.e., Matlab and Python scripts.

3.7.2   Quantification of Multiple Spot Beams

In order to find the number of spot beams, Eq. 3.1 and Eq. 3.2 were used by taking as reference the total capacity of 1 Tb/s. Thus, the traffic behavior was considered in this analysis where 5 data-traffic-ratio scenarios were proposed and
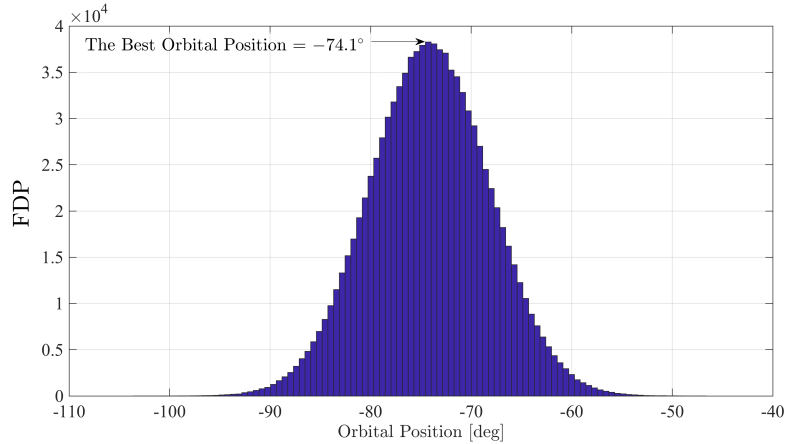
Figure 3.4: Normal distribution of the orbital-position observations.

studied. Initially, symmetric traffic between forward and return links was assumed as $[1 : 1]$ data traffic ratio, meaning 50% (500 Gb/s) of the data throughput in the outbound and 50% (500 Gb/s) in the inbound. However, a more realistic traffic scenario could be 60%:40% which can be expressed as $[3 : 2]$ data traffic ratio. The other three traffic scenarios employed in this thesis are: $[4 : 1]$ (80%:20%), $[7 : 3]$ (70%:30%), and $[9 : 1]$ (90%:10%).

Figure 3.5 shows the results of the number of beams using DVB-S2X and DVB-S2 standards for the feeder uplink. For this purpose, the 1F2P scheme was implemented for both trials, in addition to the satellite links were computed under ideal conditions. Due to the best spectral efficiency, the best results were found by using the DVB-S2X standard, where the number of beams for the feeder uplink is always less than the number of beams using the DVB-S2 standard, for all data traffic scenarios. That is, each feeder uplink beam corresponds to a gateway station (GW) on the ground segment (GS). For this reason, a fewer number of beams are necessary for infrastructure savings on terrestrial segment deployments. Throughout this study, the DVB-S2X standard is used only for assessing and calculating satellite forward links.

Figure 3.6 illustrates the results of the number of carriers in the feeder downlink (return link). Each carrier has a bandwidth of 10 MHz [8], hence, whether the return data traffic is greater, there are more carriers on the feeder downlink. Particularly with 50% of data traffic, i.e. $[1 : 1]$ traffic ratio, there are 11664 carriers. On the other hand, with 10% of data traffic, which is $[9 : 1]$ traffic ratio, there are only 2331 carriers. Therefore, the choice of data-traffic-ratio can be either a positive or a negative factor in order to synchronize all data carriers in the satellite return links towards GWs.

Figure 3.7 depicts the behavior of total capacity vs. data traffic ratio, where the upper limit of capacity is always 1 Tb/s. Nevertheless, there is a slight increase in total capacity due to the greater number of beams, generally, one more beam in the set of feeder uplinks. Table 3.8 shows the increase in the throughput of feeder uplinks whereas the set of feeder downlinks is easier to fit because each carrier has only a
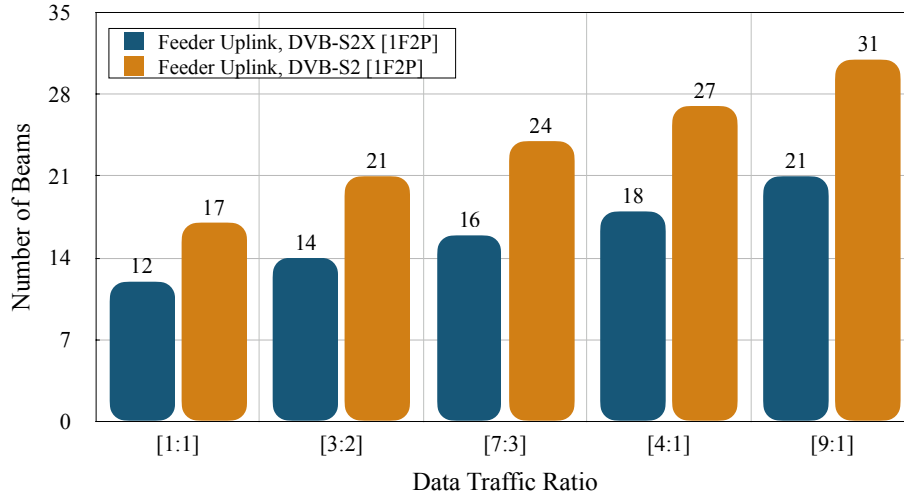
Figure 3.5: Comparison of the obtained number of beams using DVB-S2X and DVB-S2 standards.
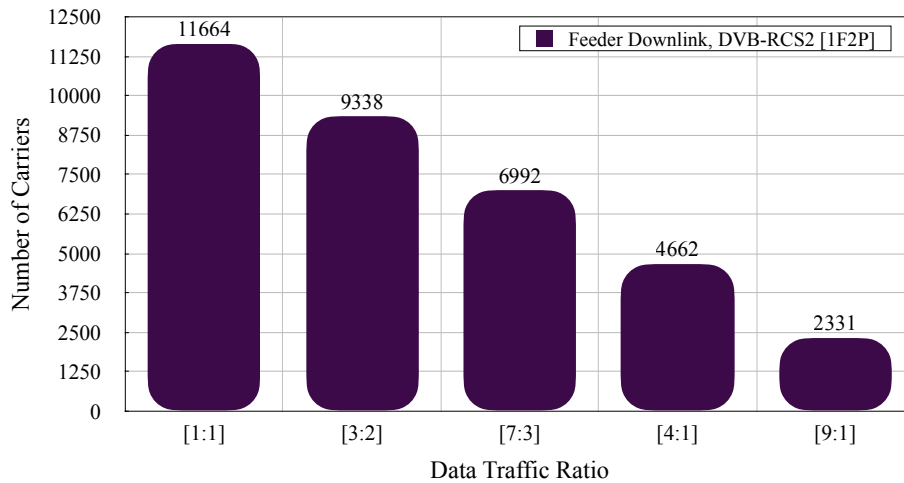
Figure 3.6: The number of carriers in the feeder downlink.

bandwidth of 10 MHz. That is, each feeder-uplink beam has a theoretical capacity of 44.96 Gb/s and each feeder-downlink carrier has a capacity of 42.83 Mb/s.

Figure 3.8 shows the number of beams and carriers in the user link using the 3-color frequency-reuse scheme. Figure 3.8a displays the number of beams using both 3F1P and 3F2P schemes where it is possible to visualize the difference between these two configurations. The number of beams for the 3F1P scheme is approximately twice regarding the 3F2P scheme, for all traffic-ratio cases. However, the theoretical throughput of each user downlink for the 3F2P scheme is twice regarding the 3F1P scheme, that is, 11.24 Gb/s versus 5.62 Gb/s respectively.

On the other hand, Figure 3.8b illustrates the number of carriers for both 3-color frequency-reuse schemes. The number of carriers for the 3F1P scheme is approximately two times greater than the 3F2P scheme, for all traffic-ratio cases.
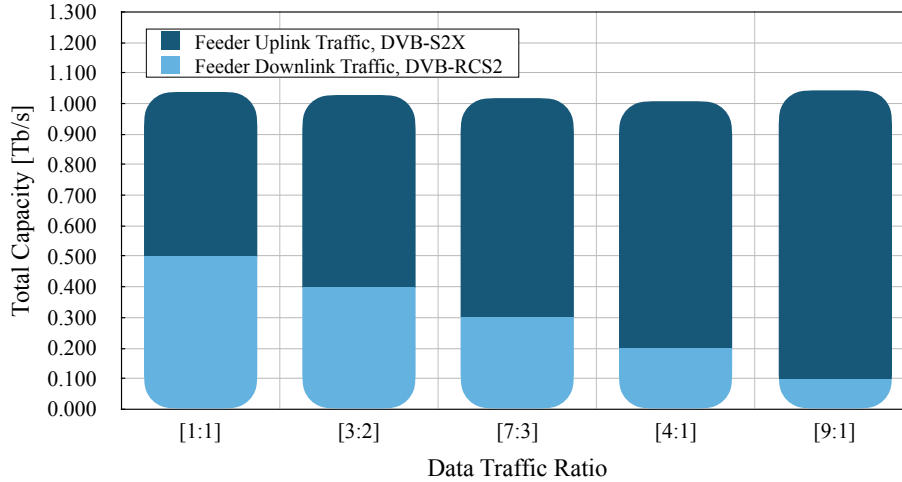
Figure 3.7: Total capacity comparison between different data traffic ratios.

Table 3.8: Throughput Comparisons

Traffic Ratio	Feeder Uplink Throughput [Gb/s]	Feeder Downlink Throughput [Gb/s]	Total Increase
[1 : 1]	539.51	499.62	3.9%
[3 : 2]	629.43	399.98	2.9%
[7 : 3]	719.35	299.50	1.9%
[4 : 1]	809.27	199.69	0.9%
[9 : 1]	944.14	99.85	4.4%

Conversely, the theoretical throughput of each user uplink for the 3F2P scheme is two times greater than the 3F1P scheme, that is, 14.28 Mb/s versus 7.14 Mb/s respectively. It is important to mention that it is tough to manage and to synchronize several user-uplink carriers. For this reason, the sophisticated multiple-frequency time-division multiple access (MF-TDMA) is a great choice in order to manage adequately user traffic, in addition to increasing the number of users on the GS [5].

The analysis for 4-color schemes is similar to 3-color schemes, thus, Figure 3.9 shows the number of beams and carriers using both 4F1P and 4F2P schemes. The common factor between the number of beams for both 4-color schemes was about 2.0 due to the double polarization antenna, reducing the number of beams by a factor of 2.0 but increasing the throughput in the same proportion. Figure 3.9a describes the number of beams in both 4-color schemes where the throughput of the 4F1P scheme is about 4.21 Gb/s and 8.42 Gb/s for the 4F2P scheme in all data traffic cases.

Figure 3.9b illustrates the number of carriers for the user uplink in all data traffic cases, where 4F1P schemes have a number of carriers greater than 4F2P schemes by a factor about 2.0. Finally, the throughput of carrier uplinks for 4F2P schemes is about 10.70 Mb/s whereas the throughput of carrier uplinks for 4F1P schemes is about 5.35 Gb/s.
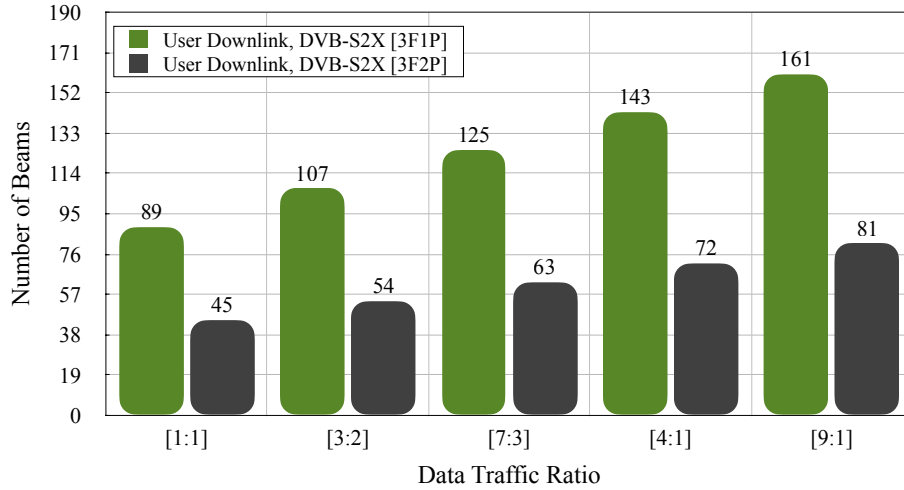
(a) The number of beams in the user downlink for the 3-color schemes.
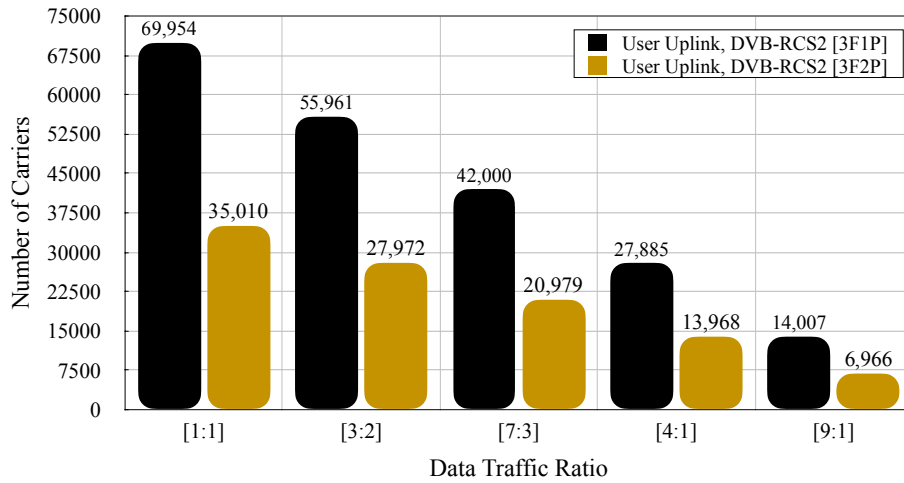
(b) The number of carriers in the user uplink for the 3-color schemes.

Figure 3.8: The number of beams and carriers using both 3F1P and 3F2P schemes.

To sum up, the sizing of the number of beams depends on the coverage area and the data traffic ratio, that is, to find an adequate beamwidth size in order to fit in the desired coverage area. Moreover, it is important to understand the data traffic behavior for each user so that it can choose properly the data traffic scenario. This last parameter is essential to design the throughput in both beams and carriers for the HTS system and to be able to size the right capacity for the end-user. At last but not least, the rain attenuation was not considered in this initial study, however, a complete analysis of rain attenuation and interferences sources are taken into account in the following Chapters.
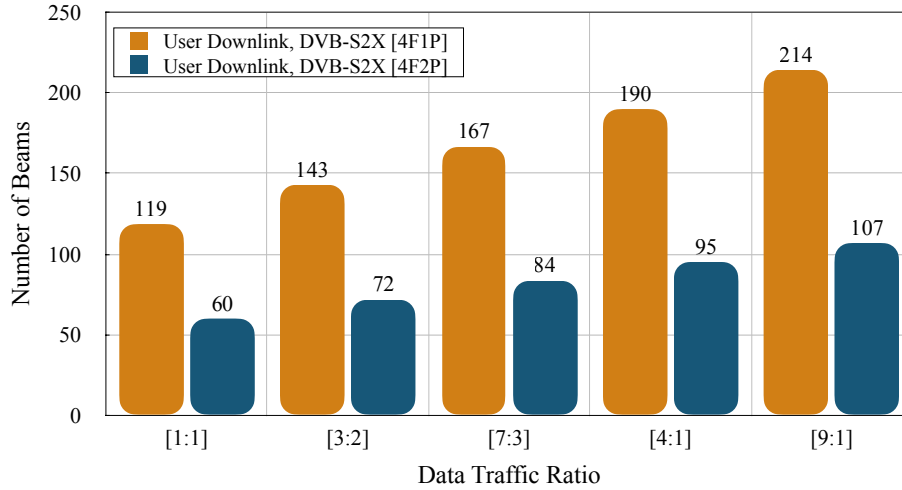
(a) The number of beams in the user downlink for the 4-color schemes.
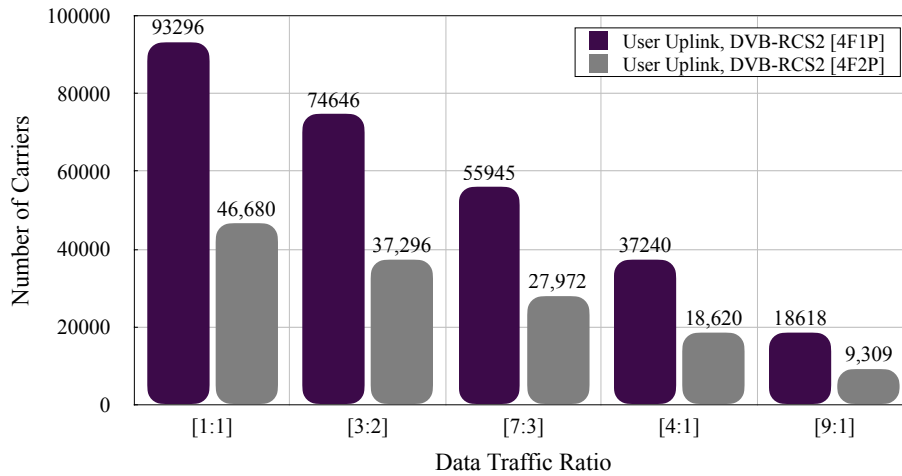
(b) The number of carriers in the user uplink for the 4-color schemes.

Figure 3.9: The number of beams and carriers using both 4F1P and 4F2P schemes.

3.8 Contributions of the Research

This chapter offers an initial study about the quantification of multiple beams and carriers for the HTS systems, therefore, the results have been published in IEEE Latin America Transactions journal and titled:

- Andres Cornejo, Salvador Landeros-Ayala, Ramon Martinez, and Jose M. Matias. Analysis to Quantify and Optimize Spot Beams for a High Throughput Satellite in Ka and Q/V Bands. *IEEE Lat. Am. Trans.*, 17(02):219–227, feb 2019

Chapter 4

Interference Evaluations in Frequency Reuse by Using Offset-Parabolic-Reflector Antennas

4.1 Introduction

This chapter analyzes the features and parameters of an offset-fed parabolic reflector antenna for the HTS system. Indeed, some antenna parameters are important for satellite communication links, so that it is necessary to evaluate the effect of frequency-reuse configurations and spot-beam interferences by designing an offset-parabolic-reflector antenna for this satellite system. That is, the interferences such as cross-polarization (cross-polar) and co-polarization (co-polar) are vital for the system performance and its feasibility. To be precise, the main aim is to adjust and to reduce the interference levels to ensure satellite links for the HTS system, obtaining the maximum advantage for frequency reuse configurations, the number of beams, and the circular polarization. The evaluations of both Multiple Spot Beams and the Carrier-to-Interference employ well-known methods [9,18,59], but with slight modifications to this proposal. Finally, the designed antenna is theoretically and numerically assessed by both implemented methods. Consequently, it is possible to find a satellite reflector antenna suitable for the proposed HTS system.

4.2 Geometric Design of an Offset-Parabolic-Reflector Antenna

Usually, the offset-parabolic-reflector antennas are a great option to reduce sidelobe levels. Motivated by this, moving the feed out of the aperture, some problems with axisymmetrical reflectors can reduce. Hence, diffraction-caused sidelobes, blockage losses, and cross-polarization can reduce or even disappear. For this reason, a proper antenna's design for the proposed HTS system is necessary to accomplish the above-mentioned requirements. Thereby, some parameters were obtained from

geometry and illumination laws by procedures from [19, 60]. In this section, the antenna geometry and its parameters are obtained by the following method.

To begin with, the aperture plane diameter, also known as antenna diameter (D_{ant}), depends on a coefficient obtained from the illumination law, whereby a coefficient with a typical value of 70° introduces some tapering at the edge of the reflector [19]. Consequently, the aperture plane diameter can be expressed by

$$D_{ant} = 70° \frac{\lambda}{\theta_{3dB}}, \tag{4.1}$$

where λ is the wavelength of the frequency band used in a specific satellite link, and the θ_{3dB} is the angle subtended by the half-power points of the main lobe [19]. This last parameter was used to characterize the beamwidth θ_{BW} (see Section 3.6), therefore, it was possible to assume that $\theta_{BW} = \theta_{3dB}$.

Figure 4.1 shows the geometric parameters that are part of the parabolic-reflector-antenna [60, 61]. As the reflector antenna indicates, there is an offset distance that provides a blockage-free region for structures in the focal region [60]. The offset (h) is the distance from the axis of symmetry to the lower reflector edge. Generally, the offset distance is popular in VSAT applications. In this case, this h distance can be obtained from [60] and denoted by

$$h = \frac{D_{ant}}{8}, h > 0 \tag{4.2}$$

The distance from the symmetry axis to the center of the reflector is known as the offset of the reflector center (H) which is described as

$$H = \frac{D_{ant}}{2} + h \tag{4.3}$$

In this procedure, one choice of the antenna design is to keep the ratio of focal length (F) to the antenna diameter (D_{ant}) constant, i.e., the ratio is constant at 1 [62]. Therefore, $F/D_{ant} = 1$. It is worth to mention that the F/D_{ant} choice also impacts on cross-polarization performance [63].

The main contribution to this study was to modify D_{ant} regarding different beamwidths (θ_{3dB}) for both Ka and Q/V bands. Indeed, this is possible as the antenna diameter is a flexible parameter, in addition to exploring different cover areas with multiple spot beams. According to [61], the half of the angle subtended (ψ_s) by the reflector as viewed from the focal point can be expressed as

$$\psi_s = \tan^{-1} \left(\frac{8FD_{ant}}{16F^2 + 4H^2 - D_{ant}^2} \right) \tag{4.4}$$

Meanwhile, the angle which bisects the reflector subtended angle is defined by

$$\psi_B = \tan^{-1} \left(\frac{16FH}{16F^2 + D_{ant}^2 - 4H^2} \right) \tag{4.5}$$

Figure 4.1: The geometry for the offset-parabolic-reflector antenna.

The lower angle (ψ_L) can be described as

$$\psi_L = \psi_B - \psi_s \tag{4.6}$$

Thus, the upper angle (ψ_U) is determined by the sum of the subtended angle and the lower angle, which is expressed by

$$\psi_U = 2\psi_s + \psi_L \tag{4.7}$$

It is important to note that the feed is directed at an angle (ψ_f), i.e., the angle of the feed-antenna-pattern peak relative to reflector axis of symmetry, where the feed is directed toward the point P. The ψ_f is denoted by

$$\psi_f = 2\tan^{-1}\left(\frac{H}{2F}\right) \tag{4.8}$$

Furthermore, the angle ψ_C is similar to the angle ψ_f when the feed aims at the reflector point C, corresponding to the aperture center.

The angle from the lower edge of the dish to feed pointing direction is defined by

$$\psi_P = \psi_f - \psi_L \tag{4.9}$$

For a parabolic reflector, the spherical wave nature of the feed radiation is referred to as spherical spreading loss (SSL), for both upper angle (ψ_U) and lower angle (ψ_L) edges [63], which is given by

$$\text{SSL}(\psi) = -20\log\left[\cos^2\frac{\psi}{2}\right] \tag{4.10}$$

The feed-pointing angle gives a difference in edge illuminations (EI) [60], which is expressed by

$$\Delta \text{EI} = EI_U - EI_L \tag{4.11}$$

The negative of the edge illumination (EI) is the sum of the feed taper (FT) and the spherical-spreading loss (SSL) [60] so that it can be denoted by

$$FT_L + SSL_L = FT_U + SSL_U + \Delta \text{EI} \tag{4.12}$$

Finally, substituting Eq. (4.10) into Eq. (4.12) outputs the following design equation,

$$\Delta \text{FT} = FT_L - FT_U = 40 \log \left\{ \frac{\left[\cos \dfrac{\psi_L}{2} \right]}{\left[\cos \dfrac{\psi_U}{2} \right]} \right\} + \Delta \text{EI} \tag{4.13}$$

Figure 4.1 illustrates the points of FT_U, FT_L, EI_U, and EI_L. For the case of balanced aperture illumination, then $\Delta \text{EI} = 0$. To sum up, each parameter was rigorously evaluated and computed in order to obtain the best performance of the antenna in terms of reduced sidelobes with an acceptable antenna gain according to the focal-length-to- diameter ratio, F/D_{ant} [63]. Therefore, this procedure is able to find a suitable offset-parabolic-reflector antenna for the HTS system.

4.3   Multiple Spot Beams Antenna for HTS Systems

The multiple-aperture-antenna with a single element per beam was chosen to study in this thesis. This antenna is either 3 or 4 apertures, that is, it depends on the frequency-reuse schemes either 3 or 4 colors, respectively. Hereafter, this multiple-aperture-antenna is also known as the multiple beam antenna (MBA) or Type (c) MBA [9]. The MBAs have carried out important researches in this area [9, 13, 59, 62], which have provided some advantages such as:

- The effective spectral bandwidth increases in several folds due to the frequency-reuse channels over numerous spot beams,

- The beam has a smaller size so that the antenna has higher gain, resulting in enhanced effective isotropic radiated power (EIRP) for the downlink and improving the antenna gain-to-noise temperature (G/T) for the uplink,

- The MBAs allows the use of much smaller ground terminals such as GWs and VSATs.

- The satellite reflector could be lower than 5.0 m diameter, which could lead to the best accommodation of multiple reflectors in the spacecraft. Naturally, the antenna diameter depends on its gain and the employed frequency.

(a) 3-cell frequency-reuse

(b) 4-cell frequency-reuse
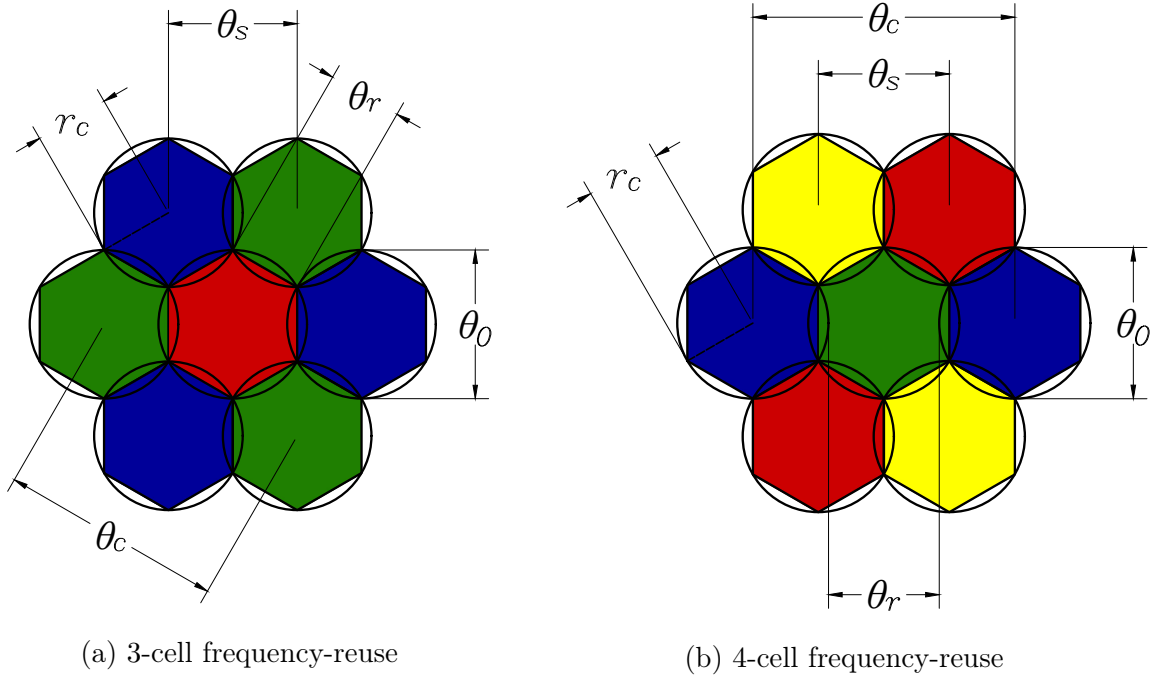
Figure 4.2: The hexagonal-grid layouts of both 3-cell and 4-cell for frequency reuse, illustrating the beam parameters.

4.3.1 Multiple Spot Beams: Design and Analysis

Adjacent beams are generated from different apertures, which are formed in an interleaved multiple-spot-beam coverage on the GS. Therefore, the design of a multiple-spot-beam antenna is depended on the beam size, which is related to the minimum-coverage-area directivity requirement. Figure 4.2 depicts hexagonal grid layouts for both 3-reflector and 4-reflector antennas, where the minimum directivity occurs at the triple beam crossover of the three adjacent beams for MBAs with uniform-size beams.

Furthermore, typical beam overlaps used for MBA designs are approximately 3 dB for two adjacent beams, and 4 dB for three adjacent beams [64]. The optimum overlap level depends on the minimum-coverage directivity, which requires the co-polar isolation among reuse beams and the frequency-reuse scheme (3-color scheme, 4-color scheme, etc.). Consequently, the spacing between adjacent-beam centers (θ_s) determines the number of beams for the desired coverage. Figure 4.2a and Figure 4.2b illustrate the hexagonal-grid layout of the beams for 3-reflector and 4-reflector schemes, respectively. As a result, the θ_s can be expressed by

$$\theta_s = \frac{\sqrt{3}}{2}\theta_0 = \sqrt{3}r_c, \tag{4.14}$$

where θ_0 is the beam diameter at the triple beam crossover and r_c is the coverage radius of the spot beam.

Thus, the minimum number of beams ($N_{b_{min}}$), for the desired coverage area is

given approximately by

$$N_{b_{min}} \approx \frac{A_c}{A_h}, \tag{4.15}$$

where A_c is the coverage area and the A_h represents the area of the hexagonal cell associated with each spot beam. The area of the hexagon can be calculated by $A_h = \frac{3\sqrt{3}}{2}r_c^2$. It is important to note that the actual number of beams (N_b) is usually 20% larger than $N_{b_{min}}$ for an efficient layout of the beams over the coverage area [59]. Moreover, the triple beam crossover levels for outer beams occur at the edge of the beam coverage.

Further, the closest spacing between beam centers reusing the same frequency (θ_c) for 3-reflector (using the 3-color frequency-reuse scheme) and 4-reflector (using the 4-color frequency-reuse scheme) antenna systems can be respectively denoted by

$$\theta_{c,3} = \sqrt{3}\theta_s = 3r_c, \tag{4.16}$$

and,

$$\theta_{c,4} = 2\theta_s = 2\sqrt{3}r_c \tag{4.17}$$

Finally, the closest spacing between the reuse-beam edges (θ_r), determines the achievable carrier-to-interference ratio (CIR), which is expressed by $\theta_r = \theta_c - \theta_0$. Therefore, the θ_r for both 3-reflector and 4-reflector hexagonal-grid layouts can be respectively expressed by

$$\theta_{r,3} = \frac{\theta_s}{2} = r_c, \tag{4.18}$$

and,

$$\theta_{r,4} = \theta_s(\sqrt{3} - 1) = 2(\sqrt{3} - 1)r_c \tag{4.19}$$

4.3.2   Spot Beam Pattern: Model Analysis

The analysis of this model has been very similar to the previous research [18], but it has been more practical and simpler than from the aforecited method. Thus, the simplified analysis has been performed and adapted to this study successfully. As was previously mentioned in Section 4.2, the offset-parabolic-reflector antenna was a good option in order to reduce the sidelobe levels. For this purpose, it was necessary to taper the field distribution over the circular aperture. Thereby, an adequate alternative was to use a parabolic taper on an offset-distance value at the edge. In summary, the antenna performance can be determined analytically for integer taper roll-off values.

For starting, the antenna beam is based on the Gaussian beam pattern obtained from [18], where the antenna pattern function is given by

$$f(\theta_{BW}, n, h) = \frac{h f(\theta_{BW}, n = 0) + \dfrac{1 - h}{n + 1} f(\theta_{BW}, n)}{h + \dfrac{1 - h}{n + 1}} \tag{4.20}$$

so that,

$$f(\theta_{BW}, n) = 2^{n+1}(n+1)!\frac{J_{n+1}(\mathcal{U})}{\mathcal{U}^{n+1}} \tag{4.21}$$

where, for simplicity,

$$\mathcal{U} = \frac{2\pi}{\lambda}D_{ant}\sin\theta_{BW}, \tag{4.22}$$

where h is the offset distance of the parabolic antenna, θ_{BW} is the beamwidth, n is an integer number ranging from 0–2, which represents the field taper roll-off factor. Moreover, J_{n+1} is the Bessel function of the $n+1$ kind, λ is the wavelength of the frequency band used, and D_{ant} the diameter of the antenna aperture.

Applied to this study, the relative gain of the antenna obtained from [18], $G_r(\theta)$, can be found by

$$G_r(\theta_{BW}) = 20\log_{10}(|f(\theta_{BW}), n, h|) \tag{4.23}$$

To sum up, the relative gain of the offset-parabolic-reflector antenna was an important parameter in order to evaluate the CIR of the downlinks for both Q band and Ka-band respectively.

4.4   Carrier-to-Interference: Evaluation Model

In this Section, the methodology to evaluate the carrier-to-interference ratio (CIR) was only determined for both feeder uplinks and downlinks, and solely user downlinks. Thus, it is important to mention that the CIR, also known as ζ, is independent of the propagation impairments, e.g., rain attenuation, as the useful and interfering signal follows the same path from the HTS to the considered ground point [18]. To begin with, a beam grid was defined by several points, where each of these points was scanned in order to compute the ζ. This methodology has been obtained from [18], whose performances and results for the ζ evaluation have been successfully tested.

Some assumptions were proposed regarding the downlink interferences,

- Each beam transmitted identical signals

- At the center of each beam, the forward uplink was the same

- In the spectrum of interest, there was a unique carrier in each beam

- Each GW was located at the beam center, therefore, its signal was emitted from there.

With these considerations, the ζ can be computed by

$$\zeta = \frac{\dfrac{G_r(\omega)}{PL_T}}{\displaystyle\sum_{i=1}^{n}\dfrac{\mathcal{I}_i(\phi)}{PL_i}} \tag{4.24}$$

where $G_r(\omega)$ is the antenna relative gain of the wanted beam at the point of interest by using the Eq. (4.23), ω is the angle that ranges from $\omega = 0$ (beam center) to $\omega = \theta_{BW}/2$ (beam edge), PL_T is the path loss from HTS to the user terminal (UT) at the point T, $\mathcal{I}_i(\phi)$ is a function that describes the nature of the interference, ϕ is the angle between the point T and the center of the i-th beam, and PL_i is the path loss from the HTS to the center of the i-th beam [18, 50].

The evaluation method was divided into 4 cases. Firstly, the method started when the i-th beam evaluated was the same color, (frequency), and the same polarization, then $\mathcal{I}_i$ would become the relative gain of the antenna at the point of interest. Secondly, when the i-th beam was of the same frequency but different polarization, then $\mathcal{I}_i$ would match to the beam relative gain of the cross-polar antenna at the point of interest. For the third case, if the i-th beam was in a different frequency but the same polarization, then $\mathcal{I}_i$ would be similar to the antenna relative gain of the beam at the point of interest but reduced by the Adjacent Carrier Isolation (ACI) factor. Lastly, if the i-th beam was neither in the same frequency-reuse nor the same polarization, then $\mathcal{I}_i$ would become the beam relative gain of the cross-polar antenna at the point of interest but reduced by the Cross-Polar Isolation ($\mathrm{XP_{iso}}$) factor.

Figure 4.3 illustrates the complete interference geometry of the downlink used for the evaluation method. However, for the feeder downlink, the evaluation method only had 2 cases because the feeder link not only did it uses double polarization but it did not use frequency reuse. Hence, when the i-th beam evaluated was the same frequency and the same polarization, then $\mathcal{I}_i$ would be the relative gain of the antenna at the point of interest. Meanwhile, when the i-th beam was the same frequency but different polarization, then $\mathcal{I}_i$ would equal to the beam relative gain of the cross-polar antenna at the point of interest.

The CIR evaluation mechanism used in this thesis was very similar to the method employed in cellular networks. For instance, the ζ of the cellular networks ranges from 13–15 dB [65]. By contrast, for satellite systems in Ka-band, the ζ ranging from 14.5–17.6 dB [66]. Meanwhile, the ζ for the downlink in the Q band must be above 20 dB, keeping an average of 29 dB [18]. This parameter was necessary to define in order to know whether the GW beams had good isolation between each other. For this reason, it was necessary to implement this method to find the minimum CIRs for the proposed HTS system.

4.5 Offset-Parabolic-Reflector Antennas: Numerical Results

4.5.1 Offset-Parabolic-Reflector Antenna: Geometric Parameters

As was analyzed in Section 4.2, the Eqs. (4.1)–(4.9) were used to find each geometric parameter of the offset-parabolic-reflector antenna. For the downlink in Ka-band, the geometric parameters were calculated by 4 different beamwidths in order to explore
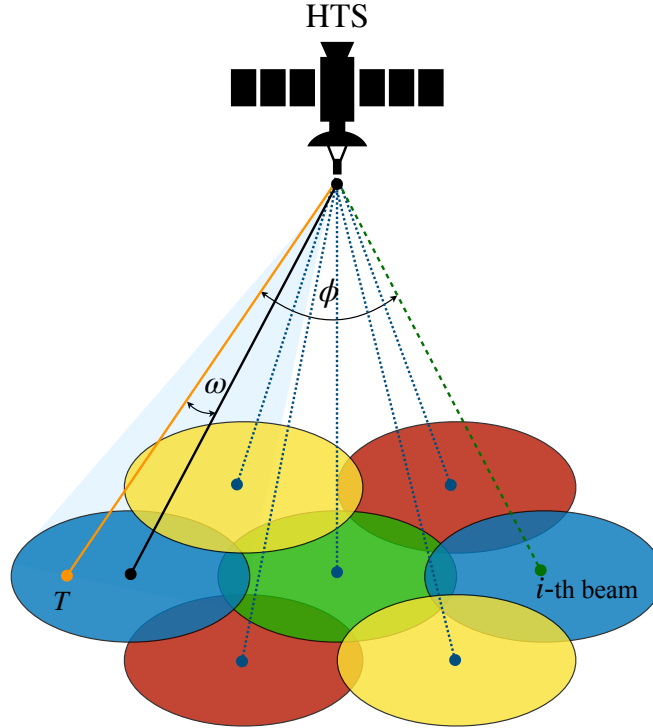
Figure 4.3: The interference geometry of the downlink.

diverse antenna diameters, i.e., $\theta_{BW} = 0.26°$, $\theta_{BW} = 0.32°$, $\theta_{BW} = 0.40°$, and $\theta_{BW} = 0.48°$. Meanwhile, the geometric parameters in the Q band were calculated by only one beamwidth, $\theta_{BW} = 0.20°$. Table 4.1 shows the obtained geometric parameters of the antenna by using the previous equations.

Furthermore, the antenna feed was modeled by a symmetric Gaussian radiation pattern, which was given by a value of 10.0 dB at the edges [60, 63]. Hence, 10.0 dB were defined for both lower (FT_L) and upper (FT_U) edge tapers. Table 4.2 indicates the values of spherical spread losses and edge illuminations obtained by using Eqs. (4.10)–(4.13).

It is important to note that the EI values are not recommended because the difference between EI_U and EI_L must be zero. Thereby, it was necessary to point the antenna feed with an angle ψ_f in order to balance the aperture illumination. Table 4.3 indicates the balanced parameters of the offset-parabolic-reflector antenna when the feed is aiming to the point P with an angle ψ_f. The angle ψ_f was modified by little steps until a high performance of cross-polar isolation(XP_{iso}) was achieved. With these results obtained, offset-parabolic-reflector antennas were simulated by a computer program.

Thus, the computer program TICRA-GRASP was used to simulate the offset-parabolic-reflector antenna [67], which, among other things, was configured to operate in circular polarization, that is, LHCP and RHCP. Figure 4.4 depicts the radiation-pattern diagram of the offset-parabolic-reflector antenna for the feeder downlink, operating in the Q band.

Table 4.1: Geometric Parameters of the Offset-Parabolic-Reflector Antenna

Parameters	Q band	Ka-band				Unit
$Freq_{s-E}$	40.00	20.00	20.00	20.00	20.00	GHz
θ_{BW}	0.20	0.48	0.40	0.32	0.26	deg
D_{ant}	2.63	2.19	2.63	3.28	4.10	m
h	0.33	0.27	0.33	0.41	0.51	m
H	1.64	1.37	1.64	2.05	2.56	m
F/D	1.00	1.00	1.00	1.00	1.00	-
ψ_B	32.93	32.93	32.93	32.93	32.93	deg
ψ_s	25.78	25.78	25.78	25.78	25.78	deg
ψ_L	7.15	7.15	7.15	7.15	7.15	deg
ψ_U	58.72	58.72	58.72	58.72	58.72	deg
ψ_f	34.71	34.71	34.71	34.71	34.71	deg
ψ_P	27.56	27.56	27.56	27.56	27.56	deg

Table 4.2: Spherical Spread Losses and Edges illuminations with a Symmetric Gaussian Radiation Pattern

Parameters	Q band	Ka-band				Unit
$Freq_{s-E}$	40.00	20.00	20.00	20.00	20.00	GHz
θ_{BW}	0.20	0.48	0.40	0.32	0.26	deg
FT_U	10.00	10.00	10.00	10.00	10.00	dB
FT_L	10.00	10.00	10.00	10.00	10.00	dB
ΔFT	0.00	0.00	0.00	0.00	0.00	dB
SSL_U	2.39	2.39	2.39	2.39	2.39	dB
SSL_L	0.03	0.03	0.03	0.03	0.03	dB
EI_U	-12.39	-12.39	-12.39	-12.39	-12.39	dB
EI_L	-10.03	-10.03	-10.03	-10.03	-10.03	dB
ΔEI	-2.35	-2.35	-2.35	-2.35	-2.35	dB

Table 4.3: Spherical Spread Losses and Edges illuminations, $\psi_f = 34.71°$

Parameters	Q band	Ka-band				Unit
$Freq_{s-E}$	40.00	20.00	20.00	20.00	20.00	GHz
θ_{BW}	0.20	0.48	0.40	0.32	0.26	deg
FT_U	10.00	10.00	10.00	10.00	10.00	dB
FT_L	12.35	12.35	12.35	12.35	12.35	dB
ΔFT	2.35	2.35	2.35	2.35	2.35	dB
SSL_U	2.39	2.39	2.39	2.39	2.39	dB
SSL_L	0.03	0.03	0.03	0.03	0.03	dB
EI_U	-12.39	-12.39	-12.39	-12.39	-12.39	dB
EI_L	-12.39	-12.39	-12.39	-12.39	-12.39	dB
ΔEI	0.00	0.00	0.00	0.00	0.00	dB

Demonstrating the pointing of the antenna feed, this parameter is very sensitive so that it influences directly to the cross-polarization.
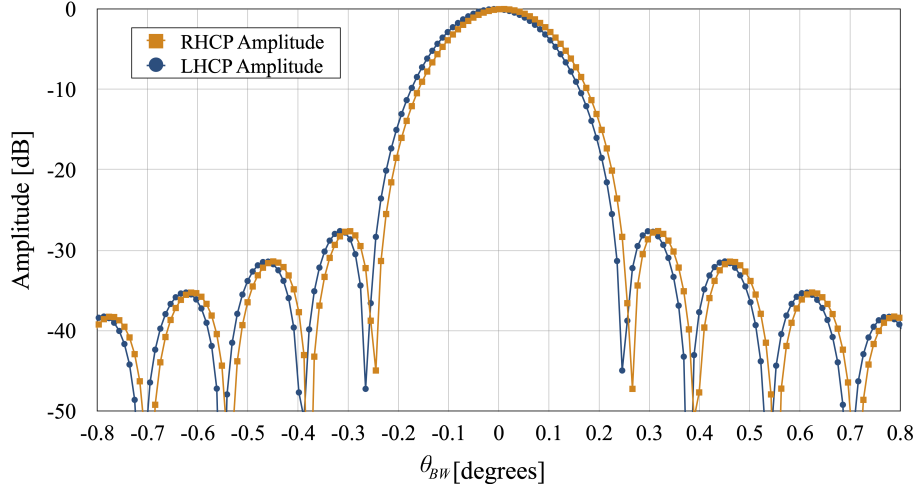
Figure 4.4: Normalized pattern of the offset-parabolic-reflector antenna, 40 GHz.

Table 4.4 shows the XP_{iso} simulation results for both feeder and user downlinks.

Table 4.4: Cross-polar isolation XP_{iso} for both feeder and user downlinks.

Parameters	Q band	Ka-band				Unit
$Freq_{s-E}$	40.00	20.00	20.00	20.00	20.00	GHz
θ_{BW}	0.20	0.48	0.40	0.32	0.26	deg
XP_{iso}	27.78	27.39	27.33	27.25	27.16	dB

The values of XP_{iso} are very similar to each other because the antenna geometry is the same for all cases. Experiments have been carried out to find the most appropriate range of XP_{iso}, which have been ranged from 20–40 dB [1,2,8,17,18,50,61]. Recommending a value of 25 dB, the results are totally convincing and viable for the final design of offset-parabolic-reflector antennas in this study.

4.5.2 Sizing of Spot Beams over the Coverage Area

Initially, it is worth to notice that the Latin American region is the area of interest, where it was possible to find the approximate number of spot beams by using the Eq. (4.15). For this purpose, the Latin American region was divided into three coverage regions: Mexico, Central America & The Caribbean, and South America. Moreover, this evaluation was solely performed by both 3 and 4 frequency-reuse schemes, i.e., for user downlinks in Ka-band, as it is the service area. Table 4.5 displays the approximate number of beams for each coverage area regarding the beamwidths. It is important to note that the number of N_b is approximately 20% larger than the $N_{b_{min}}$ because it is a more realistic scenario for an efficient layout of the spot beams over the coverage area [59]. Therefore, this is an excellent approximation for sizing the spot beams over the coverage area without considering the capacity of the HTS system.

Table 4.5: The Number of Spot Beams ($N_{b_{min}}/N_b$) for the Latin American Regions.

Region	A_c	Beamwidths, θ_{BW}			
		$\theta = 0.48°$	$\theta = 0.40°$	$\theta = 0.32°$	$\theta = 0.26°$
		$r_c \approx 150$ km	$r_c \approx 125$ km	$r_c \approx 100$ km	$r_c \approx 80$ km
		$N_{b_{min}}/N_b$			
Mexico	1.973×10^6 km^2	34/41	49/59	76/92	119/143
Central America & The Caribbean	7.328×10^5 km^2	13/16	19/23	29/35	45/54
South America	1.801×10^7 km^2	309/371	444/533	694/833	1084/1300
Total Beams		356/428	512/615	799/960	1248/1497

4.5.3 CIR Evaluation Results

Primarily one of the advantages of the Q/V band was able to generate narrower beams than other frequency bands. Applying the method of Section 4.4, Table 4.6 shows the CIR results in the Q band for the feeder downlink. Also, it is important to note that this method evaluates and gives the co-channel interference (ζ_{co}) as well as the adjacent-channel interference (ζ_{adj}).

Table 4.6: The CIR Evaluation for Feeder Downlink, 40 GHz.

Parameters				Results	
Denom.	**Values**	**Denom.**	**Values**	**Denom.**	**Values**
$mFnP$	1F2P	D_{ant}	2.63 m	ζ_{co}	36.09 dB
position	92.0° W	EI	-12.39 dB	ζ_{adj}	38.17 dB
$Freq_{s-E}$	40.00 GHz	n	2	$\zeta_{1/\zeta_{co}+1/\zeta_{adj}}$	33.99 dB
θ_{BW}	0.20°	ACI	30.00 dB		
r_c	≈ 65.50 km	XP$_{iso}$	27.78 dB		

The ACI is considered a constant value, which is obtained from [66]. As a result, the $\zeta_{1/\zeta_{co}+1/\zeta_{adj}}$ evaluation gives a value of 33.99 dB, which is higher than the average value of 29.00 dB [18]. Therefore, the offset-parabolic-reflector antenna design is robustness in terms of isolation between other feeder links, assuring an excellent performance for the proposed HTS system.

Figure 4.5 depicts the spot beams of each feeder downlink projected over the Latin America area. Details of geographic locations for the spot beams are in Appendix A.1. This choice was based on the fact that those major cities could access multiple infrastructures of various types, guaranteeing the fast deployment of facilities for gateways stations. Furthermore, it was analyzed the reaching of the HTS system in the entire Latin American region, theoretically.

Meanwhile, Table 4.7 indicates the CIR results for the 3-color scheme, evaluating both simple and double polarization. In this evaluation, the frequency band was of 20.00 GHz in the Ka-band, the HTS orbital position was 92.0° W, as was discussed in subsection 2.2.1, and the taper roll-off, n, was of zero for all cases. The co-polar evaluation was simplified by considering the closest six interferences [9,59,62].

Figure 4.5: Spot beams of feeder downlinks over the Latin America region.

Furthermore, the crossover (triple-point) level was calculated by using the method from [64].

To sum up, the CIR results are very promising where each evaluation is higher than the range between 14.5–17.6 dB. Therefore, this scheme can be used as the main layout in order to cover the ground segment in Ka-band. Figure 4.6 illustrates the 3-color frequency-reuse schemes over the Mexico area. For the 4-color frequency-reuse scheme, the evaluation method was the same as the 3-color scheme, for this reason, the parameters were exactly the same. Table 4.8 shows the CIR results for the 4-color scheme, assessing both simple and double polarization.

The 4-color frequency-reuse scheme is more aggressive than the 3-color scheme, therefore, the CIR results for the 4-color scheme are lower than CIR results for 3-color schemes. Although the CIR values are a few dBs lower than CIR values for 3-color schemes, it does not mean bad results. In fact, the CIR results for 4-color schemes are within the range value between 14.5–17.5 dB, where the scheme 4F1P overcomes slightly that range. Figure 4.7 illustrates the 4-color frequency-reuse scheme over the Mexico area.

In conclusion, the antenna results are very encouraging, giving an excellent outlook on the design of the offset-parabolic-reflector antennas for HTS systems. The double polarization increases the capacity of the link without degrading the signal at the reception antenna. It is also important to mention that the larger beam spacing enables a proportionate increase in the feed horn size, which improves the antenna gain by reducing spillover loss, i.e., the reflector illuminates optimally increasing the

Table 4.7: The CIR Evaluation for the 3-color Frequency-reuse Scheme.

Denom.	Values			
θ_{BW}	0.48°	0.40°	0.32°	0.26°
r_c	≈ 150 km	≈ 125 km	≈ 100 km	≈ 80 km
D_{ant}	2.19 m	2.63 m	3.28 m	4.10 m
EI	−12.39 dB	−12.39 dB	−12.39 dB	−12.39 dB
ACI	30.00 dB	30.00 dB	30.00 dB	30.00 dB
$\mathbf{XP_{iso}}$	27.39 dB	27.33 dB	27.25 dB	27.16 dB
Results				
Denom.	**3F1P Scheme**			
ζ_{co}	21.36 dB	21.29 dB	21.20 dB	21.03 dB
ζ_{adj}	25.49 dB	25.45 dB	25.40 dB	25.34 dB
$\zeta_{1/\zeta_{co}+1/\zeta_{adj}}$	19.94 dB	19.88 dB	19.80 dB	19.66 dB
Denom.	**3F2P Scheme**			
ζ_{co}	21.36 dB	21.29 dB	21.20 dB	21.03 dB
ζ_{adj}	24.32 dB	24.19 dB	24.07 dB	23.99 dB
$\zeta_{1/\zeta_{co}+1/\zeta_{adj}}$	19.58 dB	19.49 dB	19.39 dB	19.25 dB
Crossover level	−2.88 dB	−2.97 dB	−3.05 dB	−3.10 dB

beam End-of-Coverage (EoC) gain and reducing sidelobe levels.

Furthermore, these results demonstrate that both 3-color and 4-color frequency reuse schemes accomplish the interference requirements in order to generate spot beams from offset-parabolic-reflector antennas, standing out the 3-color frequency-reuse schemes so that it is possible to recommend these layouts for the HTS systems.

Finally, the Latin America region requires a lot of spot beams in order to cover the entire area. For this purpose, an HTS fleet is necessary to supply the demand for spot beams in the region.

4.5.4 Link Margin

According to [8], the aim of link margin evaluation is to determine the positive margin of operation between the feeder uplink and the user downlink by using the combined CNIR, i.e., this analysis is only for the forward link in clear-sky conditions. The average value of the CNR for feeder uplinks in the V band was about 32.36 dB, whereas the average value of the CNR for user downlinks in the Ka-band was about 24.61 dB, as was discussed in Chapter 3. Furthermore, the intermodulation interference (ζ_{im}) is a constant value of 25.00 dB [8]. Table 4.9 shows the CNIR for both cases by using the interferences values obtained from simulations. For user downlinks, it was used the 3F1P scheme with a beamwidth (θ_{BW}) of 0.32°.

As a result, the combined CNIR for the forward link was 17.43 dB for the maximum co-channel CIR (ζ_{co}) for both feeder uplink and user downlink, which meant a margin of 3.93 dB over the required value of 13.50 dB [8]. Figure 4.8 depicts the link margin as a function of co-channel CIR that ranges from 12.00 to 25.00 dB.

(a) $\theta_{BW} = 0.26°$

(b) $\theta_{BW} = 0.32°$

(c) $\theta_{BW} = 0.40°$

(d) $\theta_{BW} = 0.48°$
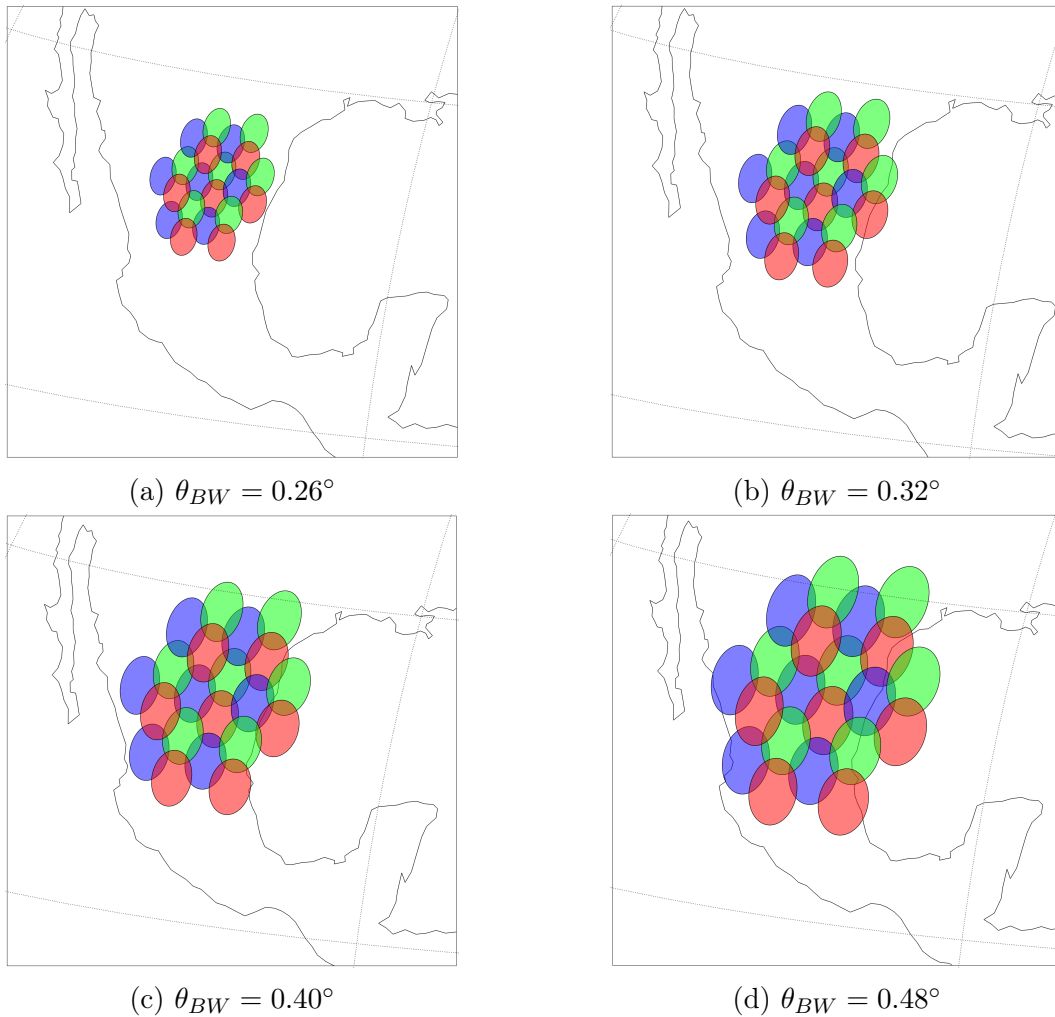
Figure 4.6: The 3-color frequency-reuse schemes over the Mexico region with 4 different beamwidths.

It is important to note that around 17.60 dB of co-channel CIR is required to obtain a positive margin. The co-channel CIR for the user downlink is much lower than the feeder uplink CIR, for this reason, it is a significant challenge and limiting factor so that it is necessary to further studies to improve the CIR antenna. In conclusion, these evaluations of offset-parabolic-antennas give excellent results but it is imperative to carry out real trials in order to obtain a more propitious scenario. All calculations in this thesis were performed on an Intel Core i5 2×2.70 GHz machine with 8 GB RAM.

4.6 Contributions of the Research

The results of this Chapter were published for The International Journal Of Engineering and Science and Congreso Internacional de Computacion y Telecomunicaciones, COMTEL, as follows. However, It is important to mention that

Table 4.8: The CIR Evaluation for the 4-color Frequency-reuse Scheme.

Denom.	Values			
θ_{BW}	0.48°	0.40°	0.32°	0.26°
r_c	$\approx$ 150 km	$\approx$ 125 km	$\approx$ 100 km	$\approx$ 80 km
D_{ant}	2.19 m	2.63 m	3.28 m	4.10 m
EI	-12.39 dB	-12.39 dB	-12.39 dB	-12.39 dB
ACI	30.00 dB	30.00 dB	30.00 dB	30.00 dB
XP$_{iso}$	27.39 dB	27.33 dB	27.25 dB	27.16 dB
Results				
Denom.	4F1P Scheme			
ζ_{co}	18.95 dB	18.95 dB	18.95 dB	18.94 dB
ζ_{adj}	25.49 dB	25.45 dB	25.40 dB	25.34 dB
$\zeta_{1/\zeta_{co}+1/\zeta_{adj}}$	18.07 dB	18.07 dB	18.06 dB	18.04 dB
Denom.	4F2P Scheme			
ζ_{co}	18.95 dB	18.95 dB	18.95 dB	18.94 dB
ζ_{adj}	23.14 dB	23.09 dB	23.03 dB	22.96 dB
$\zeta_{1/\zeta_{co}+1/\zeta_{adj}}$	17.54 dB	17.53 dB	17.51 dB	17.49 dB
Crossover level	-3.84 dB	-3.96 dB	-4.07 dB	-4.13 dB

Table 4.9: The CNIR Values for the Forward Link.

Feeder Uplink		User Downlink	
Parameters	**Values**	**Parameters**	**Values**
CNR	32.36 dB	CNR	24.61 dB
ζ_{co}	36.09 dB	ζ_{co}	21.20 dB
ζ_{adj}	38.17 dB	ζ_{adj}	25.40 dB
		ζ_{im}	25.00 dB
CNIR$_{up}$	30.09 dB	CNIR$_{dn}$	17.67 dB

the conference proceedings were published in "*Revista de Tecnología e Información*" by Universidad Inca Garcilaso de la Vega, Lima-Peru.

- Andres Cornejo, Salvador Landeros-Ayala, Ramon Martinez-Rodriguez, and Jose M Matias. Interference Evaluations in Frequency Reuse by Using Offset-Parabolic-Reflector Antennas for a UHTS System. *Int. J. Eng. Sci.*, 7(8):34–45, 2018.

- Andres Cornejo, Salvador Landeros-Ayala, Ramon Martínez Rodríguez-Osorio, and Jose M Matias. A method for designing an offset-parabolic-reflector antenna for a ultra-high throuhput satellite. *In Rev. Tecnol. e Inf.*, volume 16, pages 84–87, Lima, Peru, 2018. Universidad Inca Garcilaso de la Vega.

(a) $\theta_{BW} = 0.26°$

(b) $\theta_{BW} = 0.32°$

(c) $\theta_{BW} = 0.40°$

(d) $\theta_{BW} = 0.48°$
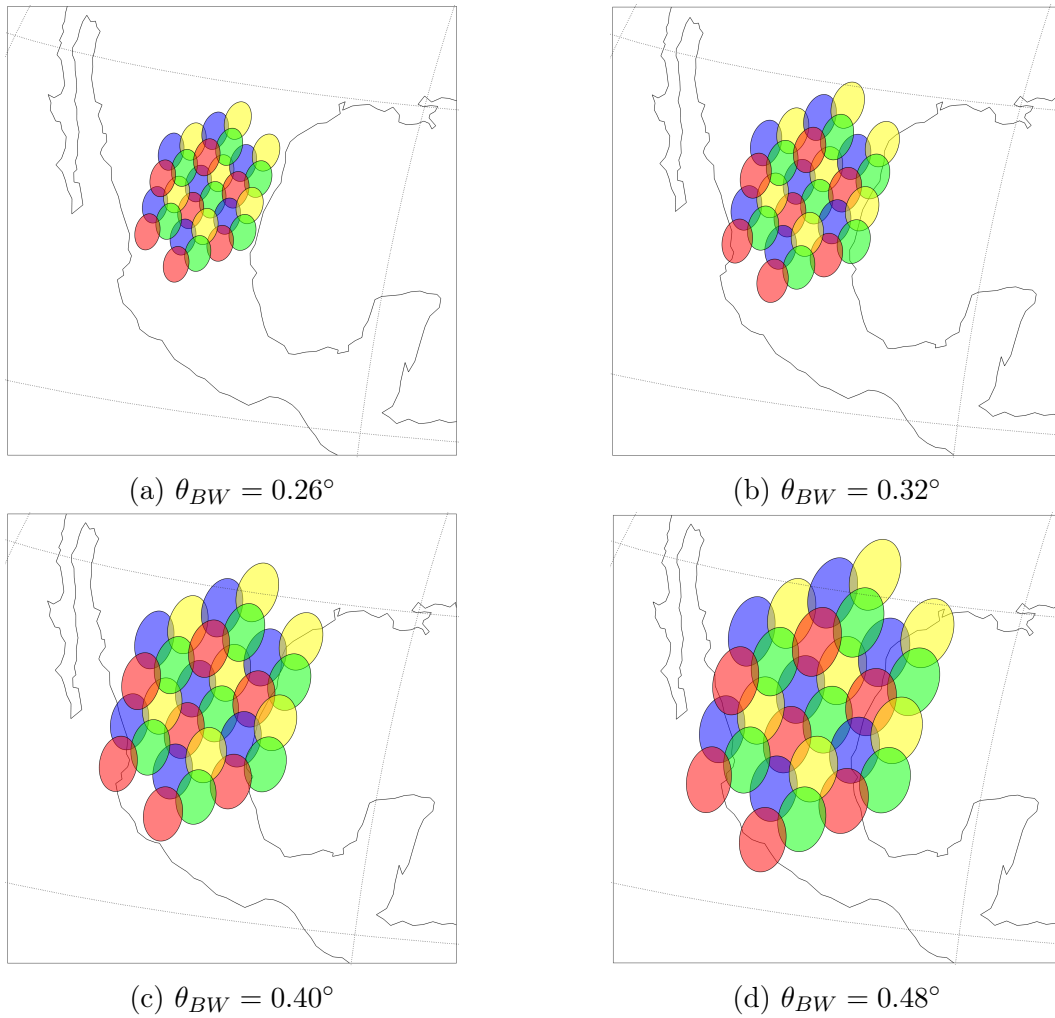
Figure 4.7: The 4-color frequency-reuse schemes over the Mexico region with 4 different beamwidths.
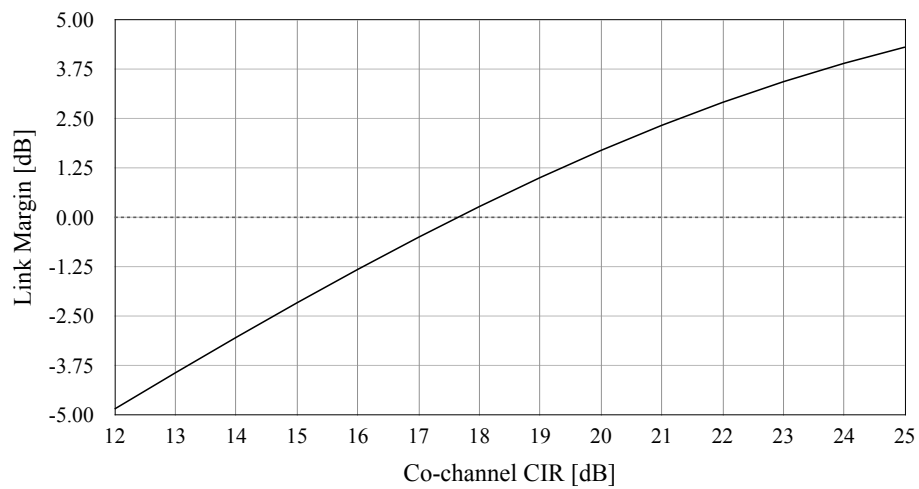
Figure 4.8: Forward link margin vs. co-channel CIR.

Chapter 5

Method of Rain Attenuation Prediction Based On Long-Short Term Memory Network

5.1   Introduction

Satellite communication links operate at different frequency bands such as L band, C band, and higher. Despite the higher frequency bands have more available spectrum, the satellite links are more susceptible to weather impairments, especially the rain attenuation. For this reason, a lot of research has been carried out in order to find accurate models of rain attenuation, whose methods have been developed by stochastic processes [37,68,69]. The Maseng-Bakken model is currently employed for the International Telecommunication Union (ITU) and its Recommendation ITU-R P.1853 [38]. Other researchers have been performed experimental models, such as the Prévision d'Ensemble ARPEGE (PEARP) system by Météo-France [15] and fade mitigation experiments for the ALPHASAT Satellite [70]. However, the main problem is the lack of historical rain database for each location and very few experimental models so that the stochastic models are the only theoretical methods in order to determine the main implications of the rain attenuation over satellite links.

Nowadays, Machine Learning techniques are employed by several real-world applications as well as theoretical problems, especially in clustering, classification, and regression problems. To be specific, Machine learning is the study of computer algorithms that improve automatically through experience. It is related to a subfield of computer sciences and is considered a subset of artificial intelligence. In this context, a novel method is proposed in this thesis by a machine learning method, to be precise, a deep learning technique. Thereby, the Long-short Term Memory (LSTM) network is a deep learning technique and predicts, accurately, events of rain-attenuation without relying on either mathematical or stochastic models.

The main objective is to train and validate the proposed models based on LSTM networks by using artificial rain attenuation time-series at the input. That is, the model learns from experience where the deep learning algorithms employ advanced

computational methods in order to learn directly from input data without appealing to predetermined models or equations. Moreover, the rain-attenuation outcomes are useful to determine the status-in-advance of the satellite link and to anticipate a sudden link outage due to heavy rain. Indeed, it is important to obtain reliable results with the aim of guaranteeing the availability of satellite links and improving mechanisms such as the satellite link switching [71–73], site diversity on the ground segment [14, 22, 26], and uplink power control (ULPC) on satellite links [74–76], especially in extremely high-frequency bands (EHF).

Finally, a comparison with other methods/models is employed to determine the best model in terms of performance, generalization, and accuracy.

5.2 Implementation of the Proposed Deep Learning Method Based on LSTM Network

5.2.1 Deep Learning Network: Model Architecture

LSTM is based on a recurrent architecture network, which is designed to overcome error back-flow problems. An LSTM layer is able to support sequence data and time series in a network. Despite the input sequence data can be either noisy or incompressible, the LSTM network can learn to join time intervals in excess of 1000 steps without losing short-time-capabilities [77]. This is possible by an efficient gradient-based algorithm. In this thesis, there is a need to predict the values of future time steps of the input time-series. Therefore, the input time-series are trained by the proposed LSTM network with sequence-to-sequence mode, where the output data are sequences with values shifted by a one time step. In other words, the LSTM network learns to predict the value of the next time step, $t + 1$, for each time step, t, of the input time-series sequence.

A. The Architecture of a Single LSTM Cell

Consider a dataset $\boldsymbol{x} = (\mathbf{x}^{(1)}, \mathbf{x}^{(2)}, \ldots, \mathbf{x}^{(m)})$, where each element is a vector (sequence) $\mathbf{x}^{(m)} \in \mathbb{R}^K$, and m is the number of examples of each dataset. For simplicity and readability, this general approach only considers $m = 1$ examples in dataset $\boldsymbol{x}$. Figure 5.1 depicts the architecture of a single LSTM cell, providing two recurrent features (LSTM cell outputs). The outputs are also known as the hidden (h_t) and cell (c_t) states.

For this purpose, let $\mathbb{U} = [0, 1]$ indicate the unit interval, whereas let $\pm\mathbb{U} = [-1, 1]$. Denoted by $\mathcal{L}$, the LSTM cell is a mathematical function that enables three inputs and generates two outputs. The LSTM cell function can be expressed as

$$(h_t, c_t) = \mathcal{L}(h_{t-1}, c_{t-1}, \mathbf{x}_t), \tag{5.1}$$

where $h_t, h_{t-1}, c_t, c_{t-1} \in \pm\mathbb{U}$ and the input vector $\mathbf{x}_t \in \mathbb{R}^K$ [77, 78]. In order to compute the first output and updated cell state, the initial state of the cell and the
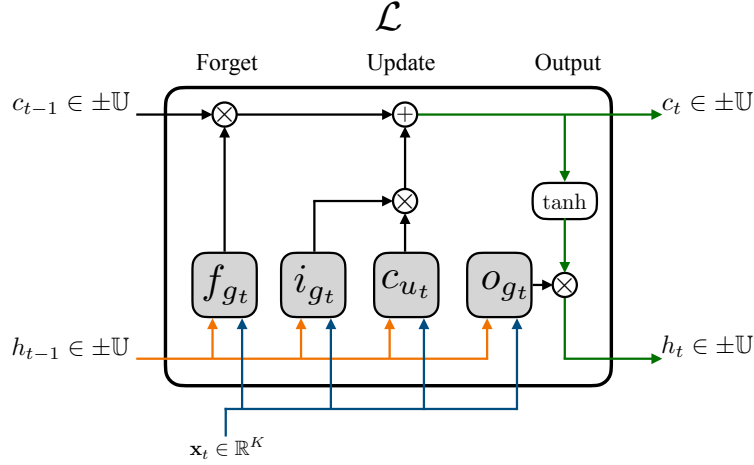
Figure 5.1: A single LSTM cell diagram [78].

first time step of the sequence are used by the LSTM cell. That is, the current state of the cell, at time step t, is employed by the LSTM cell $(h_{t-1}, c_{t-1},)$, whereas the next time step of the sequence is used to compute the output state h_t, in addition to updating the cell state c_t. Therefore, the hidden and cell states are part of the state of the cell.

At time step t, h_t and c_t states are left at the output so that the same cell can be fed back by these states at time step $t+1$. It is important to mention that an element of the input sequence $\mathbf{x} \in \mathbb{R}^K$ is also fed into the cell any time step t [78]. Meanwhile, the learned information from previous time steps is contained in the cell state. In summary, the cell appends information to or deletes information from the cell state at each time step, in other words, the cell is able to control these updates employing gates.

For this purpose, the flow of data plays an important role in the LSTM cell, where the hidden state, $h_{t-1} \in \pm\mathbb{U}$, and the input vector, $\mathbf{x}_t \in \mathbb{R}^K$, feed three gates (functions), as can be seen in Figure 5.1. At the time t, the three gates (forget, input, and output functions) are respectively given by

$$f_{g_t}(\mathbf{x}_t, h_{t-1}) = \sigma_g(\mathbf{w}_{\mathbf{x}f}^\mathsf{T}\mathbf{x}_t + w_{h_f}h_{t-1} + b_f) \in \mathbb{U}, \tag{5.2}$$

$$i_{g_t}(\mathbf{x}_t, h_{t-1}) = \sigma_g(\mathbf{w}_{\mathbf{x}i}^\mathsf{T}\mathbf{x}_t + w_{h_i}h_{t-1} + b_i) \in \mathbb{U}, \tag{5.3}$$

$$o_{g_t}(\mathbf{x}_t, h_{t-1}) = \sigma_g(\mathbf{w}_{\mathbf{x}o}^\mathsf{T}\mathbf{x}_t + w_{h_o}h_{t-1} + b_o) \in \mathbb{U}, \tag{5.4}$$

where σ_g is the gate activation function, $\mathbf{w}_{\mathbf{x}f}, \mathbf{w}_{\mathbf{x}i}, \mathbf{w}_{\mathbf{x}o} \in \mathbb{R}^K$ are the weight vectors, and $w_{h_f}, w_{h_i}, w_{h_o}, b_f, b_i, b_o \in \mathbb{R}$ are the recurrent weights and biases, respectively. During the training process of the cell, the weights are capable of learning. By default, σ_g is based on the sigmoid function to compute the gate activation function. For this reason, the gates of a single LSTM cell produce scalar values. Figure 5.1 stands out how the gates forget, update, and output the cell and hidden states. These three

gates can be interpreted as switches, that is, if their outputs are near 1, then they are on. Otherwise, when the outputs are close to 0, then they are off.

Furthermore, the cell update function is built from a single neuron, which, at time step t, is expressed as

$$c_{u_t}(\mathbf{x}_t, h_{t-1}) = \tanh(\mathbf{w_x}^\mathsf{T}\mathbf{x}_t + w_h h_{t-1} + b) \in \pm\mathbb{U}, \qquad (5.5)$$

where tanh is the state activation function, $\mathbf{w}_x \in \mathbb{R}^K$ is the weight vector, and $w_h, b \in \mathbb{R}$ are the recurrent weights and bias, respectively. Also, these weight parameters are learned in the training process. The state activation function is based on the hyperbolic tangent function, which is also set by default. Specifically, the tanh and sigmoid activation functions are discussed in Section 5.2.2.

Finally, the forget gate, f_g, controls the level of the cell state reset (forget), whereas the input gate, i_g, controls the level of the cell state update, c_u, that adds it to the cell state. Moreover, the output gate, o_g, controls the modified cell state to become the next hidden state [77, 78]. As a result, the new cell and hidden states, at time step t, can be expressed as

$$c_t = f_{g_t} \cdot c_{t-1} + i_{g_t} \cdot c_{u_t} \in \pm\mathbb{U}, \qquad (5.6)$$

$$h_t = o_{g_t} \cdot \tanh(c_t) \in \pm\mathbb{U}, \qquad (5.7)$$

where both values are scalars. For readability, it is important to note that all of these functions and parameters are encapsulated in the function $\mathcal{L}$, as can be seen in Eq. (5.1).

B. The Architecture of a Layer of LSTM Cells

Figure 5.2 illustrates a layer composed of several LSTM cells U, also known as the number of hidden units, and features C. For this purpose, the LSTM layer, denoted by $\mathcal{L}_\mathcal{U}$, is the concatenation of LSTM cells, $\mathcal{L}_1, \mathcal{L}_2, \ldots, \mathcal{L}_U$, creating an LSTM Block. At time step t, both hidden, $\mathbf{h}_t$, and cell, $\mathbf{c}_t$, states indicate the LSTM Block output. Each cell has a different set of weight parameters, thus, the mathematical expression of the LSTM layer is given by

$$(h_{1_t}, c_{1_t}) = \mathcal{L}_1(h_{1_{(t-1)}}, c_{1_{(t-1)}}, \mathbf{x}_t),$$
$$(h_{2_t}, c_{2_t}) = \mathcal{L}_2(h_{2_{(t-1)}}, c_{2_{(t-1)}}, \mathbf{x}_t),$$
$$\vdots$$
$$(h_{U_t}, c_{U_t}) = \mathcal{L}_U(h_{U_{(t-1)}}, c_{U_{(t-1)}}, \mathbf{x}_t),$$

therefore, the expression can be also rewritten as

$$(\mathbf{h}_t, \mathbf{c}_t) = \mathcal{L}_U(\mathbf{h}_{t-1}, \mathbf{c}_{t-1}, \mathbf{x}_t), \qquad (5.8)$$
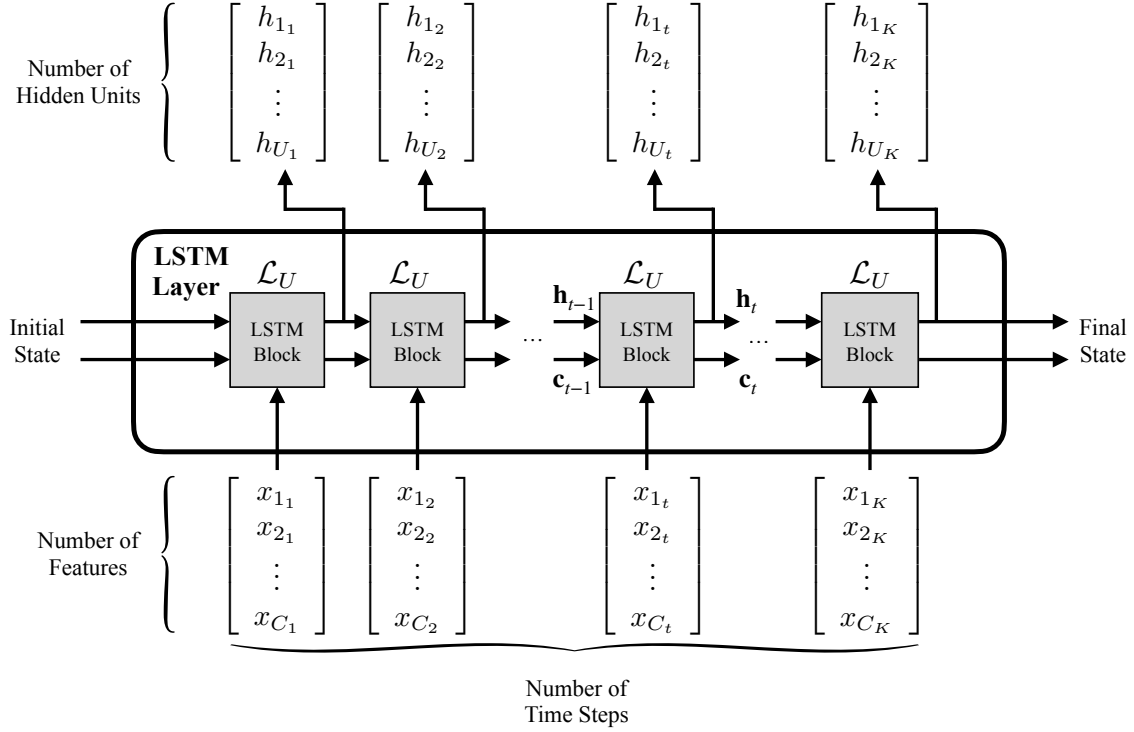
Figure 5.2: The architecture of an LSTM layer [77].

where $\mathbf{h}_t, \mathbf{h}_{t-1}, \mathbf{c}_t, \mathbf{c}_{t-1} \in \pm\mathbb{U}^U$, and $\mathbf{x}_t \in \mathbb{R}^K$. As a result, the cell and hidden states, at time step t, can be respectively given by

$$\mathbf{c}_t = f_{g_t} \odot \mathbf{c}_{t-1} + i_{g_t} \odot \mathbf{c}_{u_t} \in \pm\mathbb{U}^U, \tag{5.9}$$

$$\mathbf{h}_t = o_{g_t} \odot \tanh(\mathbf{c}_t) \in \pm\mathbb{U}^U, \tag{5.10}$$

where $\odot$ is the Hadamard product, that is the element-wise multiplication of vectors. Moreover, the dot products become matrix-vector products. Here, the individual weight vectors and biases from each LSTM cells can be stored in matrices. Therefore, the three gates and the cell update function contain weight matrices, $\mathbf{W}_{\mathbf{x}f}, \mathbf{W}_{\mathbf{x}i}, \mathbf{W}_{\mathbf{x}o}, \mathbf{W}_{\mathbf{x}} \in \mathbb{R}^{U \times K}$, respectively. Meanwhile, the stacked hidden state is a U-dimensional vector, therefore, the gates contain recurrent weight matrices, $\mathbf{W}_{\mathbf{h}f}, \mathbf{W}_{\mathbf{h}i}, \mathbf{W}_{\mathbf{h}o}, \mathbf{W}_{\mathbf{h}} \in \mathbb{R}^{U \times U}$, and bias vectors $\mathbf{b}_f, \mathbf{b}_i, \mathbf{b}_o, \mathbf{b} \in \mathbb{R}^U$ [78].

As a shorthand, all parameters of the LSTM network are usually concatenated and expressed as a whole by parameter $\boldsymbol{\Theta}_{\mathcal{L}}$ [79]. For notational convenience, the parameter $\boldsymbol{\Theta}_{\mathcal{L}}$ can be written as

$$\boldsymbol{\Theta}_{\mathcal{L}} \equiv \left\{ \begin{array}{ccc} \mathbf{W}_{\mathbf{x}f}, & \mathbf{W}_{\mathbf{h}f}, & \mathbf{b}_f \\ \mathbf{W}_{\mathbf{x}i}, & \mathbf{W}_{\mathbf{h}i}, & \mathbf{b}_i \\ \mathbf{W}_{\mathbf{x}o}, & \mathbf{W}_{\mathbf{h}o}, & \mathbf{b}_o \\ \mathbf{W}_{\mathbf{x}}, & \mathbf{W}_{\mathbf{h}}, & \mathbf{b} \end{array} \right\} \tag{5.11}$$

C. The Architecture of an LSTM Multi-Layer Network

In this case, multiple layers could improve the output accuracy, increasing the LSTM network complexity. At time step t, the function $\mathcal{L}_U$ has two outputs $\mathbf{h}_t, \mathbf{c}_t \in \mathbb{U}^U$, thereby, the next LSTM layer can be sequentially fed by the hidden state from the previous LSTM layer. Figure 5.3 depicts how the states pass through an LSTM multi-layer network.
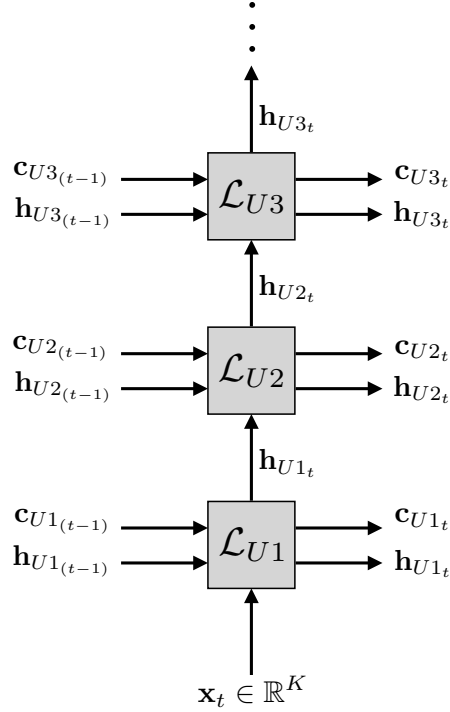
Figure 5.3: The architecture of an LSTM multi-layer [80].

For simplicity, an LSTM multi-layer network can be encapsulated by a function $\mathcal{S}$, where

$$\vdots$$
$$(\mathbf{h}_{U3_t}, \mathbf{c}_{U3_t}) = \mathcal{L}_{U3}(\mathbf{h}_{U3_{(t-1)}}, \mathbf{c}_{U3_{(t-1)}}, \mathbf{h}_{U2_t}),$$
$$(\mathbf{h}_{U2_t}, \mathbf{c}_{U2_t}) = \mathcal{L}_{U2}(\mathbf{h}_{U2_{(t-1)}}, \mathbf{c}_{U2_{(t-1)}}, \mathbf{h}_{U1_t}),$$
$$(\mathbf{h}_{U1_t}, \mathbf{c}_{U1_t}) = \mathcal{L}_{U1}(\mathbf{h}_{U1_{(t-1)}}, \mathbf{c}_{U1_{(t-1)}}, \mathbf{x}_t),$$

can be given by

$$(\mathbf{H}_t, \mathbf{C}_t) = \mathcal{S}(\mathbf{H}_{t-1}, \mathbf{C}_{t-1}, \mathbf{x}_t). \tag{5.12}$$

It is important to mention that each layer can have a different number of LSTM units $U1, U2, U3 \ldots$, so that the dimensions of the hidden and cell states can be uneven for each LSTM layer. At time step t, the variables $\mathbf{H}_t$ and $\mathbf{C}_t$ represent the collection of all hidden and cell states, respectively [78]. As can be seen, the LSTM multi-layer network is a larger model, containing a lot of stacked LSTM cells. For this

reason, the single and multiple layer LSTM networks can be employed in time-series forecasting [77, 78, 80], which is the aim of this thesis.

D. The Architecture of the Proposed Deep Learning Network

Figure 5.4 describes in detail the proposed LSTM layer where each input dataset obtained from ITU-R P.1853 [38], $\boldsymbol{A}'_i = (\mathbf{A}'^{(1)}_{t,i}, \mathbf{A}'^{(2)}_{t,i}, \ldots, \mathbf{A}'^{(m)}_{t,i})$ for $i = 1, 2, \ldots, N$, and $t = 1, 2, \ldots, K$, is made up of m examples, $\mathbf{A}'^{(m)}_{t,i} \in \mathbb{R}^K$, where K is the number of samples in each time-series, and N is the number of GW-sites on the ground segment. Here, each rain-attenuation time-series must be normalized to improve the convergence of the gradient descendent, for this reason, the input dataset of rain attenuation is denoted by $\boldsymbol{A}'_i$. Indeed, the normalization method is discussed in more detail in Section 5.2.2. In this thesis, each time series is a univariate sequence, that is, it is a single series of observations. Furthermore, each time series has a single feature, $C = 1$, and each dataset has 40 examples, i.e., $m = \{1, 2, \ldots, 40\}$. Therefore, it is a many-to-one sequence problem with a single feature. Motivated by this, an LSTM network model is built in order to learn from the time series of past observations to predict the next value in the sequence.
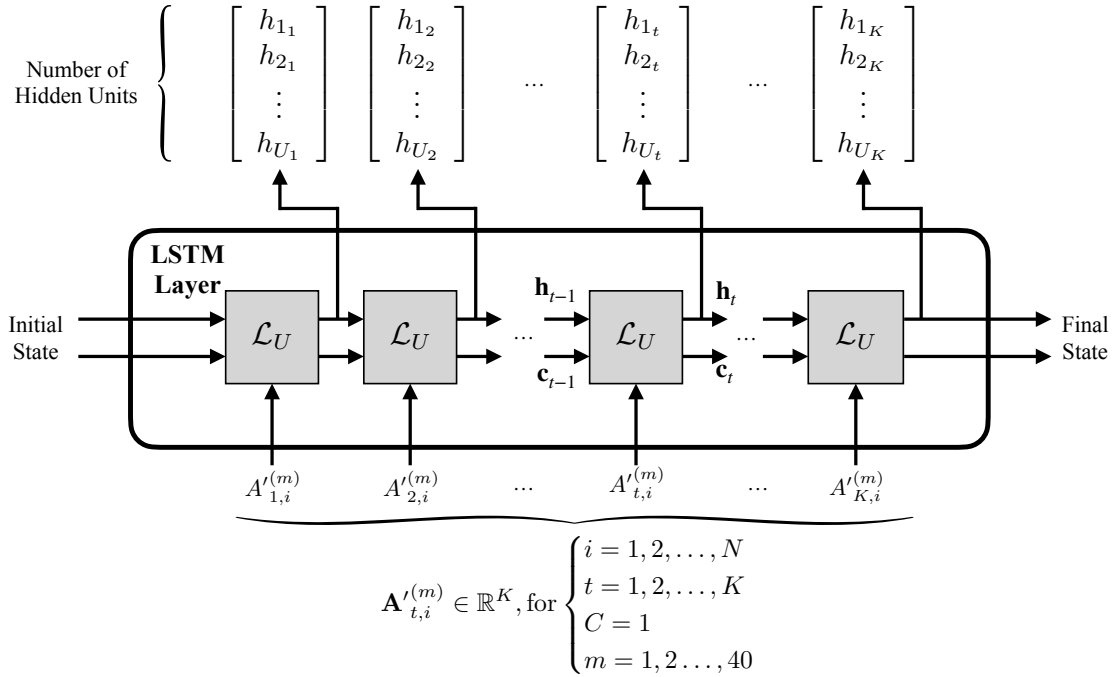
Figure 5.4: The architecture of the proposed LSTM layer.

The LSTM network can be made up of a single layer, $\mathcal{L}_U$, i.e, $\mathcal{S} = \{\mathcal{L}_U\}$ with hidden units, U, or multi-layer, $\mathcal{S} = \{\mathcal{L}_{U1}, \mathcal{L}_{U2}, \mathcal{L}_{U3}, \ldots\}$ with different number of hidden units, $U1, U2, U3, \ldots$, in each layer. For a single LSTM layer, the hidden and

cell states, with m examples and LSTM units U, are given by

$$(\mathbf{h}_t, \mathbf{c}_t) = \mathcal{L}_U(\mathbf{h}_{t-1}, \mathbf{c}_{t-1}, \mathbf{A}'^{(m)}_{t,i}), \text{for} \begin{cases} i = 1, 2, \ldots, N \\ t = 1, 2, \ldots, K \\ m = 1, 2, \ldots, 40 \end{cases} \quad (5.13)$$

Meanwhile, the output function of the LSTM multi-layer network, $\mathcal{S}$, is denoted by

$$(\mathbf{H}_t, \mathbf{C}_t) = \mathcal{S}(\mathbf{H}_{t-1}, \mathbf{C}_{t-1}, \mathbf{A}'^{(m)}_{t,i}), \text{for} \begin{cases} i = 1, 2, \ldots, N \\ t = 1, 2, \ldots, K \\ m = 1, 2, \ldots, 40 \end{cases} \quad (5.14)$$

As a result, the LSTM network presents K hidden states at the output, $\mathbf{h}_1, \mathbf{h}_2, \ldots, \mathbf{h}_t, \ldots, \mathbf{h}_K \in \pm\mathbb{U}^U$, increasing the network complexity by stacking several hidden outputs. However, it is important to find a single sequence at the output. For this purpose, dense layers can reduce from multiple inputs to a single output by an activation function either linear or non-linear. Figure 5.5 illustrates the proposed deep learning network, which connects the proposed LSTM network to the dense layer. To be precise, the obtained output is the predicted rain attenuation time-series, at the time step $t + 1$, $\hat{\mathbf{A}}'_{t+1,i} \in \mathbb{R}^K$.
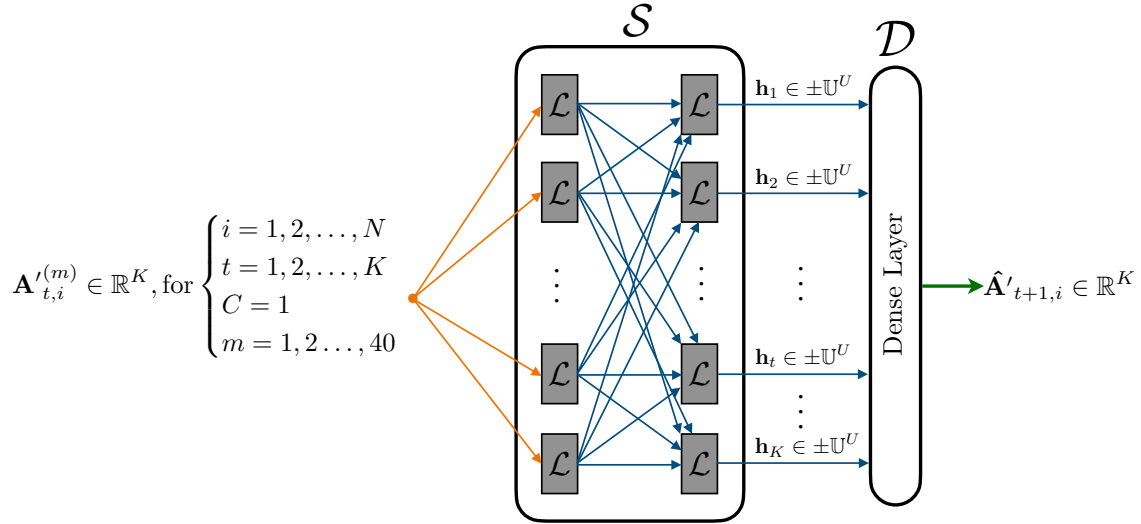
Figure 5.5: The architecture of the proposed deep learning network.

For readability and simplicity, the proposed LSTM network is analyzed as a single LSTM layer, $\mathcal{L}_U$, where each output, also known as the hidden state at time step t, is a U-dimensional vector, $\mathbf{h}_t \in \pm\mathbb{U}^U$. The LSTM outputs become the inputs of the dense layer. In this context, the dense layer is a deeply connected neural network, where each connection can be typically considered as a multiple-input neuron [81,82]. Usually, the neuron's output can be denoted by $y = f(\mathbf{W} \cdot \mathbf{p} + b)$, where $\mathbf{W}$ is the weight matrix, b is the bias, f is the activation function, and $\mathbf{p}$ is the input

vector [81–83]. In this thesis, the dense layer can be mathematically expressed as

$$\hat{A}'_{2,i} = \text{selu}(\mathbf{w_{d_1}}^\mathsf{T} \cdot \mathbf{h}_1 + b_{d_1}) \in \mathbb{R}$$
$$\hat{A}'_{3,i} = \text{selu}(\mathbf{w_{d_2}}^\mathsf{T} \cdot \mathbf{h}_2 + b_{d_2}) \in \mathbb{R}$$
$$\vdots$$
$$\hat{A}'_{t+1,i} = \text{selu}(\mathbf{w_{d_t}}^\mathsf{T} \cdot \mathbf{h}_t + b_{d_t}) \in \mathbb{R}$$
$$\vdots$$
$$\hat{A}'_{K+1,i} = \text{selu}(\mathbf{w_{d}}_K^\mathsf{T} \cdot \mathbf{h}_K + b_{d_K}) \in \mathbb{R}$$

where each value, $\hat{A}'_{t+1,i}$, is stored in the output vector. Therefore, the output of the dense layer is encapsulated and rewritten as

$$\hat{\mathbf{A}}'_{t+1,i} = \mathcal{D}(\mathbf{h}_t) \in \mathbb{R}^K, \text{for} \begin{cases} i = 1, 2, \ldots, N, \\ t = 1, 2 \ldots, K, \end{cases} \tag{5.15}$$

where $\mathcal{D}$ is the dense layer function and $\mathbf{h}_t \in \pm \mathbb{U}^U$ for $t = 1, 2, \ldots, K$, are the input vectors of the dense layer. The scaled-exponential-linear-unit (SELU) activation function is employed in this layer, which is discussed in more detail in Section 5.2.2. Moreover, $\mathbf{W_d} \in \mathbb{R}^{U \times K}$ is the weight matrix that contains each weight vector $\mathbf{w_{d_t}} \in \mathbb{R}^U$ and $\mathbf{b_d} \in \mathbb{R}^K$ is the bias vector that includes each bias element $b_{d_t} \in \mathbb{R}$. Similarly to the LSTM network, the weight parameters of the dense layer are also learned during the training process. Furthermore, the weight parameters of the dense layer can be combined under one symbol $\mathbf{\Theta}_\mathcal{D}$ [79], which is given by

$$\mathbf{\Theta}_\mathcal{D} \equiv \{\mathbf{W_d}, \mathbf{b_d}\}. \tag{5.16}$$

Finally, the output vectors obtained from the proposed deep learning network can be stacked in the matrix, $\hat{\mathbf{A}}' \in \mathbb{R}^{K \times N}$, whose predicted values of rain attenuation for each GW's feeder uplink are contained within the matrix. To be specific, these values allow the Network Control Center (NCC) to know the feeder uplink status in advance, managing resources, e.g. gateway redundancy, to avoid link outages due to the heavy rain.

5.2.2   Deep Learning Network: Model Description

A. Activation Functions

The activation function is used to determine the nature of the output of a neural network, in addition to limiting the amplitude of the output of a neuron. That is, it can map the outcome values between 0 to 1, -1 to 1, yes or no, etc., depending upon the type of activation function. For this reason, the activation function can be divided into two types, linear and non-linear activation functions. Generally, the most frequent activation functions are non-linear functions because they can facilitate the generalization and adaptation of the model with a lot of varied data. The activation functions are also known as transfer functions and/or squashing functions [83, 84].

Usually, the most employed activation functions are in the following.

- **Sigmoid Activation Function:** the sigmoid function, also known as logistic activation function, is especially used for models that are able to predict the probability at the output. For this purpose, the sigmoid function always returns a value between 0–1, therefore, it is ideal for probabilistic outputs [85]. The sigmoid activation function, $\sigma(z)$, is given by

$$\sigma(z) = \frac{1}{1 + \exp(-z)} \tag{5.17}$$

Figure 5.6 depicts the sigmoid function, where, for small values ($z < -5$), the results of the sigmoid function get close to zero, and for large values ($z > 5$) the sigmoid function returns values close to 1.
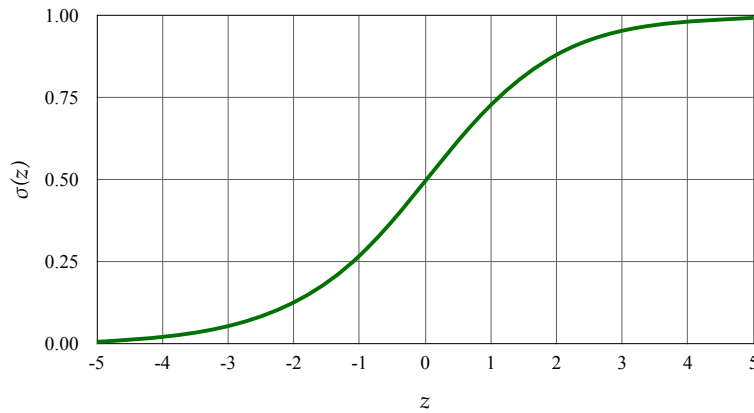
Figure 5.6: Sigmoid activation function.

The sigmoid function is differentiable, therefore, the slope of the sigmoid curve can be found at any two points. However, it is important to mention that the sigmoid function could provoke a jam at the training process [83]. Also, it is possible to assume that the sigmoid function is similar to a 2-element Softmax, where the second element is zero. Indeed, the softmax activation function for multiclass classification problems is based on the sigmoid function but with n-elements [85].

- **Hyperbolic Tangent Activation Function:** the hyperbolic tangent activation function (tanh) is similar to sigmoid function but with a wider range, which varies from -1 to 1. In this case, the negative inputs are directly mapped in the negative range whereas the zero inputs are mapped close to zero in the tanh function. Naturally, this is the main advantage of the tanh activation function. The tanh function is expressed as

$$\tanh(z) = \frac{\sinh(z)}{\cosh(z)} = \frac{1}{1 + \exp(-2z)} - 1 \tag{5.18}$$

Figure 5.7 illustrates the tanh function, where it is possible to distinguish the range between -1 to 1.
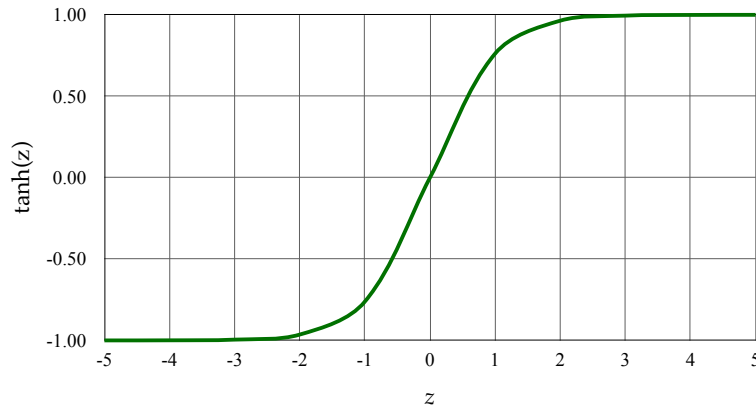
Figure 5.7: Hyperbolic tangent activation function.

It is important to mention that the tanh function is differentiable, in addition to being mainly used in classification problems, especially, between two classes. Both sigmoid and tanh activation functions are used in feed-forward neural networks [83, 85].

- **Rectifier-Linear-Unit Activation Function:** it is also known as ReLU, which is one of the most popular activation functions to use in machine learning algorithms. This activation function is especially employed in deep learning and convolutional neural networks [83]. The ReLU activation function expression is given by

$$R(z) = \max(0, z) = \begin{cases} 0 & \text{for } z < 0 \\ z & \text{for } z \geq 0 \end{cases} \tag{5.19}$$

Figure 5.8 shows the ReLU activation function, which ranges from 0 to ∞. In other words, the ReLU is half rectified, i.e., $R(z) = 0$ when z is less than zero ($z < 0$) and $R(z) = z$ when z is above or equal to zero ($z \geq 0$) [85].

However, this activation function can become a problem if there are negative input values, which turn into zero values. In a sense, this issue can affect the ability of the model to train or fit from the data. For this reason, the input data must be previously analyzed to apply the proper activation function.

- **Scaled-Exponential-Linear-Unit Activation Function:** it is also known as SELU activation function, which is defined as

$$\text{selu}(z) = \lambda_{selu} \cdot \begin{cases} z & \text{for } z \geq 0 \\ \alpha_{selu}[\exp(z) - 1] & \text{for } z < 0 \end{cases}, \tag{5.20}$$

where λ_{selu} and α_{selu} are pre-defined constants ($\lambda_{selu} = 1.05070098$ and $\alpha_{selu} = 1.67326324$) [85]. For the sake of simplicity, the SELU activation function
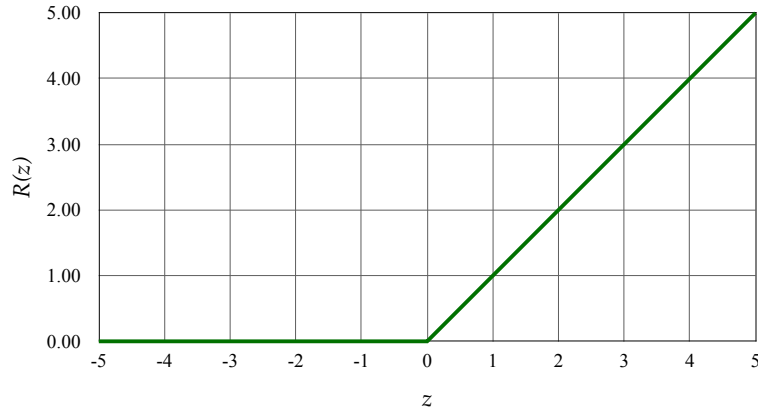
Figure 5.8: Rectifier-Linear-Unit activation function.

multiplies scale ($\alpha_{selu} > 1$) with the exponential and the linear functions to assure a slope larger than 1 for positive inputs.

Figure 5.9 depicts the SELU activation function. The values of λ_{selu} and α_{selu} are chosen so that the mean and variance of the inputs are preserved between two consecutive layers as long as the weights are initialized correctly, in addition to the number of input units is large enough [85, 86].
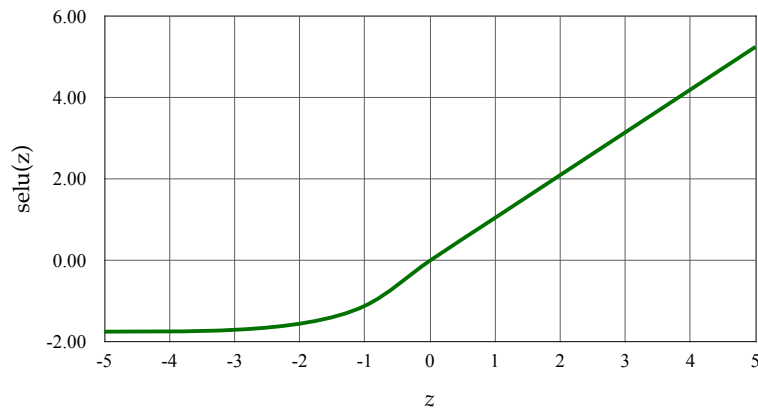
Figure 5.9: Scaled-Exponential-Linear-Unit activation function.

Self-normalizing neural networks (SNN) use the SELU activation function, which is able to enable high-level abstract representations. SELU activation functions induce self-normalizing properties, improving the convergence and accuracy, in addition to being widely used in machine learning and deep learning models. [86].

To sum up, the choice of the best activation function depends on the type and nature of input data, which translates into better convergence, accuracy, and generalization of the neural network model. Therefore, each activation function must be rigorously tested to find a strong and functional model.

B. Feature Scaling

To begin with, the rain attenuation time-series for each i-th GW, $\mathbf{A}_{t,i}^{(m)} \in \mathbb{R}^K$, is pre-processed by using feature scaling, also known as normalization, which is expressed by

$$\mathbf{A'}_{t,i}^{(m)} = \frac{\mathbf{A}_{t,i}^{(m)} - \min_{1 \leq t \leq K} \mathbf{A}_{t,i}^{(m)}}{\max_{1 \leq t \leq K} \mathbf{A}_{t,i}^{(m)} - \min_{1 \leq t \leq K} \mathbf{A}_{t,i}^{(m)}}, \text{for} \begin{cases} i = 1, 2, \ldots, N \\ t = 1, 2, \ldots, K \\ m = 1, 2, \ldots, 40 \end{cases}, \qquad (5.21)$$

where $\mathbf{A'}_{t,i}^{(m)} \in \mathbb{R}^K$ and each component $A'_{t,i}^{(m)}$ corresponds to a time step, t. This process is carried out for each example sequence (m) from dataset $\boldsymbol{A}_i$. The main advantage of feature scaling is that the gradient descent converges much faster with normalization than without it. Normalization is often employed in neural networks when the distribution of data is not a Gaussian distribution. In this case, the nature of rain attenuation data follows a log-normal distribution [28, 38].

In summary, the normalized rain-attenuation time-series are ready to be employed at the input layer of the LSTM network.

C. Initialization of Biases and Weights

The values of weights are usually initialized by random values, whereas the default value for the bias is 1. However, the initialization could manually be changed. The weights can be represented by concatenated matrices (Θ), where their dimensions depend on how deep is the neural network and the number of features of the hypothesis function.

D. The Loss Function

The loss functions are a measure in order to understand how well a model is able to predict the expected outcome [84]. It is important to mention that there is not a unique loss function, therefore, the choice depends on multiple factors such as the type of machine learning algorithm, presence of outliers, differentiable loss functions, the efficiency of optimization algorithms, and accurate predictions. Depending on the machine learning problem, loss functions must be for either regression or classification [80]. In order to predict the rain attenuation time-series, the chosen machine-learning-algorithm must be based on a regression problem, therefore, the loss functions for regression are considered in this thesis.

To begin with, a model is built from the proposed deep learning network (Section 5.2.1), whose performance is evaluated by a loss function. In this context, the loss function evaluates the differences between predicted and observed values, reaching the minimum when the prediction is exactly equal to the observed (true) value. For this purpose, the mean absolute error (MAE) is a loss function used for regression, which is more robust to outliers [84]. That is, rain-attenuation datasets contain outliers due to the nature of the rain, therefore, the MAE loss function is useful in these cases. In

general terms, the MAE loss function is given by

$$L(\mathbf{\Theta})_i = \frac{1}{m} \sum_{j=1}^{m} |A'^{(j)}_{t,i} - \hat{A}'_{t,i}|, \begin{cases} i = 1, 2, \ldots, N \\ j = 1, 2, \ldots, m \\ t = 1, 2, \ldots, K \end{cases} \qquad (5.22)$$

where the parameter $\mathbf{\Theta}$ is implicit in the predicted values $\hat{A}'_{t,i}$. During the training process, the learning of the parameter $\mathbf{\Theta}$ is continuous so that the output can have a better fit and the model can be more accurate. Furthermore, it is important to note that the parameter $\mathbf{\Theta}$ is comprised of $\mathbf{\Theta}_{\mathcal{L}}$ and $\mathbf{\Theta}_{\mathcal{D}}$, where each parameter is updated in its respective training process. The loss function can be applied to both the training and validation process. Thus, the model can be evaluated by the training loss function, $L(\mathbf{\Theta})_{train}$, and the validation loss function $L(\mathbf{\Theta})_{val}$.

E. Optimization Algorithms

Machine Learning algorithms depend on maximizing or minimizing a function. In this case, the loss function is minimized by optimization algorithms in order to find the best performance and the minimum of the function. The main optimization algorithms are presented in the following items.

- **Stochastic Gradient Descent Algorithm:** this algorithm updates the parameter $\mathbf{\Theta}$ to minimize the loss function in the direction of its negative gradient by taking small steps [82–84]. The update algorithm of the parameter $\mathbf{\Theta}$ is denoted by

$$\mathbf{\Theta}_{\ell+1} := \mathbf{\Theta}_\ell - \alpha \nabla_{\mathbf{\Theta}} L(\mathbf{\Theta}_\ell), \qquad (5.23)$$

  where ℓ is the iteration number and α is the step size or learning rate. The learning rate setting could be quite tricky. For instance, if the learning rate is constant, $\alpha > 0$, but its value is too small, convergence can be very slow, but if the value is too large, the method can fail to converge at all [84].

  In general, this algorithm evaluates the function gradient and updates the parameter $\mathbf{\Theta}$ by using a subset derived from the training set. Usually, the subset is also known as mini-batch [84], whose gradient evaluation using the mini-batch is performed by each iteration ℓ. During each iteration, the algorithm is one step closer to minimizing the loss function. Finally, the full-pass when the training algorithm ends up its process in all mini-batches is an epoch.

- **Root Mean Square Propagation (RMSProp):** this algorithm tries to improve network training by using different learning rates, α. That is, the RMSProp algorithm can automatically adapt to the loss function, optimizing the training process in addition to updating the parameter $\mathbf{\Theta}$ efficiently [87]. A moving average of the element-wise squares of the parameter gradients is kept by this algorithm, which is given by

$$v_\ell = \beta_2 v_{\ell-1} + (1 - \beta_2)[\nabla_{\mathbf{\Theta}} L(\mathbf{\Theta}_\ell)]^2, \qquad (5.24)$$

where β_2 is the decay factor rate, whose value usually can be 0.9, 0.99, or 0.999. This moving average is used by the RMSProp algorithm to normalize the updates of the parameter Θ, individually. Parameter Θ is normalized and updated by the following expression

$$\Theta_{\ell+1} := \Theta_\ell - \frac{\alpha \nabla_\Theta L(\Theta_\ell)}{\sqrt{v_\ell} + \epsilon}, \tag{5.25}$$

where ϵ is a small constant in order to avoid division by zero. By using RMSProp algorithms, the learning rate decreases with larger gradients and increases with small gradients [87].

- **Adaptive Moment Estimation Optimizer (ADAM):** the adaptive moment estimation algorithm is a stochastic gradient-descent algorithm with momentum which keeps an element-wise moving average of both parameter gradients and their squared values [87]. These average values can be expressed by

$$m_\ell = \beta_1 m_{\ell-1} + (1 - \beta_1) \nabla_\Theta L(\Theta_\ell), \tag{5.26}$$

$$v_\ell = \beta_2 v_{\ell-1} + (1 - \beta_2)[\nabla_\Theta L(\Theta_\ell)]^2, \tag{5.27}$$

where gradient decay factors, β_1 and β_2, are linear and quadratic respectively. Also, $\nabla_\Theta L(\Theta_\ell)$ is the gradient of the loss function, and ℓ is the iteration number. ADAM optimizer uses these averages to update the parameter Θ, using the following expression

$$\Theta_{\ell+1} := \Theta_\ell - \alpha \frac{m_\ell}{\sqrt{v_\ell} + \epsilon}, \tag{5.28}$$

where $\alpha > 0$ is the learning rate, and ϵ is a small constant added in order to avoid division by zero. In this algorithm, the moving average of the gradient enables the parameter Θ updates, picking up the momentum in a definite direction as long as gradients throughout many iterations are similar. Also, the moving average and parameter Θ can become smaller whether the gradients are noisy. In general, there is not a specific learning rate, therefore, different learning rates are tried out to find the optimal values. It can be stipulated a different learning rate for each layer. Finally, the ADAM optimizer is more efficient than RMSProp and stochastic gradient descent algorithms, especially due to the fast convergence and adaptability [87].

F. L2 Regularization

The overfitting can be reduced by adding a regularization term for the weights of the loss function $L(\Theta)$ [87]. Therefore, the loss function with the regularization term is defined as

$$L(\Theta)_R = L(\Theta) + \lambda_R \Omega(\Theta), \tag{5.29}$$

where λ_R is the regularization coefficient, and $\Omega(\boldsymbol{\Theta})$ is the regularization function. Thus, the regularization function is given by vector notation, which is represented by

$$\Omega(\boldsymbol{\Theta}) = \frac{1}{2}\boldsymbol{\Theta}^{\mathsf{T}}\boldsymbol{\Theta} \tag{5.30}$$

It is important to mention that the biases are not regularized. The λ_R coefficient can manually be modified, also, it is possible to specify different regularization coefficients for different layers.

G. Dropout Regularization

Dropout is a regularization method that is capable of dropping out inputs to a layer by probabilistically removing. To be specific, dropout simulates a large number of networks but with different structures. Thus, nodes in the network are more robust to the inputs. For this purpose, the probability of establishing each input to zero is determined in the layer which is also known as the dropout rate.

For instance, if a dropout rate sets at 0.8, it means that 20% of inputs are to zero. Therefore, dropout is a computationally-low-cost method to regularize a deep learning network, to reduce the overfitting, and to improve the generalization error at the LSTM network.

H. Training Process

By setting the network hyperparameters, the model, let $\mathcal{F}$, is trained by the proposed deep learning network to forecast rain attenuation time-series in K-time steps into the future. In this case, the used method is many-to-one, where the input dataset, $\boldsymbol{A}'_i$, is comprised of multiple time-series,

$$
\begin{aligned}
\mathbf{A}'^{(1)}_{t,i} &= [A'^{(1)}_{1,i}, A'^{(1)}_{2,i}, \ldots, A'^{(1)}_{t,i}, \ldots, A'^{(1)}_{K,i}] \in \mathbb{R}^K \\
\mathbf{A}'^{(2)}_{t,i} &= [A'^{(2)}_{1,i}, A'^{(2)}_{2,i}, \ldots, A'^{(2)}_{t,i}, \ldots, A'^{(2)}_{K,i}] \in \mathbb{R}^K \\
&\vdots \\
\mathbf{A}'^{(m)}_{t,i} &= [A'^{(m)}_{1,i}, A'^{(m)}_{2,i}, \ldots, A'^{(m)}_{t,i}, \ldots, A'^{(m)}_{K,i}] \in \mathbb{R}^K
\end{aligned}
\quad , \text{ for }
\begin{cases}
i = 1, 2, \ldots, N \\
t = 1, 2, \ldots, K \\
m = 1, 2, \ldots, 40
\end{cases} \quad ,
$$

and the single time-series obtained from the deep learning network at the output is given by

$$\hat{\mathbf{A}}'_{t+1,i} = [\hat{A}'_{2,i}, \hat{A}'_{3,i}, \ldots, \hat{A}'_{t+1,i}, \ldots, \hat{A}'_{K+1,i}] \in \mathbb{R}^K, \text{ for } \begin{cases} i = 1, 2, \ldots, N \\ t = 1, 2, \ldots, K \end{cases}$$

Here, the feature scaling must be undone according to the feature range parameters calculated earlier (sub-section 5.2.2-*Feature Scaling*) [88]. As a result, each rain-attenuation time-series is denoted by $\hat{\mathbf{A}}_{t+1,i} \in \mathbb{R}^K$.

I. Metrics

The proposed regression model is based on supervised learning, which must be estimated and evaluated in its performance and fit. Usually, three metrics are used for this purpose, such as the root mean squared error (RMSE), mean absolute error (MAE), and the coefficient of determination (R-Squared or R^2).

- **Root Mean Squared Error:** this metric is the most commonly used in regression problems, which indicates how well the model fits the data. That is, how near the observed values are from the predicted values, providing an absolute measure of fit. The RMSE is given by

$$\text{RMSE}_i = \sqrt{\frac{1}{K} \sum_{j=1}^{K} (A_{j,i} - \hat{A}_{j,i})^2}, \text{for } i = 1, 2, \ldots, N \qquad (5.31)$$

  To be precise, the RMSE represents the square root of the differences between observed and predicted values. In other words, it is the quadratic mean of these differences [82–84]. For calculations over the data sample, these deviations are known as residuals, whereas they are called errors for out-of-sample calculations. In general, a lower RMSE value indicates a better fit and accuracy of the model to predict, which is the most important criterion in prediction models. However, it is important to mention that RMSE is sensitive to outliers [89].

- **Mean Absolute Error:** it is the arithmetic average of the absolute errors, i.e., between observed and predicted values. This statistical metric is often used as a measure of forecast error in the time-series analysis [89]. The MAE is calculated as

$$\text{MAE}_i = \frac{1}{K} \sum_{j=1}^{K} |A_{j,i} - \hat{A}_{j,i}|, \text{for } i = 1, 2, \ldots, N \qquad (5.32)$$

  Both RMSE and MAE metrics express the average prediction error for LSTM models. Furthermore, both metrics are indifferent to the direction errors, i.e., RMSE and MAE are negatively-oriented scores, which means lower values are much better. Finally, it is important to mention that MAE is a linear score in addition to being more robust to outliers [84].

- **Coefficient of Determination:** it is also known as R-Squared, R^2, which is used in the context of statistical models. Indeed, the main purpose is either the prediction of future results or the testing of hypotheses, on the basis of other related information. That is, it is implemented as a measure of how well the observed outcomes are replicated by the model, based on the proportion of total variation of outcomes explained by the model [90]. The R-Squared is computed as

$$R_i^2 = 1 - \frac{\sum_{j=1}^{K} (A_{j,i} - \hat{A}_{j,i})^2}{\sum_{j=1}^{K} (A_{j,i} - \bar{A}_{j,i})^2}, \text{for } i = 1, 2, \ldots, N \qquad (5.33)$$

In other words, the coefficient of determination is employed to indicate the goodness of fit of the LSTM model. In this context, R^2 could be employed as an accuracy metric where a value of about 1 indicates that the data predictions perfectly fitted the proposed model, whereas an $R^2 = 0$ indicates that the proposed model did not improve the predictions [90].

J. CNIR Time-series Calculation

Predicted by the deep learning network, the rain attenuation time-series are trained and denoted by $\hat{\mathbf{A}}'_{t+1,i} = \mathcal{F}(\mathbf{A}'^{(m)}_{t,i})$ for each GW location, $i = 1, 2, \ldots, N$. As previously stated, the normalization must be undone so the time-series can be expressed on the original scale. Thus, rain attenuation time-series can be given by $\hat{\mathbf{A}}_{t+1,i} \in \mathbb{R}^K$. By using Eq. (2.3), the predicted sequence of CNR time-series for each feeder uplink can be expressed by

$$\hat{\mathbf{\Gamma}}_{t+1,i} = 10 \log_{10}(\gamma_{cs_i}) - \hat{\mathbf{A}}_{t+1,i}, \text{ for } \begin{cases} i = 1, 2, \ldots, N \\ t = 1, 2, \ldots, K \end{cases} \tag{5.34}$$

where $\hat{\mathbf{\Gamma}}_{t+1,i} \in \mathbb{R}^K$ and each element, $\hat{\Gamma}_{t+1,i}$, is given in decibels, dB. Finally, substituted the predicted CNR into Eq. (2.6), the predicted sequence of CNIR time-series is calculated for each feeder uplink and rewritten as

$$\hat{\mathbf{\Xi}}_{t+1,i} = \frac{\hat{\mathbf{\Gamma}}_{t+1,i} \cdot \zeta_T}{\hat{\mathbf{\Gamma}}_{t+1,i} + \zeta_T}, \text{ for } \begin{cases} i = 1, 2, \ldots, N \\ t = 1, 2, \ldots, K \end{cases} \tag{5.35}$$

where $\hat{\mathbf{\Xi}}_{t+1,i} \in \mathbb{R}^K$ is the CNIR prediction for the next time step, $t + 1$. Figure 5.10 depicts a block diagram of the proposed method where each GW processes its both rain-attenuation and CNIR predictions to send them to the Network Control Center (NCC), At NCC, each predicted time-series component of both rain attenuation and CNIR can be stored into matrices, $\hat{\mathbf{A}}, \hat{\mathbf{\Xi}} \in \mathbb{R}^{K \times N}$, respectively. Thus, the NCC analyzes each feeder-uplink status in order to determine which of them are threatened in advance by rain impairments.

5.3   Experimentation

In order to prove the deep learning network performance, two experiments were executed by employing a high-level programming language. For this purpose, 24 locations were chosen as possible GW sites, therefore, there were obtained 24 rain attenuation datasets with 40 sequences for each one of them. In this context, the possible GW-sites are dispersed in Mexico, Central America, and The Caribbean, as these cities can access easier to high-quality services and infrastructures so the implementation and deployment can be faster and more efficient than in minor cities. Furthermore, the number of examples, m, emulates a historical database of 40 years. Table A.2 (Appendix A.2) shows in detail the main features of each GW site, in
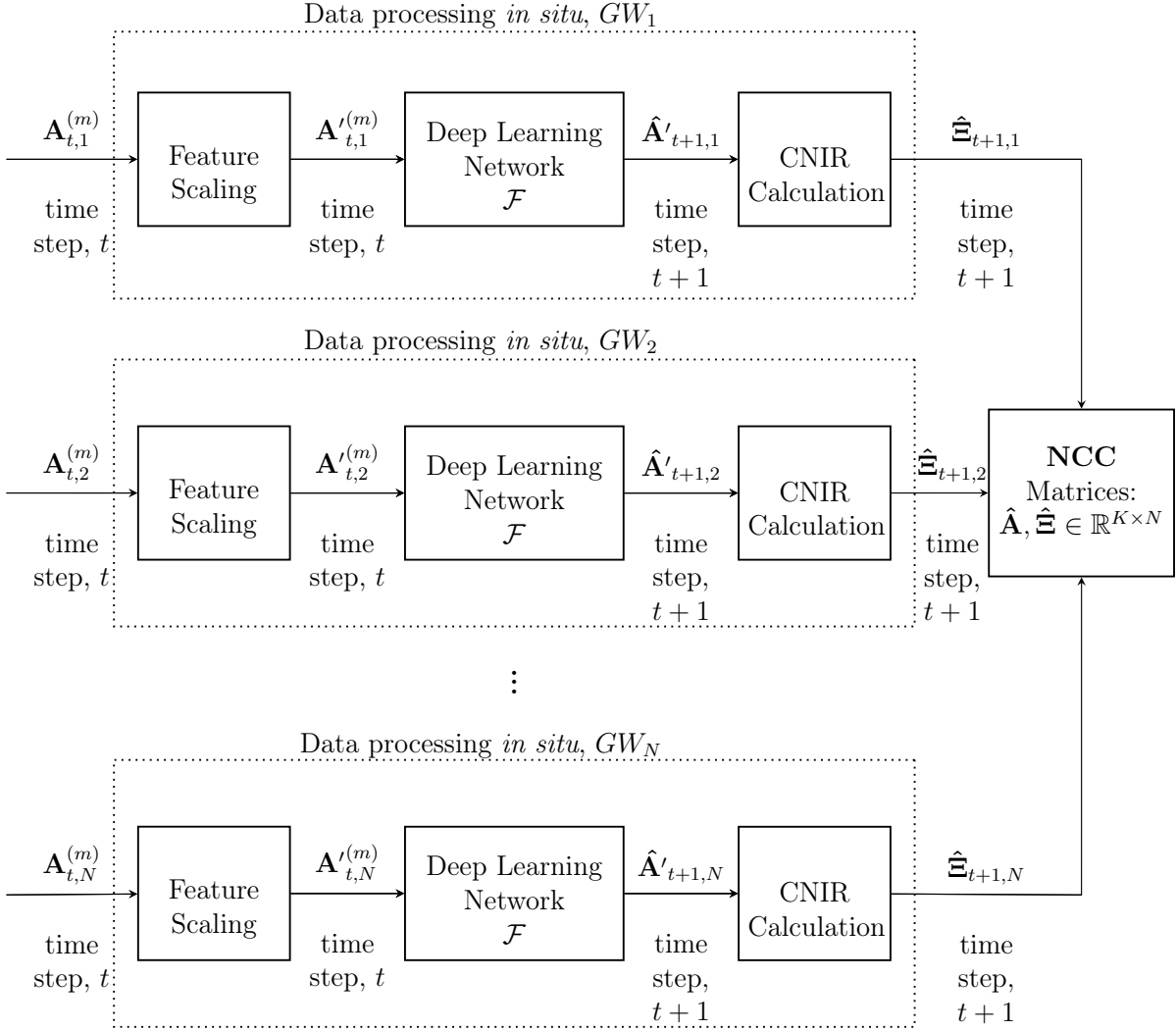
Figure 5.10: Block diagram of the proposed method based on the deep learning network.

---

addition to its calculated carrier-to-noise ratio under clear-sky conditions according to the discussed method in Chapters 2 and 3, γ_{cs_i}, for $i = 1, 2, \ldots, N$ [dB]. In this context, a lot of time was invested by computer coding to carry out the experiments successfully. Provided in the following sub-sections, each experiment details the employed settings and procedure.

5.3.1 Experiment 1: Training and validation subsets partitioning, 70/30

To begin with, the rain attenuation datasets for the set $[N] = \{1, 2, \ldots, 24\}$ were calculated by using the model presented in sub-section 2.4. This model employed

geographic coordinates (latitude, longitude, and height) of each GW site, satellite orbital position at 92° West, the frequency band of the feeder uplink at 50 GHz, and $T_s = 1$ min. It is important to highlight that the rain attenuation time-series were sampled every $T_s = 1$ min at 1 year period, therefore, the number of samples of each rain-attenuation time-series is 525600, that is, each sequence has a dimensionality of $K = 525600$.

Each time-series was partitioned into training and validation subsets, where the training subset was 70% and the validation subset was 30%. Hereinafter, each rain attenuation time-series was normalized by feature scaling to be trained and validated in the deep learning network. Table 5.1 shows the hyperparameters that are incorporated into the deep learning network configuration. To be precise, the hyperparameters adjustment is an important role in the learning process. For this purpose, different values were assigned to each hyperparameter such as the number of hidden layers, dropout rate, number of LSTM units, learning rate, etc. In this case, the deep learning network employed a single LSTM layer, $\mathcal{S} = \{\mathcal{L}_U\}$. After several trials, where about 400 models were tried out with different hyperparameter combinations, the best model was found according to the best hyperparameters. In summary, this deep learning network configuration was able to train and validate 960 rain attenuation time-series regarding 24 GW sites with 40 examples by the site-specific.

Table 5.1: Hyperparameters for Experiment 1

Parameter	Arg./Value	Parameter	Arg./Value
LSTM units, U	100	Dense Layer: $(\mathcal{D})$ output	1
Activation Function $(\mathcal{L}_U)$	tanh	Activation Function $(\mathcal{D})$	selu
L2 λ_R	1×10^{-4}	β_1	0.9
Dropout	0.2	β_2	0.999
Loss Function	MAE	ϵ	1×10^{-8}
Optimizer	ADAM	Metrics	RMSE, MAE, R^2
Learning rate	5×10^{-3}	Validation	Yes
Epochs	250	Batch Size	1024
Early Stopping	Yes	Patient	5

5.3.2 Experiment 2: Training and validation subsets partitioning, 90/10

This procedure was similar to Experiment 1, but the rain attenuation time-series were divided into 90% for the training subsets and 10% for the validation subsets. Unlike in Experiment 1, the number of hidden units increased in the LSTM layer. Also, the LSTM network was modified by adding more layers. Therefore, the LSTM multi-layer network contributed to the proposed model to be deeper than Experiment 1. Thus, the deeper network might need fewer epochs to train the model, but the computational cost might be higher.

Table 5.2 indicates the obtained hyperparameters for Experiment 2. Similarly, the hyperparameters tuning was performed according to the Experiment 1 process. However, it was necessary to test about 600 models to find the best hyperparameters that are part of the model settings for Experiment 2. It is important to mention that the deep learning network is comprised of 5 LSTM layers, where each layer of the LSTM multi-layer network, $\mathcal{S} = \{\mathcal{L}_{U1}, \mathcal{L}_{U2}, \mathcal{L}_{U3}, \mathcal{L}_{U4}, \mathcal{L}_{U5}\}$, such that $U1 = 200, U2 = 75, U3 = 50, U4 = 25, U5 = 5$ has its own LSTM hidden units, respectively.

Table 5.2: Hyperparameters for Experiment 2

Parameter	Arg./Value	Parameter	Arg./Value
LSTM units, $U1$	200	LSTM units, $U2$	75
Activation Function ($\mathcal{L}_{U1}$)	tanh	Activation Function ($\mathcal{L}_{U2}$)	tanh
LSTM units, $U3$	50	LSTM units, $U4$	25
Activation Function ($\mathcal{L}_{U3}$)	tanh	Activation Function ($\mathcal{L}_{U4}$)	tanh
LSTM units, $U5$	5	Dense Layer: ($\mathcal{D}$) output	1
Activation Function ($\mathcal{L}_{U5}$)	tanh	Activation Function ($\mathcal{D}$)	selu
L2 λ_R	1×10^{-6}	β_1	0.9
Dropout	0.2	β_2	0.999
Loss Function	MAE	ϵ	1×10^{-8}
Optimizer	ADAM	Metrics	RMSE, MAE, R^2
Learning rate	1×10^{-3}	Validation	Yes
Epochs	250	Batch	1024
Early Stopping	Yes	Patient	5

5.4   Results

Both experiments were performed by computer resources to train and validate the proposed models, where Python programming language was employed, in addition to using tensor processor units (TPU) and graphics processor units (GPU) to accelerate the training and validation processes, reducing the computing time and improving the general performance. In order to evaluate both experiments, three statistical metrics were used for this purpose: root mean squared error (RMSE), mean absolute error (MAE), and the coefficient of determination (R^2).

Figure 5.11 and Figure 5.12 depict RMSE scores for both training and validation subsets, respectively. In both cases, the best results were obtained by Experiment 2. However, some RMSE scores for training subsets that were evaluated in each site by Experiment 1 such as San Jose, Tegucigalpa, Guadalajara, La Habana, and Belmopan were lower than RMSE scores from Experiment 2, without having a remarkable difference for all reported cases. Furthermore, for validation experiments, some RMSE scores from Experiment 1 such as Tijuana, Torreon, La Paz B.C., Tuxtla Gtz., San Pedro Sula, Belmopan, Kingston, and Oaxaca were also lower than RMSE scores from Experiment 2. Anyway, the average RMSE score obtained from Experiment 2 was lower than Experiment 1.
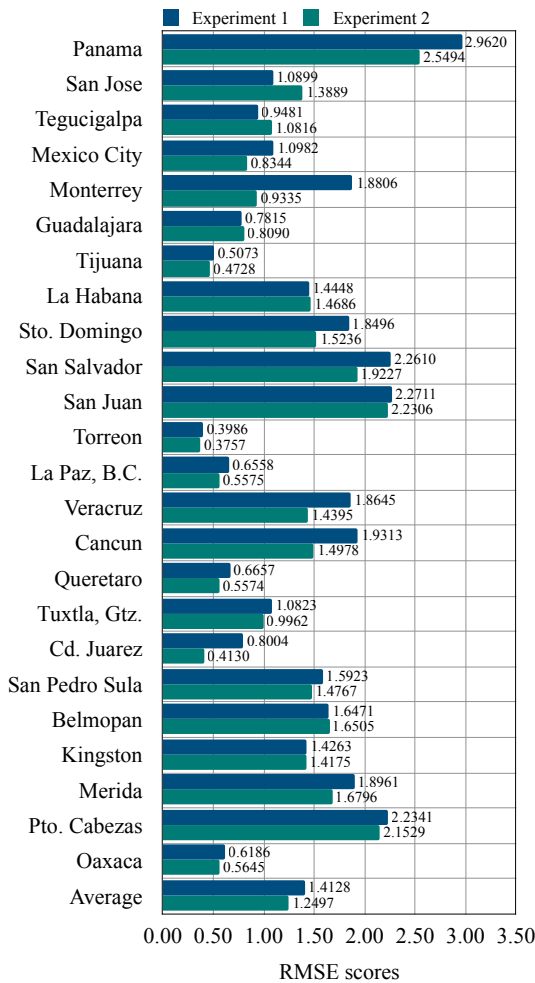
Figure 5.11: RMSE scores for training subsets.
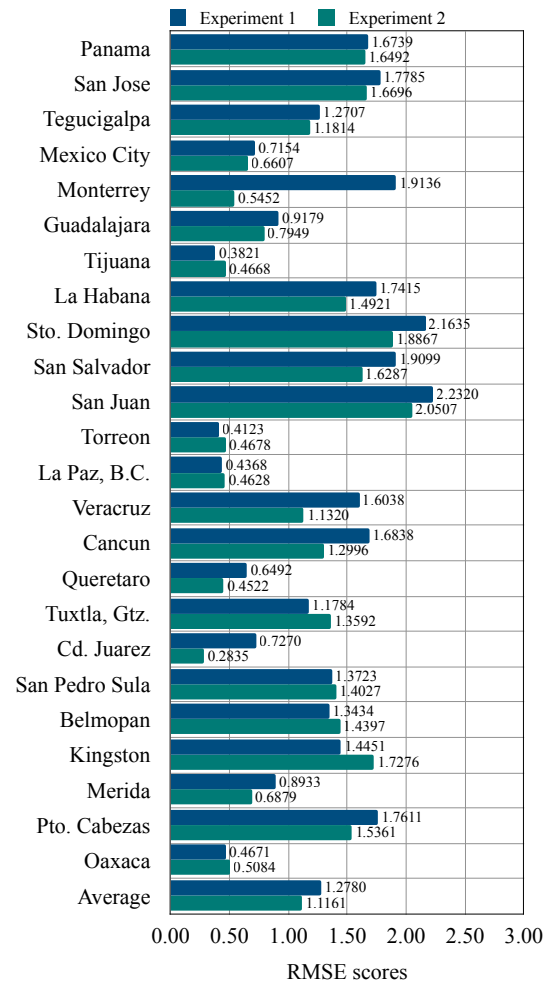
Figure 5.12: RMSE scores for validation subsets.

Figure 5.13 and Figure 5.14 show MAE scores for training and validation subsets, respectively. For both training and validation subsets, the MAE scores were closely similar to each other. Here, the average MAE score from Experiment 2 was lower than Experiment 1 for both training and validation evaluations. Nevertheless, some MAE scores from Experiment 1 were lower than Experiment 2, but these scores did not influence strongly in the final average score. In many cases, RMSE scores are larger than MAE scores, but if the errors have the same magnitude, then RMSE=MAE.

Figure 5.15 and Figure 5.16 illustrate the training and validation rain attenuation subsets of each site, respectively. In order to visualize properly, 50 samples were picked out by each training and validation figure. That is, each range was randomly chosen by illustrating rain attenuation samples. Furthermore, each figure, either training or validation subset, depicted both Experiments and the Observed data. In this sense, results from Experiment 2 were adequately fitted better than Experiment 1. For instance, although Tijuana training and validation subsets, Figure 5.15g and Figure 5.16g respectively, were practically the same for both experiments, other evaluations
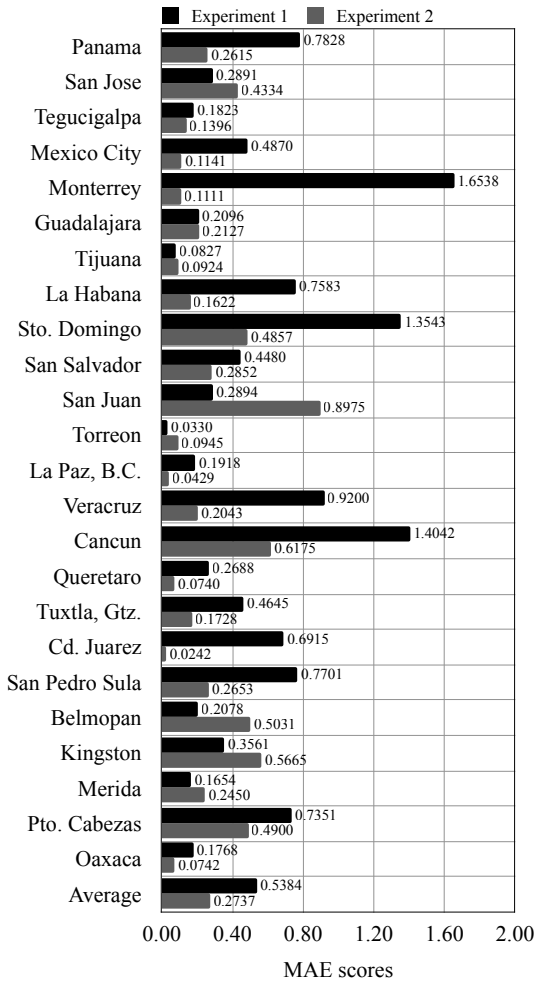
Figure 5.13: MAE scores for training subsets.
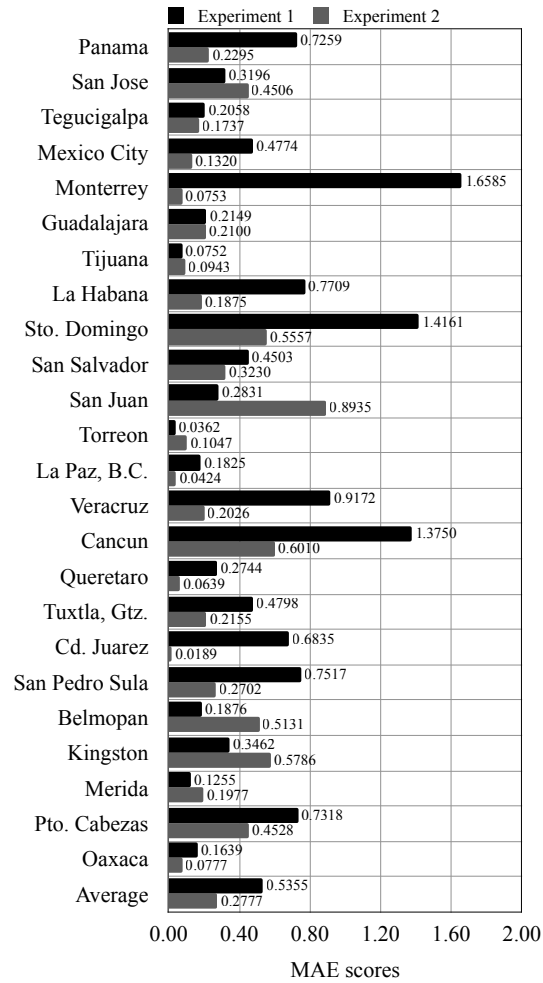
Figure 5.14: MAE scores for validation subsets.

such as Monterrey (Figure 5.15e and Figure 5.16e) or Torreon (Figure 5.15l and Figure 5.16l) had shown a remarkable difference. Unfortunately, some training subsets experienced troubles during the training process, therefore, the hyperparameters such as dropout or LSTM units were modified in some evaluations such as: Torreon, La Paz, B.C., Queretaro, Cd. Juarez, and Pto. Cabezas. This was necessary to avoid under-fitting and over-fitting on predicted subsets.

Figure 5.17 and Figure 5.18 indicate the R^2 values of both training and validation subsets respectively, where Experiment 2 predicted the outcomes slightly better than Experiment 1. R^2 indicated how well the regression predictions approximated the real data points.

According to results from Experiment 2, Figure 5.19 shows the validation metrics for each evaluated rain-attenuation. Experiment 2 was chosen because the overall model performance obtained from it was better than Experiment 1. It was possible to note that in some cases because of the many outliers, the predicted values did not fit well on the regression line. For instance, in a few cases such as La Paz, B.C.

(a) Panama, range: $k = 19110, \ldots, 19160$

(b) San Jose, range: $k = 25540, \ldots, 25590$

(c) Tegucigalpa, range: $k = 14075, \ldots, 14125$

(d) Mexico City, range: $k = 10520, \ldots, 10570$

(e) Monterrey, range: $k = 26090, \ldots, 26140$

(f) Guadalajara, range: $k = 13100, \ldots, 13150$

(g) Tijuana, range: $k = 259980, \ldots, 260030$

(h) La Habana, range: $k = 26170, \ldots, 26220$

(i) Sto. Domingo, range: $k = 50465, \ldots, 50515$

(j) San Salvador, range: $k = 32255, \ldots, 32305$

(k) San Juan, range: $k = 18050, \ldots, 18100$

(l) Torreon, range: $k = 41965, \ldots, 42015$, dropout=0.5

Figure 5.15: The training rain-attenuation subsets obtained from deep learning models.

(m) La Paz, B.C., range: $k = 52215, \ldots, 52265$, dropout= 0.5

(n) Veracruz, range: $k = 14183, \ldots, 14233$

(o) Cancun, range: $k = 37100, \ldots, 37150$, dropout= 0.5

(p) Queretaro, range: $k = 15215, \ldots, 15265$, dropout= 0.5

(q) Tuxtla, Gtz., range: $k = 38320, \ldots, 38370$

(r) Cd. Juarez, range: $k = 74145, \ldots, 74195$, $\mathcal{L}_{U1} = 400$, dropout=0.5

(s) San Pedro Sula, range: $k = 10000, \ldots, 10050$

(t) Belmopan, range: $k = 12165, \ldots, 12215$

(u) Kingston, range: $k = 17350, \ldots, 17400$

(v) Merida, range: $k = 27598, \ldots, 27648$, dropout= 0.3

(w) Pto. Cabezas, range: $k = 19180, \ldots, 19230$, dropout= 0.5

(x) Oaxaca, range: $k = 11680, \ldots, 11730$

Figure 5.15: The training rain-attenuation subsets obtained from deep learning models (cont.).

(a) Panama, range: $k = 475460, \ldots, 475510$

(b) San Jose, range: $k = 477390, \ldots, 477440$

(c) Tegucigalpa, range: $k = 482140, \ldots, 482190$

(d) Mexico City, range: $k = 477490, \ldots, 477540$

(e) Monterrey, range: $k = 474550, \ldots, 474600$

(f) Guadalajara, range: $k = 479480, \ldots, 479530$

(g) Tijuana, range: $k = 510090, \ldots, 510140$

(h) La Habana, range: $k = 505318, \ldots, 505368$

(i) Sto. Domingo, range: $k = 504330, \ldots, 504380$

(j) San Salvador, range: $k = 503138, \ldots, 503188$

(k) San Juan, range: $k = 519440, \ldots, 519490$

(l) Torreon, range: $k = 496275, \ldots, 496325$, dropout=0.5

Figure 5.16: The validation rain-attenuation subsets obtained from deep learning models.

(m) La Paz, B.C., range: $k = 518740, \ldots, 518790$, dropout= 0.5
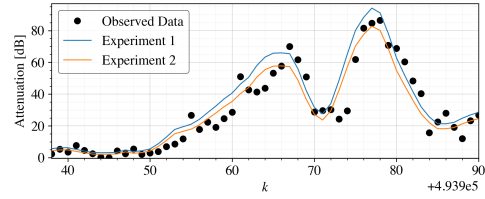
(n) Veracruz, range: $k = 493940, \ldots, 493990$
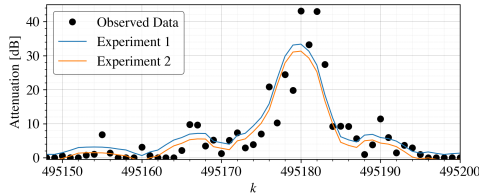
(o) Cancun, range: $k = 495150, \ldots, 495200$, dropout= 0.5
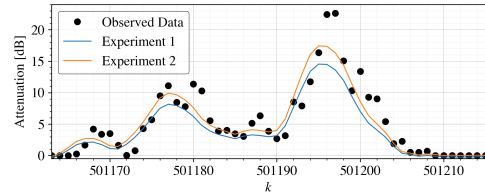
(p) Queretaro, range: $k = 501165, \ldots, 501215$, dropout= 0.5
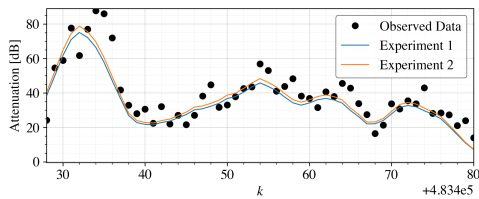
(q) Tuxtla, Gtz., range: $k = 483430, \ldots, 483480$
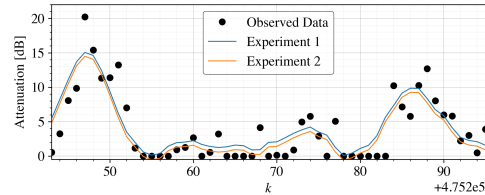
(r) Cd. Juarez, range: $k = 475245, \ldots, 475295$, $\mathcal{L}_{U1} = 400$, dropout=0.5
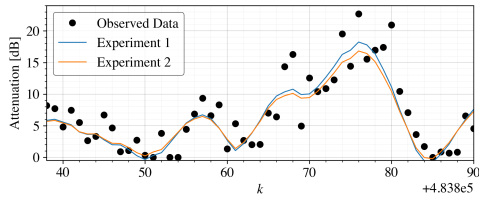
(s) San Pedro Sula, range: $k = 483840, \ldots, 483890$
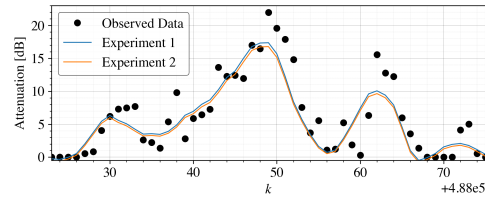
(t) Belmopan, range: $k = 488025, \ldots, 488075$
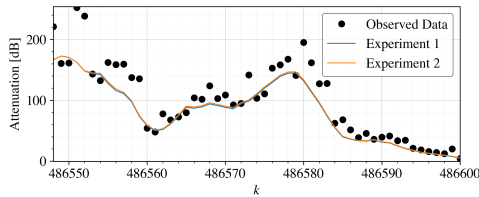
(u) Kingston, range: $k = 486550, \ldots, 486600$
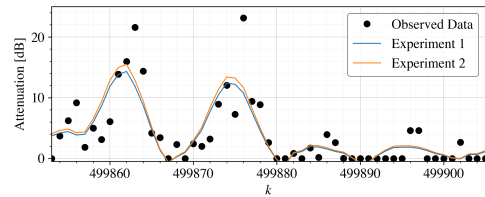
(v) Merida, range: $k = 499855, \ldots, 499905$, dropout= 0.3
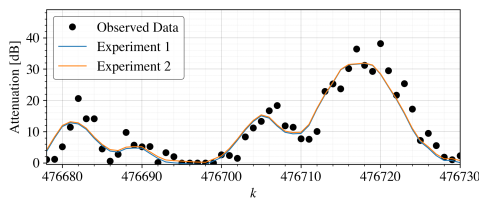
(w) Pto. Cabezas, range: $k = 476680, \ldots, 476730$, dropout= 0.5
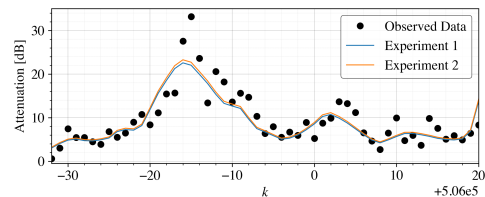
(x) Oaxaca, range: $k = 505970, \ldots, 506020$

Figure 5.16: The validation rain-attenuation subsets obtained from deep learning models (cont.).
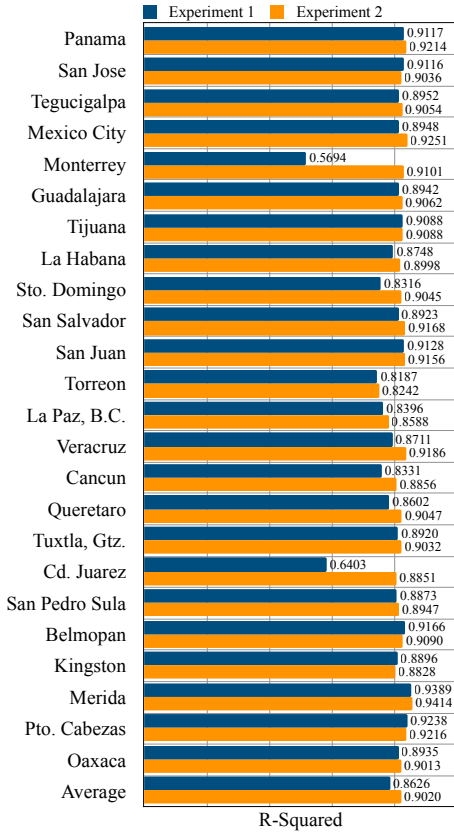
Figure 5.17: R^2 for training subsets.
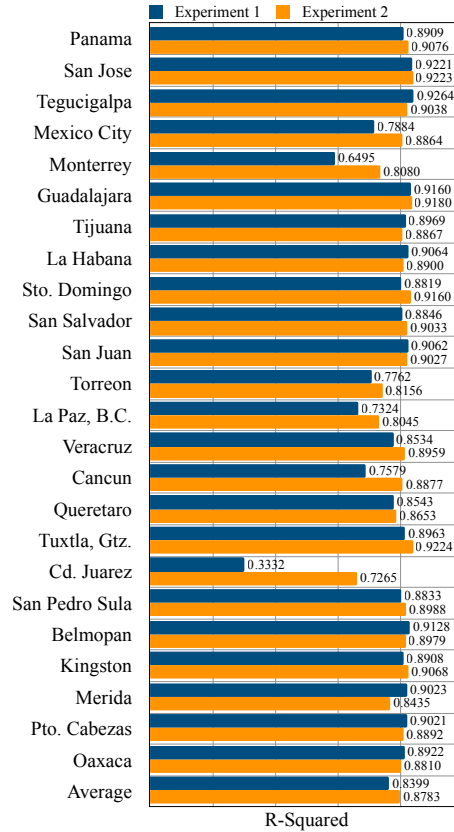
Figure 5.18: R^2 for validation subsets.

(Figure 5.19m), or Cd. Juarez (Figure 5.19r), the squared residuals with respect to the linear regression were higher than the best models such as Tuxtla, Gtz. (Figure 5.19q), or San Jose (Figure 5.19b).

By using Eq. (5.34) and Eq. (5.35), it was possible to predict the CNIR for the next time step, $t + 1$. For this purpose, the co-channel interference value, $\zeta_{co} = 36.09$ dB, and the adjacent interference value, $\zeta_{adj} = 38.17$ dB, were obtained from subsection 4.5.3. Figure 5.20 depicts the model with higher R-Squared, $R^2 = 0.9224$, which demonstrates that the rain attenuation, Figure 5.20a, directly influences on the CNIR, Figure 5.20b, and spectral efficiency, Figure 5.20c. On the other hand, Figure 5.21 indicates the model with lower R-Squared, $R^2 = 0.7265$. In both cases, only 50 samples were employed to visualize properly the effects of rain attenuation. Also, the spectral efficiency was determined from CNIR values by the DVB-S2X table [6].

These two approaches can be also analyzed from a climatological perspective to compare with the obtained prediction models. For instance, Tuxtla, Gtz. is located in the rainforest area of Mexico regarding the Köppen-Geiger climate type map [91]. On the other hand, Cd. Juarez is located in the cold desert zone of Mexico according to the Köppen-Geiger climate type map of North America [91]. This makes sense, as the mean annual precipitation at Tuxtla, Gtz. is about 1900 mm, whereas at Cd. Juarez is less than 200 mm [92]. For this reason, the Tuxtla prediction model was not difficult to train because there were more precipitation data than at Cd. Juarez. That
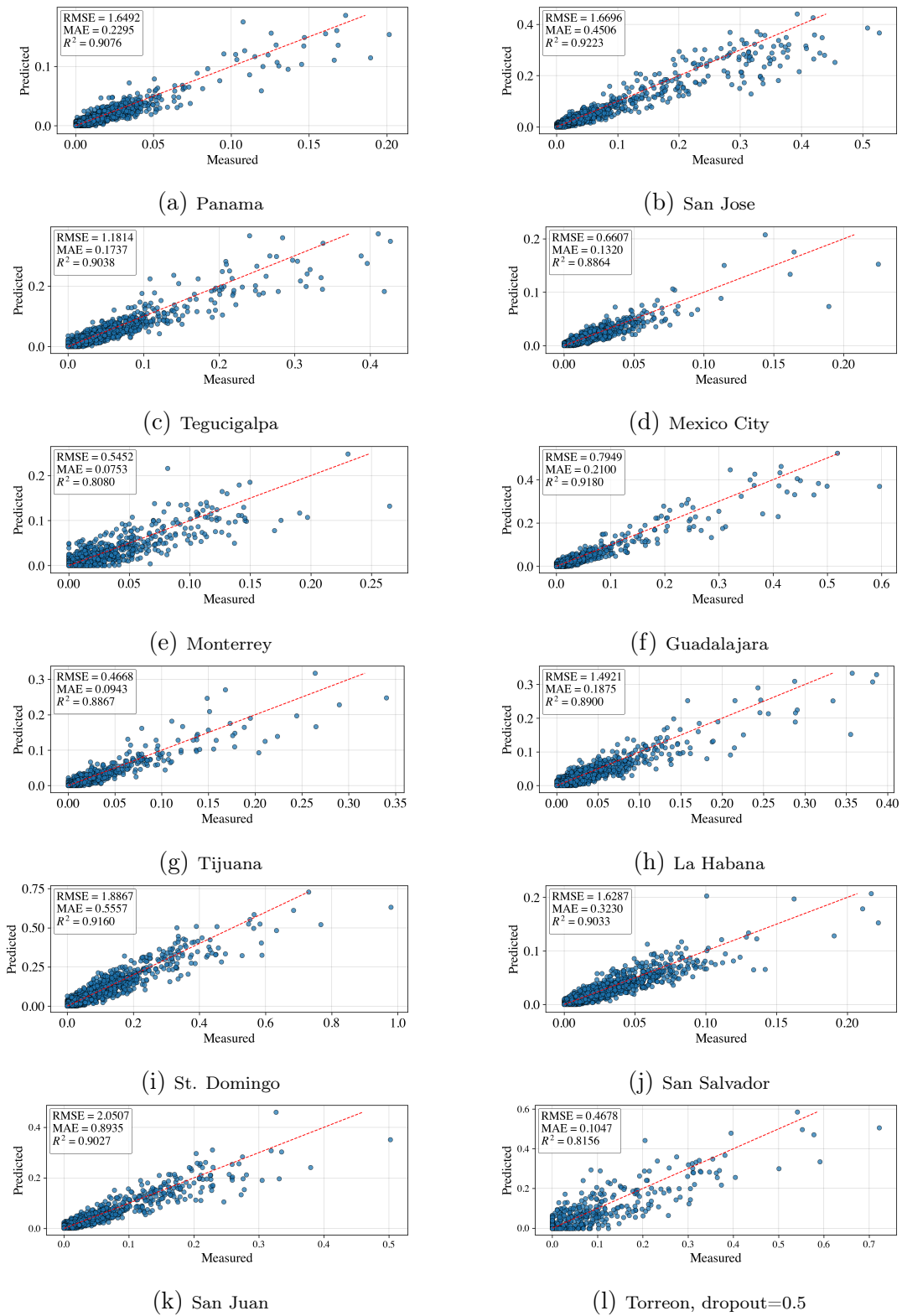
(a) Panama

(b) San Jose

(c) Tegucigalpa

(d) Mexico City

(e) Monterrey

(f) Guadalajara

(g) Tijuana

(h) La Habana

(i) St. Domingo

(j) San Salvador

(k) San Juan

(l) Torreon, dropout=0.5

Figure 5.19: Model performance results: measured vs. predicted rain-attenuation values for validation.

(m) La Paz, dropout= 0.5

(n) Veracruz

(o) Cancun, dropout= 0.5

(p) Queretaro, dropout= 0.5

(q) Tuxtla, Gtz.

(r) Cd. Juarez, $\mathcal{L}_{U1} = 400$, dropout=0.5

(s) San Pedro Sula

(t) Belmopan

(u) Kingston

(v) Merida, dropout= 0.3

(w) Pto. Cabezas, dropout= 0.5

(x) Oaxaca
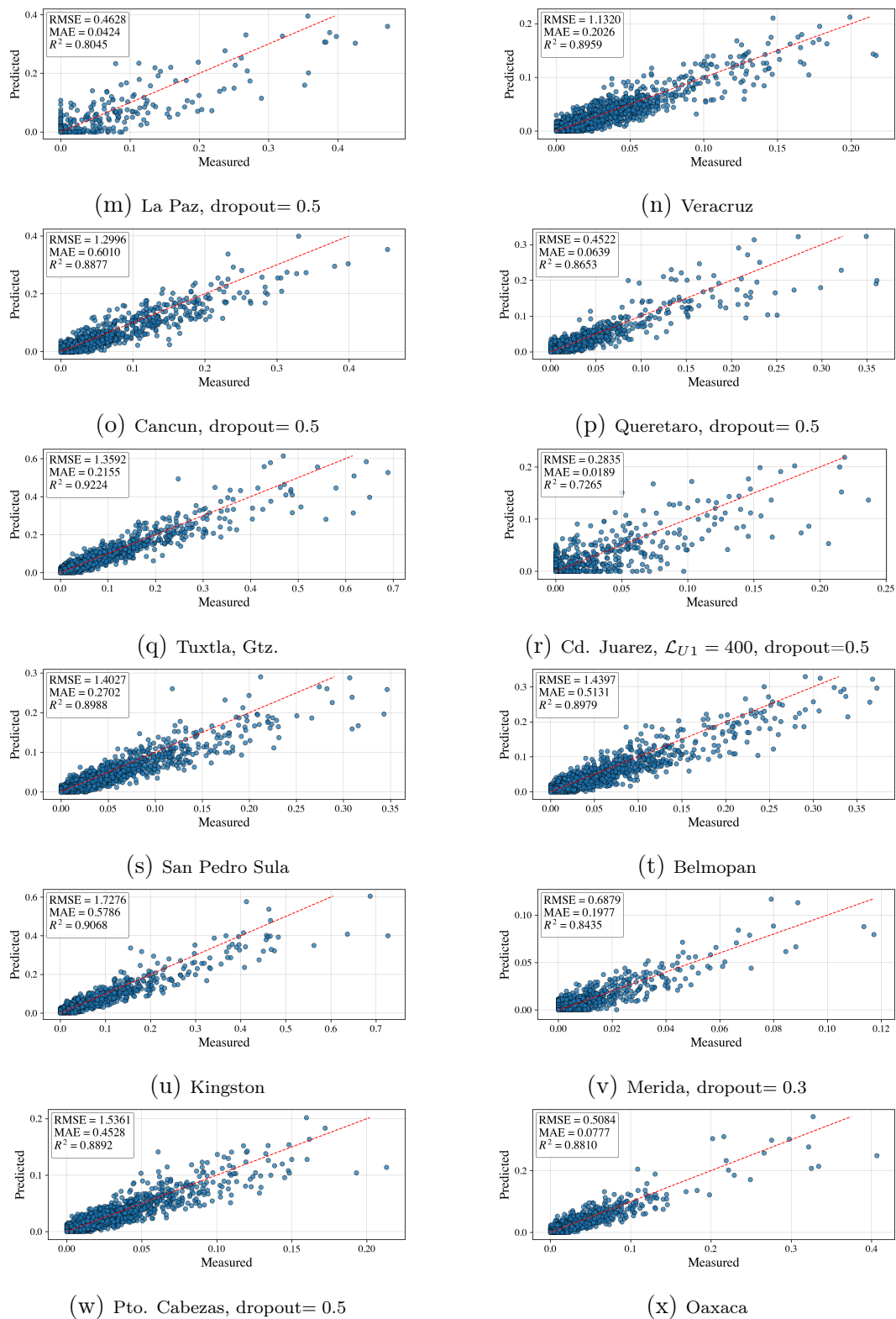
Figure 5.19: Model performance results: measured vs. predicted rain-attenuation values for validation (cont.).
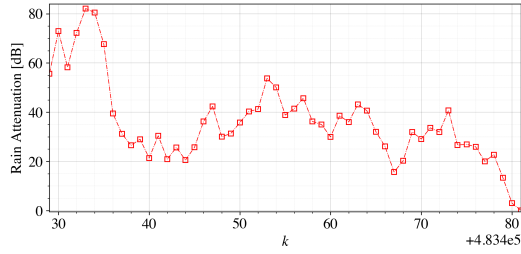
(a) Rain attenuation window
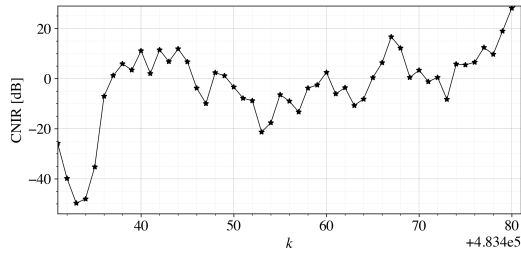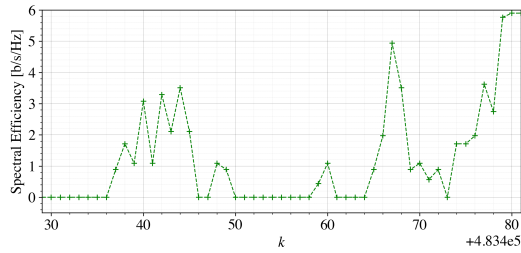
(b) CNIR window

(c) Spectral efficiency window

Figure 5.20: The higher R-Squared, $R^2 = 0.9224$ at Tuxtla, Gtz.
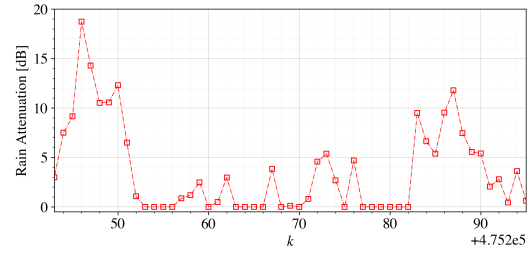
(a) Rain attenuation window
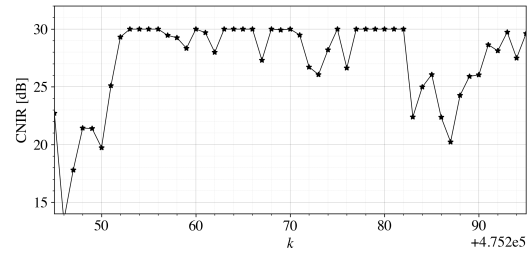
(b) CNIR window
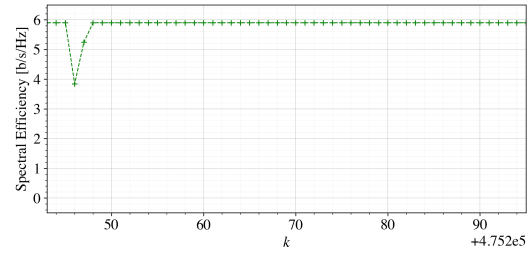
(c) Spectral efficiency window

Figure 5.21: The lower R-Squared, $R^2 = 0.7265$ at Cd. Juarez.

is, the lack of data is a big problem because it can be difficult to train and validate the model, obtaining low accuracy, in addition to not finding reasonable results. Finally, Figure 5.22 indicates the performance of the deep learning network configuration by showing both training and validation loss functions for each rain-attenuation time series. Both loss function graphics were the results of Experiment 2.

5.5   Discussions

The outcomes of Experiment 2 were better than Experiment 1, improving scores of metrics such as RMSE and MSE. Therefore, the trained and validated model obtained from Experiment 2 was the basis for understanding and forecasting accurately the rain-attenuation and their strong influence on feeder links. However, the most important metric was the coefficient of determination or R^2, which was decisive in order to pick out the best Experiment in this study. R^2 is a number between 0 and 1 that estimates the changes in the dependent variable by changes in the independent
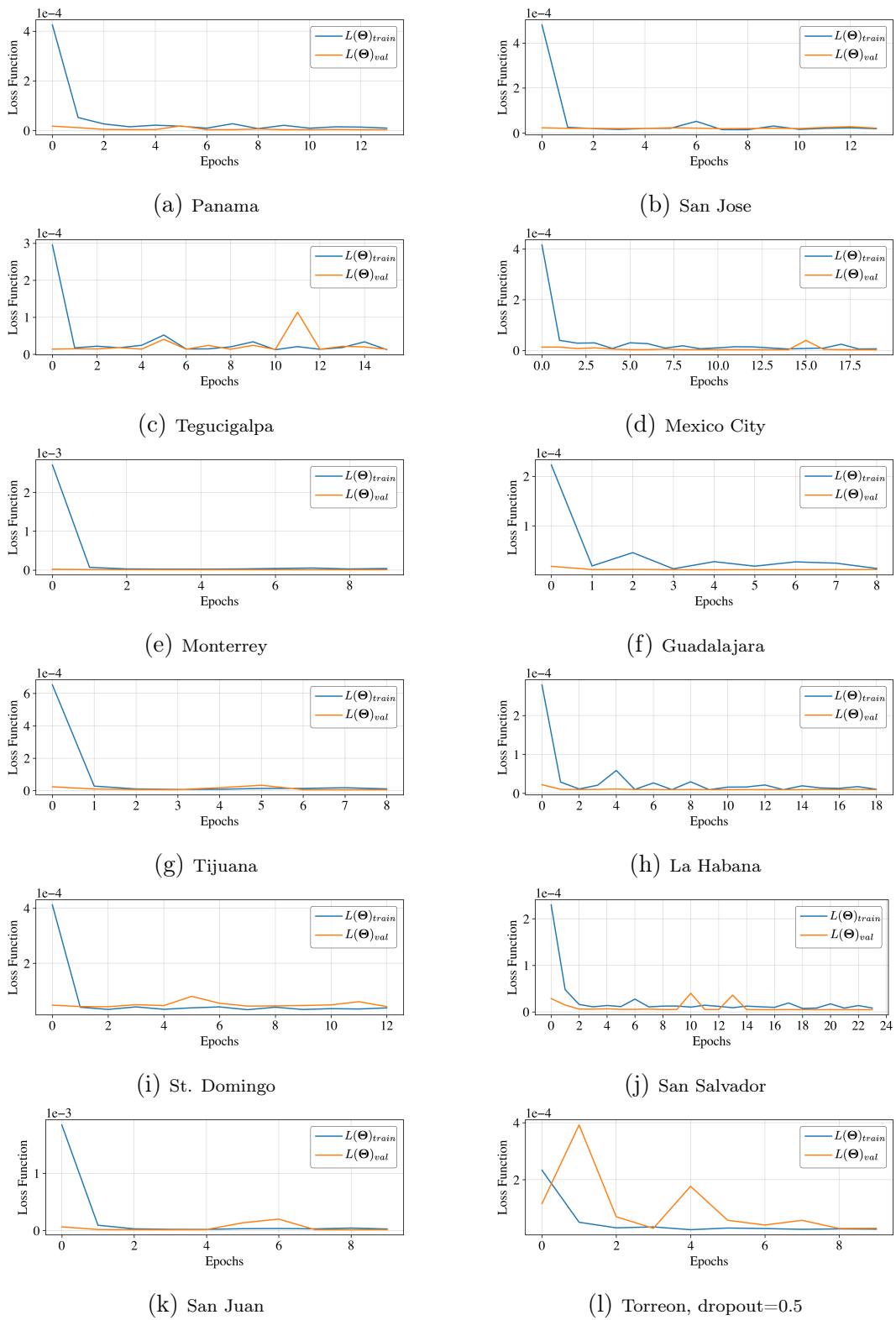
(a) Panama

(b) San Jose

(c) Tegucigalpa

(d) Mexico City

(e) Monterrey

(f) Guadalajara

(g) Tijuana

(h) La Habana

(i) St. Domingo

(j) San Salvador

(k) San Juan

(l) Torreon, dropout=0.5

Figure 5.22: Training and validation loss functions for each rain-attenuation time series.

(m) La Paz, dropout= 0.5

(n) Veracruz

(o) Cancun, dropout= 0.5

(p) Queretaro, dropout= 0.5

(q) Tuxtla, Gtz.

(r) Cd. Juarez, $\mathcal{L}_{U1} = 400$, dropout=0.5

(s) San Pedro Sula

(t) Belmopan

(u) Kingston

(v) Merida, dropout= 0.3

(w) Pto. Cabezas, dropout= 0.5

(x) Oaxaca
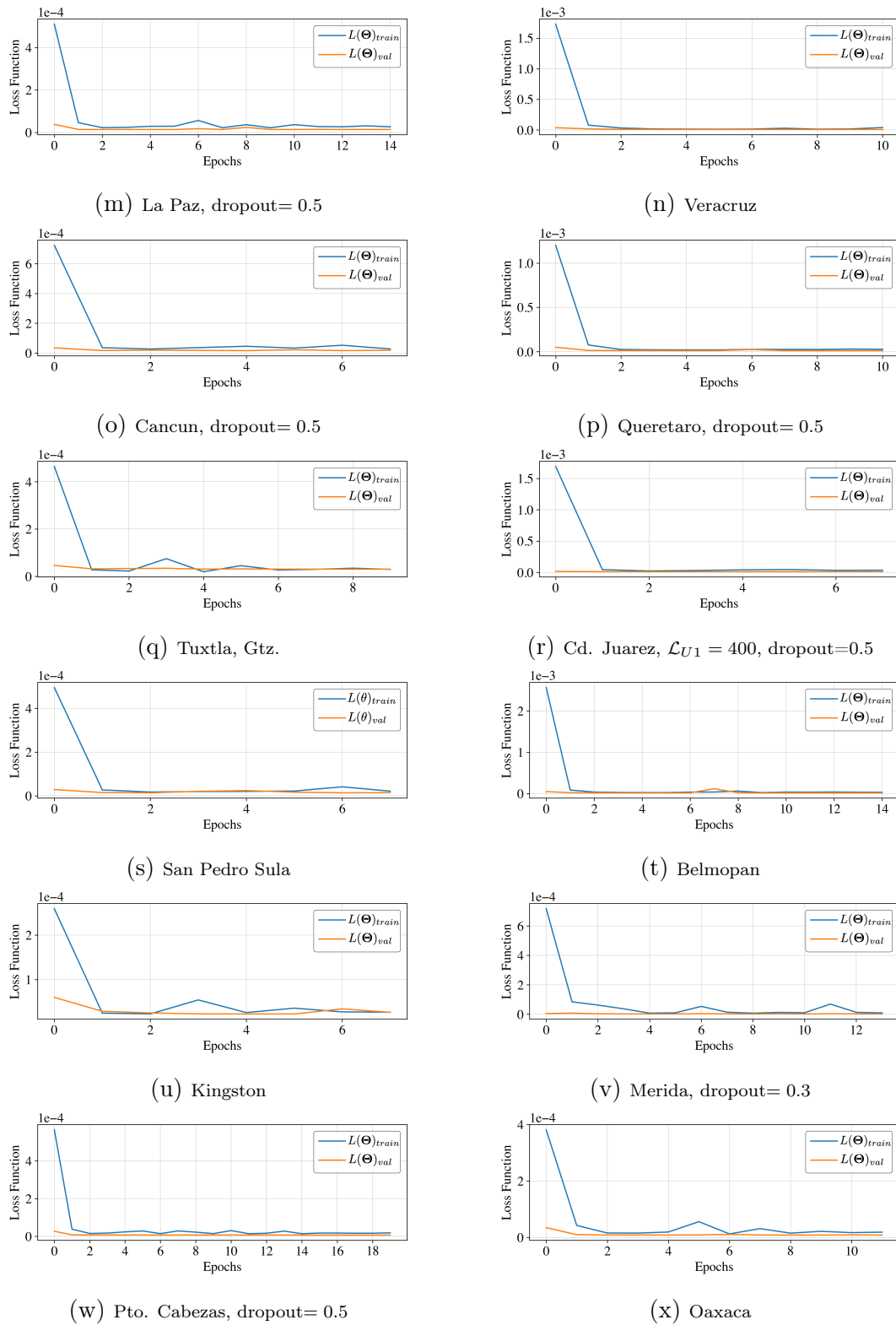
Figure 5.22: Training and validation loss functions for each rain-attenuation time series (cont.).

variable. In fact, a high R^2, close to 1, is necessary for precise predictions, therefore, the found R^2 from validation subsets were between 0.7265 and 0.9224. Potentially, these values demonstrate a high accuracy of deep learning networks obtained from Experiment 2 unlike deep learning networks from Experiment 1, as seen in Figure 5.18.

In order to understand graphically R^2, data points of deep learning networks with high R^2 are lying near to the regression line, whereas data points of deep learning networks with low R^2 are dispersed, as demonstrated in Figure 5.19. After all, determining an adequate R^2 is a matter of judgment. Hence, the found R^2s accomplish the requirements for all rain-attenuation models.

In this sense, the predictive model of rain attenuation with high R^2, Figure 5.20, is compared with the predictive model with low R^2, Figure 5.21. For instance, the first model predicted an aggressive rain-attenuation in the range from $k = 483430$–483480. In this case, CNIR predictions varied from -50.0–30.0 dB, approximately, impacting strongly on the spectral efficiency. On the contrary, a non-aggressive rain-attenuation was predicted by the second model in the range from $k = 475245$–475295. In this case, CNIR predictions are more stable due to the lower attenuation of the rain, therefore, the spectral efficiency is almost constant in that range, as seen in Figure 5.21c.

It is important to mention that the upper limit of the DVB-S2X standard, in power terms, is 19.57 dB, which corresponds to the best modulation and codification, 256 APSK 3/4, and spectral efficiency of 5.9009 b/s/Hz [6]. That is, the CNIR has a margin of about 10.00 dB until the signal is degraded by rain attenuation. In other words, the spectral efficiency varies according to the CNIR level, as shown in Figure 5.20b and Figure 5.20c. In this case, the rain attenuation greater than 10.00 dB affects strongly the CNIR level, degrading the spectral efficiency until there is no signal, i.e., if the CNIR < -2.85 dB, then spectral efficiency $= 0.00$ b/s/Hz.

Furthermore, it was figured out that the validation loss, $L(\mathbf{\Theta})_{val}$, is lower than training loss, $L(\mathbf{\Theta})_{train}$, during the training and validation processes of the proposed models, as shown in Figure 5.22. Nonetheless, this is not fundamentally an uncertain phenomenon in essence. Indeed, the structure of both training and validation subsets can have a smaller validation loss than the training loss. This usually happens for five main reasons,

- When the training data is harder to train or learn patterns on it, whereas it is possible to have an easier validation subset.

- Dropout is not enabled during the validation process, therefore, this can lead to greater outcomes on the validation subset.

- By default, regularization is solely applied during the training process but not during the validation or testing process. Nevertheless, when the regularization is present during the validation process, then both loss functions can be more similar.

- On average, the training loss is performed during each epoch whereas the validation loss is performed after each epoch. That is, the training loss can be out of phase a half epoch regarding the validation loss.
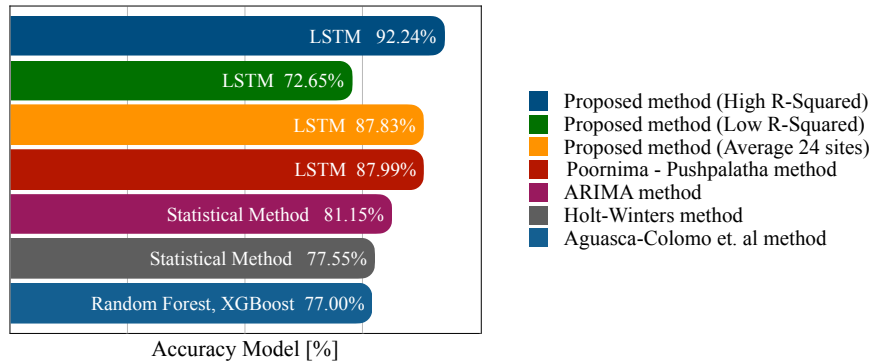
Figure 5.23: Comparison between predictive models.

- It is possible that in the early phase of the training process the validation loss is smaller than the training loss.

In this thesis, dropout and regularization methods were added to the LSTM networks, there were even some different configurations to train hard LSTM networks, for instance, Torreon (dropout = 0.5), La Paz, B.C. (dropout= 0.5), Cancun (dropout = 0.5), Queretaro (dropout = 0.5), Cd. Juarez ($\mathcal{L}_{U1}$ = 400 units and dropout = 0.5), Merida (dropout = 0.3), and Pto. Cabezas (dropout = 0.5). Thus, the first reason is essentially the main factor to diminish the validation loss in contrast to the training loss. Hence, data are prepared carefully, as the outcomes depend significantly on the quality of data, i.e, pre-processing data, cleaning data, and partitioning training/validation subsets.

Finally, Figure 5.23 illustrates the comparison between predictive models/methods according to the accuracy metric. For instance, the best model found in this thesis, Experiment 2: 90/10, has better accuracy than the Poornima-Pushpalatha method [93], i.e., 92.24% vs. 87.99%. However, on average, the proposed method is slightly lower than the Poornima-Pushpalatha method, 87.83% vs. 87.99%. It is important to mention that the proposed method in this thesis evaluated 24 locations whereas the Poornima-Pushpalatha method evaluated a single location at Hyderabad, India. Other proposals employed statistical methodologies, such as the autoregressive integrated moving average (ARIMA) method, 81.15% of accuracy, [94], and Holt-Winters method, 77.55% of accuracy, [95], but they could not overcome the accuracy of the proposed LSTM method. At last but not least, the Aguasca-Colomo et. al method proposed a random forest model based on classification with an accuracy of 77.00% [96]. As a result, Machine Learning methods based on regression techniques have better performance and accuracy than statistical methods in order to predict rain events.

To sum up, this proposal guarantees an accurate rain-attenuation prediction at the evaluated sites, generalizing efficiently the models. Therefore, this method can efficiently contribute to managing the resources of both the space segment and the ground segment of a high throughput satellite system.

5.6 Contributions of the Research

The proposed method and found results in this chapter were submitted to Neural Processing Letters journal to be reviewed and published later. Also, in this context, an initial study based on neural networks was presented in a specialized conference: *"XXXIII Simposium Nacional de la Unión Científica Internacional de Radio, URSI 2018,"* at Granada, Spain.

- Andres Cornejo, Salvador Landeros-Ayala, Ramon Martinez Rodriguez-Osorio, and Jose Maria Matias. Optimization of the Ground Segment for an UHTS System through Neural Networks. *In XXXIII Simp. Nac. la Unión Científica Int. Radio (URSI 2018)*, pages 1–5, Granada, Spain, 2018

Chapter 6

Ground Segment Optimization by Using Smart Strategies of Switching Between Gateway Stations

6.1 Introduction

The ground segment (GS) is an important part of satellite communications, which contains the gateways stations (GW) and user terminals (UT-VSAT) necessary to communicate to/from the high throughput satellite HTS. When a user requires the satellite service, then the operator adds a VSAT to the network, as long as there is availability. Meanwhile, the number of nominal gateways NGWs depends on the satellite capacity, i.e., each NGW manages a portion of the total capacity, as can be seen in Section 3.4. In this context, it is simple to determine the number of GWs, but it does not consider when the rain affects the feeder links. That is, if the rain impairs one or more GWs, the satellite capacity diminishes, impacting directly on the quality of service (QoS) and leaving several VSATs out-of-service.

In a sense, by using the Adaptive Coding and Modulation (ACM) from the DVB-S2X standard, the system availability might not drop dramatically [6]. Also, the Uplink Power Control (ULPC) can manage a few dBs to compensate for channel degradation [74–76]. Despite the fact that both techniques can mitigate channel degradation, they can not combat the aggressive effects of the heavy rain over feeder links.

For this reason, some researchers recommend that the NGWs must be separated by a distance D to avoid the correlated rain to each other, i.e. so that the rain affects only one NGW at a time. Each NGW has an extra resource to support when an affected feeder link is in an outage due to the heavy rain. This technique is known as Smart Gateway Diversity (SGD), where the affected NGW is capable of re-routing traffic to an alternate NGW with extra resources for temporary allocation, improving the availability considerably [26, 28].

Other researchers have proposed to add redundant gateway stations as a backup (PGWs), i.e., when the rain attenuation impacts on NGW's feeder link, an available

PGW gets into the network rather than the affected NGW. Temporarily, the PGW manages all traffic of the affected NGW and establishes a link between the satellite and PGW, waiting for the NGW is available again. This configuration is also known as the $\bar{N} + \bar{P}$ scheme, whose NGWs are denoted by $\bar{N}$, and PGWs are described by $\bar{P}$ [22, 23, 26, 97].

However, this scheme could be an inelegant solution and very little efficient without evaluating the adequate number of PGWs necessary for keeping up the system availability. Here, some researchers have simplified the analysis by proposing a $1 + 1$ scheme and using stationary distributions or Markov Chains to calculate the number of PGWs properly [21, 25, 98, 99]. Naturally, this leads to a better switching strategy between NGWs and PGWs but without achieving an adequate optimization of the ground segment. Other authors have developed interesting methods in order to optimize the ground segment in a particular way [100, 101].

Despite the smart gateway diversity is focused on increasing the system availability and improving the switching strategies, it is not based on reducing the number of PGWs optimally. For this purpose, a predictive method, as proposed in Chapter 5, provides predictions of rain attenuation by time intervals, identifying how many times the NGWs could be with a link outage due to the rain and which PGWs could temporarily replace to each one of them. Compared with other methods, this predictive method aids to a large degree to optimize the number of PGWs. This contribution must guarantee an availability higher than 99.9%, foreseeing accurately when a feeder link is going to be affected by the rain. Also, this method contributes to the switching strategy to be of lower complexity than previous methods.

6.2   Proposed Model

To begin with, the ITU-R 1815 recommended that the distance between two GWs must be $\geq$ 80 km to avoid the correlated rain, dropping the spatial correlation coefficient ρ_a to < 0.1, as can be seen in Section2.3. By using the coordinates of Appendix A.2, it was possible to determine the distance matrix, $\mathbf{D}$, between the GW locations. Furthermore, GW locations were the same as those employed by analysis of Chapter 5. Appendix A.3 presents the distance matrix between pairs of locations. In all cases, the distances were greater than 80 km between each other, ensuring the uncorrelated rain for all locations.

6.2.1   Sizing of Nominal Gateways, NGWs

In the high throughput satellite (HTS) systems, the total capacity is strongly related to the number of nominal gateways (NGW) on the ground segment (GS). Initially, the data traffic is symmetrically assumed between forward and return links. That is, 50% of the inbound's throughput and 50% in the outbound, [1 : 1]. In this context, the upload speed is not strained by the symmetrical connection, whose data is flowed in a proper way [18].

Each NGW manages its feeder link where the feeder uplink is the focus of this

study. For this case, the feeder uplink does not use the frequency reuse, although it uses double polarization. Based on Eq. (3.1) and Eq. (3.2), the capacity, in b/s, of each feeder uplink is expressed as

$$Cp_i = \frac{N_p \cdot S_{avail}}{N_{sb}} S_{eff_i}, \text{for } i = 1, 2, \dots, \bar{N},$$

(6.1)

where N_p is the number of polarizations, N_{sb} is the number of frequency sub-bands, S_{avail} is the available spectrum, and S_{eff} is the spectral efficiency from the DVB-S2X standard by each feeder uplink [6,18], as was discussed in Chapter 3. At this point, the inbound uplink beams are received and demodulated by the satellite communication subsystem. Naturally, each NGW transmits its corresponding feeder uplink beam. Thus, the total capacity is directly related to the number of NGWs on the GS, which is denoted by

$$Cp_T = \sum_{i=1}^{\bar{N}} Cp_i$$

(6.2)

In this study, the inbound Cp_T is computed by four configurations of NGWs, where $\bar{N} = 4, 8, 12$, and 16.

6.2.2   Smart Method for Forecasting Rain Attenuation and CNIR at each GW

This novel method is based on Machine Learning algorithms by the implementation of LSTM networks. To begin with, the rain attenuation time-series for each possible GW location was obtained by ITU Recommendation, ITU-R 1853 [38]. Thus, each rain attenuation time-series was trained and validated by LSTM networks, as can be seen in Chapter 5 in detail. As a result, each predicted rain attenuation time-series, at time step $t + 1$, can be denoted by $\hat{\mathbf{A}}_{t+1,i} = \mathcal{F}(\mathbf{A}_{t,i}^{(m)})$ for $i = 1, 2, \dots, N$, where $\mathcal{F}$ is the deep learning model, m is the number of examples of the rain attenuation time-series by each GW-site. Figure 5.10 illustrates the block diagram of the smart method employed to predict rain attenuation time-series in this proposal.

Finally, each prediction of rain attenuation time-series can be stored in matrix $\hat{\mathbf{A}} \in \mathbb{R}^{K \times N}$. Using Eq. (5.34) and Eq. (5.35), it was possible to compute the predicted CNIR, $\hat{\mathbf{\Xi}} \in \mathbb{R}^{K \times N}$, at time step $t + 1$. Both matrices can be processed and employed by NCC to supervise and monitor the status of each feeder uplink in advance.

6.2.3   Method to Decide the Best NGWs

In order to evaluate the status of each feeder uplink, a CNIR threshold, ξ_{th}, leads to understanding how well the feeder uplink signal works between the NGW and satellite, i.e., when the CNIR above the threshold, in addition to knowing if the rain affects each feeder uplink, i.e., when the CNIR below the threshold. However, an adequate CNIR threshold could result in a challenge in this study. For this purpose,

the predicted CNIR matrix, $\hat{\Xi}$, is evaluated by the CNIR threshold. By each GW-site, it is important to mention that each CNIR prediction is implicit in each column i of the matrix. Therefore, if $\hat{\Xi}_{t+1,i} \geq \xi_{th}$ for $i = 1, 2, \ldots, N$, and $t = 1, 2, \ldots, K$, then the feeder uplink is active at that time step, otherwise, the feeder uplink is inactive. Based on the previous statement, it is possible to find the availability of each feeder uplink, which is denoted by

$$\nu_i = \frac{1}{K} \sum_{k=1}^{K} \left[(\hat{\Xi}_{k,i} \geq \xi_{th} \to x = 1) \wedge (\hat{\Xi}_{k,i} < \xi_{th} \to x = 0) \right], \text{for } i = 1, 2, \ldots, N, \quad (6.3)$$

where x is a temporary variable. As a result, GWs can be sorted from the highest to the lowest according to individual availability, ν_i. Thus, each i column of the matrix $\hat{\Xi} \in \mathbb{R}^{K \times N}$ is also sorted by individual availability, ν_i. This method allows us to define the best candidates in order to set up the ground network system with NGWs. Therefore, it is essential to find system availability regarding its network configuration. In this context, the system availability, [102], is given by

$$\nu = \nu_1 \cdot \nu_2 \cdot, \ldots, \cdot \nu_{\bar{N}} = \prod_{i=1}^{\bar{N}} \nu_i, \quad (6.4)$$

where $\bar{N}$ corresponds to the number of NGWs, comprising the ground network configuration. However, it is highly probable that the system availability is lower than 99.9%, dropping even more when increasing the number of NGWs. Indeed, the ITU Recommendation, ITU-R S.1557, indicates that for gateway stations at geographically dispersed hubs must require the end-to-end system availability of at least 99.9% [16]. For this reason, it is necessary to add redundancy to the ground network, increasing the system availability equal to or greater than 99.9%.

6.2.4   A Strategy to Allocate the Best PGWs

It is necessary to mention that the sorted matrix $\hat{\Xi}$ contains the possible NGWs and PGWs for this study. The first $\bar{N}$ columns correspond to the number of NGWs of the ground network, whereas the next columns correspond to the number of possible PGWs to be added to the ground network by this strategy. Therefore, in general terms, the columns for redundant gateways are denoted by $\hat{\Xi}_{t+1,\bar{N}+j}$, for $j = 1, 2, \ldots, \bar{P}$, where $\bar{P}$ is the number of PGWs.

To be precise, this procedure consists of adding a redundant gateway, PGW, when an NGW feeder uplink is an outage due to the rain. For this purpose, a switching strategy is implemented between NGW and PGW by a straightforward mechanism. That is, when an NGW is going to experience an outage in its feeder uplink at time step $t + 1$, i.e., $\hat{\Xi}_{t+1,i} < \xi_{th}$, for $i = 1, 2, \ldots, \bar{N}$, then the affected NGW will commute all its data traffic to an available PGW. Also, this mechanism is able to verify if the assigned PGW feeder uplink is active, i.e., $\hat{\Xi}_{t+1,\bar{N}+1} \geq \xi_{th}$. Otherwise, the mechanism goes to the next candidate, as long as $\hat{\Xi}_{t+1,\bar{N}+2} \geq \xi_{th}$, and so on

until reaching the condition. However, the picked PGW could still be working with another affected NGW. Therefore, the mechanism is also capable of looking for the next PGW candidate. When the initial NGW is active again, then the mechanism commutes all data traffic from the current PGW towards the initial NGW. To sum up, this switching mechanism can be called the $1 + \bar{P}$ configuration, where each NGW is backed up by redundant gateways $\bar{P}$ to increase the feeder uplink availability. Figure 6.1 depicts the flowchart of the $1 + \bar{P}$ switching strategy for each NGW that explains the described process in this proposal in detail. In other words, the multiple $1 + \bar{P}$ mechanism, running $\bar{N}$ times, provides a scheme $\bar{N} + \bar{P}$ as a result.

The number of feeder uplink outages can be individually accounted for by the expression $(1 - \nu_i) \cdot K$, for $i = 1, 2, \ldots, \bar{N}$, where K is the total number of samples at a time period. Based on the above formulation, the total number of feeder uplink outages in the system is given by

$$\text{outages} = K \cdot \sum_{i=1}^{\bar{N}} (1 - \nu_i) \tag{6.5}$$

In order to decrease the network complexity, the system unavailability only with NGWs must be equal or lower than 5% in a year, i.e. $(1 - \nu) \cdot 100 \leq 5\%$, reducing the number of switchings between NGWs and PGWs. As a result, the value of the CNIR threshold, ξ_{th}, is set up based on the system's unavailability percentage. Finally, used the $1 + \bar{P}$ strategy, the feeder-uplink availability expression can be denoted by

$$\nu_{B_i} = \frac{1}{K} \sum_{k=1}^{K} \Big\{ (\hat{\bar{\Xi}}_{k,i} \geq \xi_{th} \rightarrow x = 1) \wedge$$
$$\wedge \big[(\hat{\bar{\Xi}}_{k,\bar{N}+1} \geq \xi_{th} \rightarrow x = 1) \wedge (\hat{\bar{\Xi}}_{k,\bar{N}+2} \geq \xi_{th} \rightarrow x = 1) \wedge \ldots$$
$$\wedge (\hat{\bar{\Xi}}_{k,\bar{N}+\bar{P}} \geq \xi_{th} \rightarrow x = 1) \wedge (\hat{\bar{\Xi}}_{k,\bar{N}+\bar{P}} < \xi_{th} \rightarrow x = 0) \big] \Big\}, \text{for } i = 1, 2, \ldots, \bar{N} \tag{6.6}$$

Indeed, this expression determines how many redundant PGW gateways, denoted by $\bar{P}$, can provide instant support to an affected NGW at an annual period, improving the feeder uplink availability as much as possible. Finally, the total system availability is computed by the Eq. (6.4), so that $\nu_B = \nu_{B_1} \cdot \nu_{B_2} \cdot \ldots \cdot \nu_{B_{\bar{N}}}$. Naturally, this leads to determine the necessary number of $\bar{P}$ to aid in the ground network to maintain it above 99.9%, finding an optimized $\bar{N} + \bar{P}$ scheme.

6.3 The $1 + \bar{P}$ Scheme Analyzed by a Markov Chain

The $1 + \bar{P}$ scheme was also analyzed using a stationary distribution by a Markov Chain. Therefore, it was necessary to find the probability of rain for each GW location. For this purpose, the ITU Recommendation ITU-R P. 837 models the characteristics of precipitation for propagation, whose aim is to calculate the rainfall rate exceeded for the desired average annual probability of exceedance and a given location of the Earth [29].

```
                    ┌─────────────────┐
                    │  Start (k, i = 1) │
                    └─────────────────┘
                             │
                    ┌─────────────────┐
                    │ Collect all CNIRs │
                    │  Ξ̂ ∈ ℝ^{K×N}      │
                    └─────────────────┘
                             │
                    ┌─────────────────┐
                    │ Sort Ξ̂ according to ν │
                    │ ν₁ ≥ ν₂ ≥ … ≥ ν_N │
                    └─────────────────┘
                             │
                    ┌─────────────────┐
                    │  NGW scheme      │
                    │  N̄ = 4, 8, 12 or 16 │
                    └─────────────────┘
```
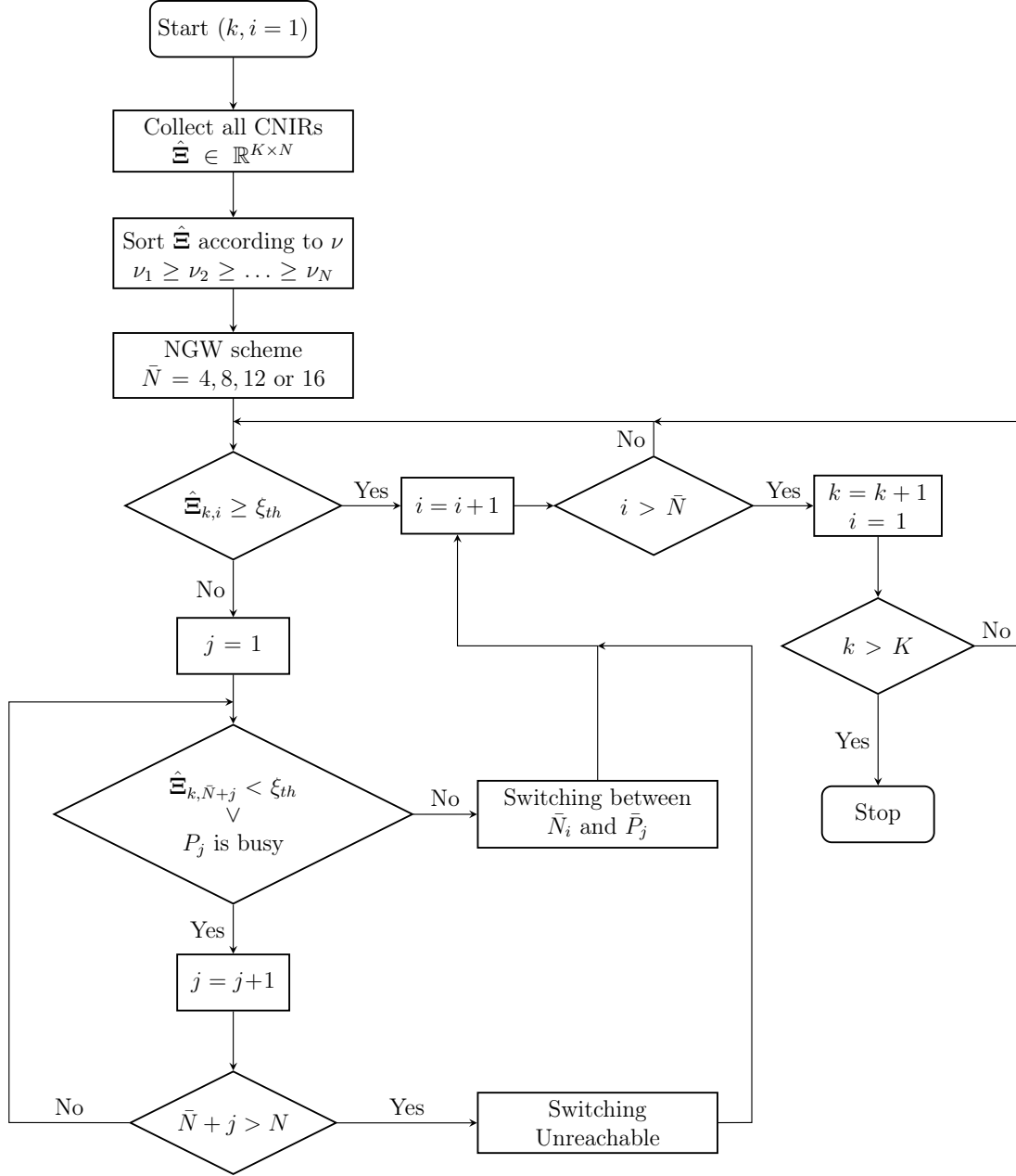
Figure 6.1: Flowchart of the multiple $1 + \bar{P}$ switching strategy.

6.3.1 Method to Calculate the Probability of Rain, P_0

To begin with, the ITU Recommendation ITU-R P.837 includes digital maps with information about the monthly mean total rainfall data, MT_{ii}, and the annual rainfall rate data exceeded for 0.01% of an average year, $R_{0.01}$. In both cases, these maps are georeferenced by grids of geographical coordinates. For the MT_{ii} map, each coordinate of latitude and longitude is separated by steps with a resolution of $0.25°$, whereas a resolution of $0.125°$ for the $R_{0.01}$ map.

In this context, the ITU-R P.837 method enables three input parameters, which are the desired annual probability of exceedance, p_d [%], the latitude of the desired location Lat_i [degrees], and the longitude of the desired location Lon_i [degrees]. Table A.2 shows the latitude, Lat_i, and longitude, Lon_i, for each $i = 1, 2, \ldots, N$. Also, the method generates two output parameters, which are the rainfall rate exceeded for the desired probability of exceedance, R_p [mm/h], and the annual probability of rain, P_{0_i} [%]. The ITU-R P.837 method [29] is discussed and developed in the following.

- **Step 1:** Table 6.1 indicates the representations of months to employ in this method. Let ii the month number and let N_{ii} the number of days in each month.

Table 6.1: Month Numbers and Number of Days

Month	Jan	Feb	Mar	Apr	May	Jun	Jul	Aug	Sep	Oct	Nov	Dec
ii	01	02	03	04	05	06	07	08	09	10	11	12
N_{ii}	31	28.25	31	30	31	30	31	31	30	31	30	31

- **Step 2:** Determine the monthly mean surfaces temperatures, T_{ii} [K], at the i-th GW location (Lat_i, Lon_i), where $ii = \{01, 02, 03, \ldots, 12\}$ and $i = 1, 2, \ldots, N$. In this case, the monthly mean surface temperatures are obtained from the digital maps included in ITU Recommendation ITU-R P.1510 [34].

- **Step 3:** Likewise, determine the monthly mean total rainfall, MT_{ii}, at the i-th GW location (Lat_i, Lon_i), from the digital maps included in this ITU Recommendation. However, to determine the MT_{ii} at the specific site (Lat_i, Lon_i), it is necessary to use bilinear interpolation, which gives by the ITU Recommendation ITU-R P.1144 in more detail [33].

- **Step 4:** Convert the temperature T_{ii}[K] to t_{ii}[°C], for each month number, ii.

- **Step 5:** Calculate r_{ii} [mm/h] for each month number as follows

$$
\begin{array}{ll}
r_{ii} = 0.5874 \cdot \exp\left(0.0833 \cdot t_{ii}\right) & \text{for } t_{ii} \geq 0°C \\
r_{ii} = 0.5874 & \text{for } t_{ii} < 0°C
\end{array}
\tag{6.7}
$$

- **Step 6a:** Calculate the monthly probability of rain [%] for each month number, ii, as follows

$$
P_{0_{ii}} = 100 \cdot \frac{MT_{ii}}{24 \cdot N_{ii} \cdot r_{ii}}
\tag{6.8}
$$

- **Step 6b:** if $P_{0_{ii}} > 70$, then set $P_{0_{ii}} = 70$ and $r_{ii} = \frac{100}{70} \cdot \frac{MT_{ii}}{24 \cdot N_{ii}}$

- **Step 7:** For each i-th GW location, calculate the annual probability of rain, $P_{0_i} = P(R > 0)$ [%] as follows

$$
P_{0_i} = \frac{\sum_{ii=1}^{12} N_{ii} \cdot P_{0_{ii}}}{365.25}, \text{for } i = 1, 2, \ldots, N
\tag{6.9}
$$

- **Step 8:** In this case, it is not necessary to find R_p for this study. For further details, consult the ITU-R P.837 [29].

It is important to note that the probabilities of rain P_{0_i} and P_i^{rain} are the same but using different notations. The first one is well-known by the ITU-R P.837, whereas the ITU-R P.618 uses the second one often [28, 29].

6.3.2 The Switching Strategy, $1 + \bar{P}$, from the perspective of a Markov Chain

Calculated the annual probability of rain, $P_{0_i}(Lat_i, Lon_i, p_d)$, for each i-th GW-site by Table A.2 coordinates, the GWs can be sorted from the best to the worst regarding no-rain probabilities by each site, so that $1 - P_{0_1} \geq 1 - P_{0_2} \geq \ldots \geq 1 - P_{0_N}$. Likewise, the best first $\bar{N}$ sites are assigned to be part of the NGWs scheme, whereas the rest of the sites are becoming part of the PGWs as those are added to the ground network later. Although this analysis is using the Markov Chain, the switching mechanism is similar to the scheme $1 + \bar{P}$, as was discussed in subsection 6.2.4 in more detail.

Thus, each GW has three states, the active state, non-active state, and the switching state. The active state is related to the no-rain probability at each GW-site, whereas the non-active state occurs as one of the NGWs of the ground network experiences an outage due to the rain, i.e., there is a total outage probability of the system, P_{out}. At this point, the switching state works as a link between the affected NGW and the picked PGW. It is important to note that there is always a strong emphasis on the first PGW. Nonetheless, if the mentioned PGW is busy or in a feeder-uplink outage, the transition probability goes to the next switching state towards an available PGW, and so on.

As a result, the first three states correspond to the analyzed NGW, whereas the next states, in threes, are for each PGW. Figure 6.2 shows the transition probabilities from one state to another by a Markov chain graph. Also, as the Markov chain is a discrete-time process, it can be represented by a state transition matrix $\mathbf{P}$, for $i = 1, 2, \ldots, \bar{N}$ and $j = 1, 2, \ldots, \bar{P}$, as can be seen in Eq. (6.10).

In general terms, the stationary distribution is the fraction of time that the system spends in each state as the number of samples tends to the infinity. As a result, if there are $3(1+\bar{P})$ states, then the stationary distribution is a vector of length $3(1+\bar{P})$. Indeed, the stationary distribution is usually referred to as π and is given by

$$\pi = \mathbf{s}_0 \cdot \mathbf{P}^n, n \to \infty \tag{6.11}$$

where n is the number of iterations and $\mathbf{s}_0$ is the initial state vector $\mathbf{s}_0 = [1, 0, 0, \ldots, 0] \in [0, 1]^{3(1+\bar{P})}$. In this context, a Markov chain is stationary with stationary distribution π if $\pi \cdot \mathbf{P} = \pi$, and $\sum_{i=1}^{3(1+\bar{P})} \pi_i = 1$, where $\pi = [\pi_1, \pi_2, \ldots, \pi_{3(1+\bar{P})}]$. Therefore, the switching probability is calculated as

$$P_{sw} = \pi_3 + \pi_6 + \ldots + \pi_{3(1+j)}, \text{for } j = 0, 1, 2 \ldots, \bar{P} \tag{6.12}$$
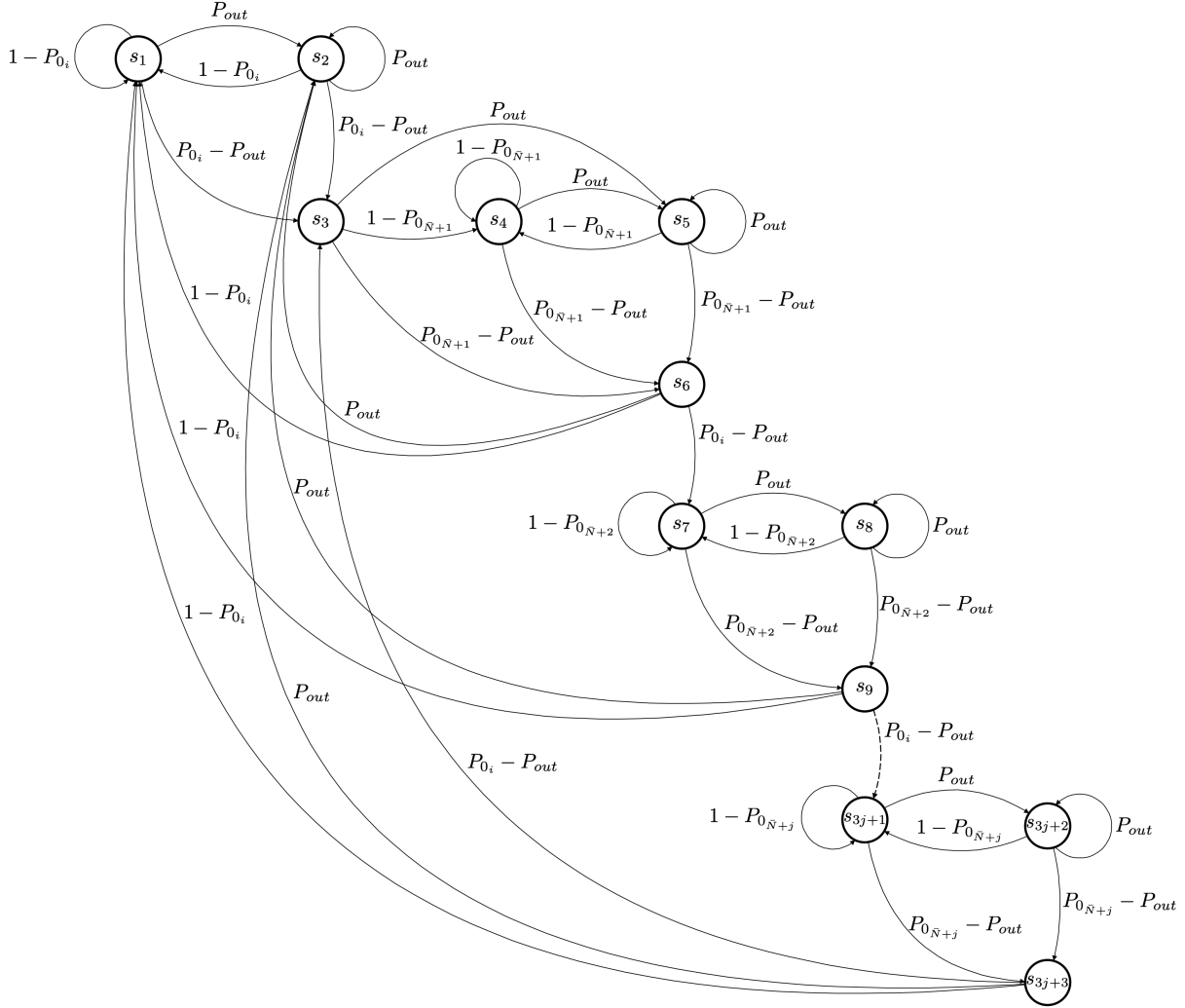
Figure 6.2: The $1 + \bar{P}$ strategy represented by a Markov Chain graph.

Finally, the switching rate is calculated by $R_{sw} = P_{sw}/T_{sw}$, where T_{sw} is the interval between switching instants [21,98]. This switching rate is important to determine the effectiveness of the switching strategy in addition to finding the optimal number of PGWs necessary to maintain the availability of the ground network above 99.9%.

6.4   Results

To begin with, the smart method to predict both rain attenuation time-series and CNIR time-series at each GW was trained and validated in Chapter 5 by Experiment 2. This method found a model with an average accuracy of 87.83%, generating high-reliability results in comparison with other models.

Each ground network configuration has a different capacity, depending on the number of NGWs. By using Eq. (6.1), it was possible to find the feeder uplink capacity at each GW location. For this purpose, the V band provided 4 GHz of

$$
\mathbf{P} =
\begin{array}{c|ccccccccccccc}
 & s_1 & s_2 & s_3 & s_4 & s_5 & s_6 & s_7 & s_8 & s_9 & \cdots & s_{3j+1} & s_{3j+2} & s_{3j+3} \\
\hline
s_1 & 1-P_{0_i} & P_{out} & P_{0_i}-P_{out} & 0 & 0 & 0 & 0 & 0 & 0 & \cdots & 0 & 0 & 0 \\
s_2 & 1-P_{0_i} & P_{out} & P_{0_i}-P_{out} & 0 & 0 & 0 & 0 & 0 & 0 & \cdots & 0 & 0 & 0 \\
s_3 & 0 & 0 & 0 & 1-P_{0_{\bar N+1}} & P_{out} & P_{0_{\bar N+1}}-P_{out} & 0 & 0 & 0 & \cdots & 0 & 0 & 0 \\
s_4 & 0 & 0 & 0 & 1-P_{0_{\bar N+1}} & P_{out} & P_{0_{\bar N+1}}-P_{out} & 0 & 0 & 0 & \cdots & 0 & 0 & 0 \\
s_5 & 1-P_{0_i} & P_{out} & 0 & 1-P_{0_{\bar N+1}} & P_{out} & P_{0_{\bar N+1}}-P_{out} & 0 & 0 & 0 & \cdots & 0 & 0 & 0 \\
s_6 & 0 & 0 & 0 & 0 & 0 & 0 & P_{0_i}-P_{out} & P_{out} & P_{0_{\bar N+2}}-P_{out} & \cdots & 0 & 0 & 0 \\
s_7 & 0 & 0 & 0 & 0 & 0 & 0 & 1-P_{0_{\bar N+2}} & P_{out} & P_{0_{\bar N+2}}-P_{out} & \cdots & 0 & 0 & 0 \\
s_8 & 1-P_{0_i} & P_{out} & 0 & 0 & 0 & 0 & 1-P_{0_{\bar N+2}} & 0 & 0 & \cdots & 0 & 0 & 0 \\
s_9 & 0 & 0 & 0 & 0 & 0 & 0 & 0 & 0 & 0 & \cdots & 0 & 0 & 0 \\
\cdots & \cdots & \cdots & \cdots & \cdots & \cdots & \cdots & \cdots & \cdots & \cdots & \cdots & \cdots & \cdots & \cdots \\
s_{3j+1} & 0 & 0 & 0 & 0 & 0 & 0 & 0 & 0 & 0 & \cdots & 1-P_{0_{\bar N+j}} & P_{out} & P_{0_{\bar N+j}}-P_{out} \\
s_{3j+2} & 0 & 0 & 0 & 0 & 0 & 0 & 0 & 0 & 0 & \cdots & 1-P_{0_{\bar N+j}} & P_{out} & P_{0_{\bar N+j}}-P_{out} \\
s_{3j+3} & 1-P_{0_i} & P_{out} & P_{0_i}-P_{out} & 0 & 0 & 0 & 0 & 0 & 0 & \cdots & 0 & 0 & 0 \\
\end{array}
\tag{6.10}
$$

available spectrum, S_{avail}. Furthermore, the feeder uplink models employed the 1F2P scheme so that they did not use frequency reuse, $N_{sb} = 1$, however, they employed double polarization, $N_p = 2$. In order to determine the maximum capacity, each feeder uplink was defined to work under clear sky conditions. Therefore, the best MODCOD, 256 APSK 3/4, based on DVB-S2X, has a spectral efficiency of 5.6199 b/s/Hz with a roll-off of 5%, as can be seen in Chapter 3. As a result, all feeder uplinks obtained an individual capacity of 44.96 Gb/s.

Consequently, the inbound capacity was calculated by Eq. (6.2) and using schemes $\bar{N} = 4, 8, 12$, and 16. To be precise, Table 6.2 indicates the inbound capacity of an HTS system for each $\bar{N}$ scheme with a traffic ratio of [1 : 1].

Table 6.2: The Inbound and Total Capacity of the Ground Network Segment.

Scheme $\bar{N}$	Inbound Capacity [Gb/s]	Total Capacity [Gb/s]
4	179.84	≈ 360.00
8	359.68	≈ 720.00
12	539.52	≈ 1000.00
16	719.36	≈ 1400.00

The matrix $\hat{\Xi} \in \mathbb{R}^{K \times N}$ contains the predicted CNIR time-series of each GW obtained from the deep learning model. To be specific, 24 GW locations (Table A.2) were trained and validated by the machine learning model, as can be seen in Chapter 5. Thus, the availability, ν_i, of each feeder uplink was calculated by Eq. (6.3). For this purpose, the CNIR threshold varied from 0–29 dB to verify the feeder uplink behavior at each step, in addition to sorting the obtained availability from the best to the worst for each $\bar{N}$ configuration scheme. The best $\bar{N}$s, according to availability, were part of each ground network configuration, finding the system availability, ν, for each $\bar{N}$ configuration scheme by using Eq. (6.4).

Figure 6.3 depicts the unavailability percentage, $1 - \nu$ [%], vs. the CNIR threshold range, ξ_{th}, for all configuration schemes, $\bar{N} = 4, 8, 12, 16$. In this case, $\xi_{th} = 14$ dB was a good measure as for all $\bar{N}$ schemes, the system unavailability percentage was lower than 5% per year. For $1 - \nu > 5\%$, the system unavailability increased considerably, so that the number of outages of the system could be tough to manage.

The capacity of the feeder uplink is also affected by the rain. For this reason, the CNIR threshold must be capable of balancing as the system available as the capacity of the feeder uplink. Figure 6.4 shows how the threshold $\xi_{th} = 14$ dB indicates the limit of the system availability, ν, not to be lower than 0.95, and the capacity of feeder uplinks, on average, must not be lower than 44.70 Gb/s.

Here the desired availability, ν_i of each feeder uplink for the GW set, $[N] = \{1, 2, \ldots, 24\}$, was calculated using the threshold $\xi_{th} = 14$ dB by Eq. (6.3). Then, the GW locations were sorted from the highest to the lowest according to the availability. Table 6.3 shows the sorted availabilities where the best $\bar{N}$ GWs correspond to the number of GWs according to the ground network configuration, $\bar{N} = 4, 8, 12, 16$. As a result, none of the four configuration schemes reached the minimum system
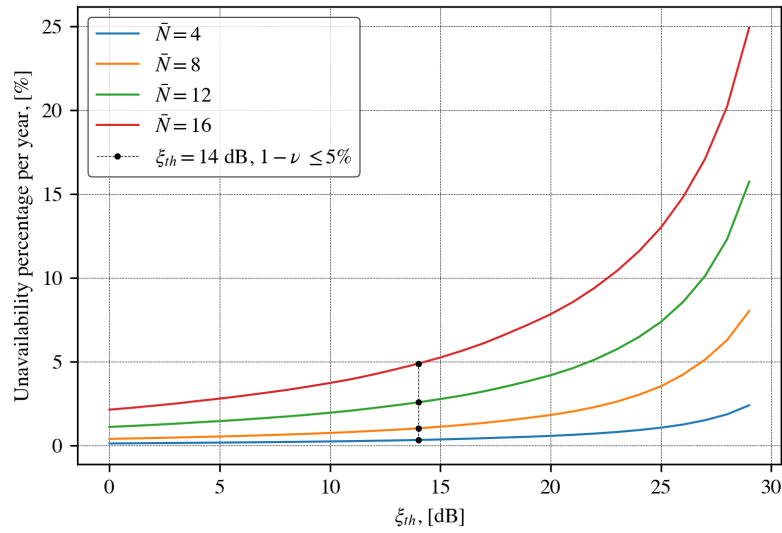
Figure 6.3: Unavailability percentage per year, for all $\bar{N}$ configuration schemes.
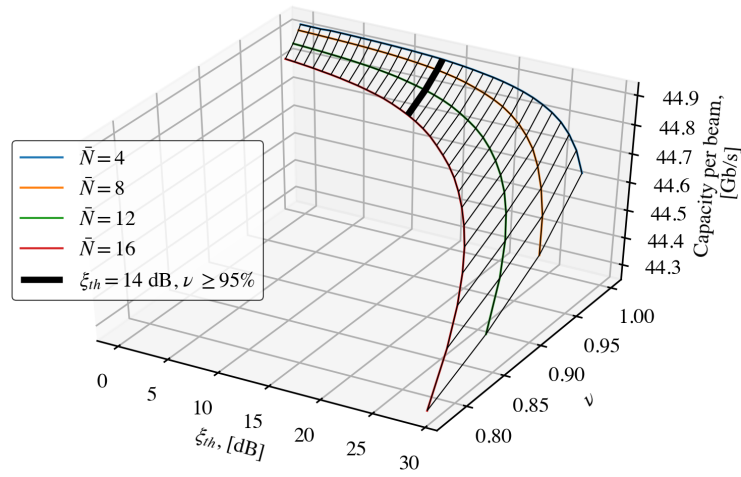
Figure 6.4: System availability vs. the feeder uplink capacity, on average, by ranging the CNIR threshold, ξ_{th}.

availability, established in 99.90%. Therefore, all schemes must add redundancy to outperform the required minimum availability.

Table 6.3: Gateway Availabilities.

Locations $[N] = \{1, 2, \ldots, 24\}$	Availability ν_i	$\bar{N} = 4$	$\bar{N} = 8$	$\bar{N} = 12$	$\bar{N} = 16$
Torreon	0.9994	$\bar{N}_1$	$\bar{N}_1$	$\bar{N}_1$	$\bar{N}_1$
Cd. Juarez	0.9992	$\bar{N}_2$	$\bar{N}_2$	$\bar{N}_2$	$\bar{N}_2$
La Paz, B.C.	0.9992	$\bar{N}_3$	$\bar{N}_3$	$\bar{N}_3$	$\bar{N}_3$
Tijuana	0.9990	$\bar{N}_4$	$\bar{N}_4$	$\bar{N}_4$	$\bar{N}_4$
Oaxaca	0.9986	$\bar{P}_{\bar{N}+1}$	$\bar{N}_5$	$\bar{N}_5$	$\bar{N}_5$
Queretaro	0.9985	$\bar{P}_{\bar{N}+2}$	$\bar{N}_6$	$\bar{N}_6$	$\bar{N}_6$
Mexico City	0.9982	$\bar{P}_{\bar{N}+3}$	$\bar{N}_7$	$\bar{N}_7$	$\bar{N}_7$
Guadalajara	0.9977	$\bar{P}_{\bar{N}+4}$	$\bar{N}_8$	$\bar{N}_8$	$\bar{N}_8$
Monterrey	0.9968	$\bar{P}_{\bar{N}+5}$	$\bar{P}_{\bar{N}+1}$	$\bar{N}_9$	$\bar{N}_9$
Tegucigalpa	0.9963	$\bar{P}_{\bar{N}+6}$	$\bar{P}_{\bar{N}+2}$	$\bar{N}_{10}$	$\bar{N}_{10}$
Merida	0.9961	$\bar{P}_{\bar{N}+7}$	$\bar{P}_{\bar{N}+3}$	$\bar{N}_{11}$	$\bar{N}_{11}$
Tuxtla, Gtz.	0.9953	$\bar{P}_{\bar{N}+8}$	$\bar{P}_{\bar{N}+4}$	$\bar{N}_{12}$	$\bar{N}_{12}$
La Habana	0.9949	$\bar{P}_{\bar{N}+9}$	$\bar{P}_{\bar{N}+5}$	$\bar{P}_{\bar{N}+1}$	$\bar{N}_{13}$
Kingston	0.9942	$\bar{P}_{\bar{N}+10}$	$\bar{P}_{\bar{N}+6}$	$\bar{P}_{\bar{N}+2}$	$\bar{N}_{14}$
San Jose	0.9941	$\bar{P}_{\bar{N}+11}$	$\bar{P}_{\bar{N}+7}$	$\bar{P}_{\bar{N}+3}$	$\bar{N}_{15}$
Cancun	0.9938	$\bar{P}_{\bar{N}+12}$	$\bar{P}_{\bar{N}+8}$	$\bar{P}_{\bar{N}+4}$	$\bar{N}_{16}$
Veracruz	0.9934	$\bar{P}_{\bar{N}+13}$	$\bar{P}_{\bar{N}+9}$	$\bar{P}_{\bar{N}+5}$	$\bar{P}_{\bar{N}+1}$
San Pedro Sula	0.9932	$\bar{P}_{\bar{N}+14}$	$\bar{P}_{\bar{N}+10}$	$\bar{P}_{\bar{N}+6}$	$\bar{P}_{\bar{N}+2}$
Belmopan	0.9925	$\bar{P}_{\bar{N}+15}$	$\bar{P}_{\bar{N}+11}$	$\bar{P}_{\bar{N}+7}$	$\bar{P}_{\bar{N}+3}$
San Salvador	0.9917	$\bar{P}_{\bar{N}+16}$	$\bar{P}_{\bar{N}+12}$	$\bar{P}_{\bar{N}+8}$	$\bar{P}_{\bar{N}+4}$
St. Domingo	0.9911	$\bar{P}_{\bar{N}+17}$	$\bar{P}_{\bar{N}+13}$	$\bar{P}_{\bar{N}+9}$	$\bar{P}_{\bar{N}+5}$
San Juan	0.9902	$\bar{P}_{\bar{N}+18}$	$\bar{P}_{\bar{N}+14}$	$\bar{P}_{\bar{N}+10}$	$\bar{P}_{\bar{N}+6}$
Panama	0.9898	$\bar{P}_{\bar{N}+19}$	$\bar{P}_{\bar{N}+15}$	$\bar{P}_{\bar{N}+11}$	$\bar{P}_{\bar{N}+7}$
Pto. Cabezas	0.9889	$\bar{P}_{\bar{N}+20}$	$\bar{P}_{\bar{N}+16}$	$\bar{P}_{\bar{N}+12}$	$\bar{P}_{\bar{N}+8}$
System Availability, ν [%]		99.68%	98.98%	97.46%	95.23%

In this context, the proposed strategy was carried out in this analysis by the switching mechanism, $1+\bar{P}$. Table 6.4 indicates the number of feeder uplink outages of each NGW, backing up by one PGW, at a year-round. Table 6.5 shows the combined availability between NGW and PGW, proving the increase of availability of each feeder uplink. As a result, only one redundant GW was necessary to overcome the required system availability, picking out Oaxaca as the backup GW. Therefore, the optimized scheme was $4 + 1$.

For the scheme $8 + \bar{P}$, two PGWs (Monterrey and Tegucigalpa) were necessary to back up the ground network about 100%. Table 6.6 displays the number of outages of each NGW, where $\bar{P}_1$ (Monterrey) backs up 99% of feeder uplink outages from all NGWs. Table 6.7 shows the system availability with and without redundancy. In this case, only one PGW (Monterrey) was needful to overcome the required system availability (99.9%), obtaining a 99.99%. Therefore, the $8 + 1$ scheme met the aim of improving the required system availability.

Table 6.4: The Number of Outages of Each NGW for the $4 + \bar{P}$ Scheme.

Locations $[\bar{N}] = \{1, 2, 3, 4\}$	Oaxaca $\bar{P}_1$
Torreon	293
Cd. Juarez	412
La Paz, B.C.	444
Tijuana	549
Total Outages	1698

Table 6.5: The System Availability for the $4 + \bar{P}$ Scheme.

Locations $[\bar{N}] = \{1, 2, 3, 4\}$	$4 + 0$	$4 + 1$
Torreon	0.9994	1.0000
Cd. Juarez	0.9992	1.0000
La Paz, B.C.	0.9992	1.0000
Tijuana	0.9990	1.0000
ν_B [%]	99.68%	100.0%

Table 6.6: The Number of Outages of Each NGW for the $8 + \bar{P}$ Scheme.

Locations $[\bar{N}] = \{1, 2, \ldots, 8\}$	Monterrey $\bar{P}_1$	Tegucigalpa $\bar{P}_2$
Torreon	292	1
Cd. Juarez	412	0
La Paz, B.C.	444	0
Tijuana	549	0
Oaxaca	730	0
Queretaro	793	20
Mexico City	907	24
Guadalajara	1190	6
Total Outages	5317	51

Table 6.7: The System Availability for the $8 + \bar{P}$ Scheme.

Locations $[\bar{N}] = \{1, 2, \ldots, 8\}$	$8 + 0$	$8 + 1$	$8 + 2$
Torreon	0.9994	0.9999	1.0000
Cd. Juarez	0.9992	1.0000	1.0000
La Paz, B.C.	0.9992	1.0000	1.0000
Tijuana	0.9990	1.0000	1.000
Oaxaca	0.9986	1.0000	1.0000
Queretaro	0.9985	0.9999	1.0000
Mexico City	0.9982	0.9999	1.0000
Guadalajara	0.9977	0.9999	1.0000
ν_B [%]	98.98%	99.99%	100.0%

Likewise, Table 6.8 indicates the feeder uplink outages for the scheme $12 + \bar{P}$, where two PGWs (La Habana and Kingston) support all outages. Naturally, the $\bar{P}_1$ (La Habana) backed up 98.9%of the feeder uplink outages for all NGWs. Table 6.9 exhibits the system availability for $12 + \bar{P}$ schemes. The switching strategy gave two PGWs as a result, but only one PGW (La Habana) was useful to improve the system availability of the ground network. For this reason, the $12 + 1$ scheme overcame the required system availability, providing a 99.97%.

Table 6.8: The Number of Outages of Each NGW for the $12 + \bar{P}$ Scheme.

Locations $[\bar{N}] = \{1, 2, \ldots, 12\}$	La Habana $\bar{P}_1$	Kingston $\bar{P}_2$
Torreon	292	1
Cd. Juarez	412	0
La Paz, B.C.	444	0
Tijuana	547	2
Oaxaca	730	0
Queretaro	810	3
Mexico City	898	33
Guadalajara	1189	7
Monterrey	1668	30
Tegucigalpa	1892	30
Merida	2052	7
Tuxtla, Gtz.	2419	40
Total Outages	13353	153

Table 6.9: The System Availability for the $12 + \bar{P}$ Scheme.

Locations $[\bar{N}] = \{1, 2, \ldots, 12\}$	$12 + 0$	$12 + 1$	$12 + 2$
Torreon	0.9994	0.9999	1.0000
Cd. Juarez	0.9992	1.0000	1.0000
La Paz, B.C.	0.9992	1.0000	1.0000
Tijuana	0.9990	0.9999	1.0000
Oaxaca	0.9986	1.0000	1.0000
Queretaro	0.9985	0.9999	1.0000
Mexico City	0.9982	0.9999	1.0000
Guadalajara	0.9977	0.9999	1.0000
Monterrey	0.9968	0.9999	1.0000
Tegucigalpa	0.9963	0.9999	1.0000
Merida	0.9961	0.9999	1.0000
Tuxtla, Gtz.	0.9953	0.9999	1.0000
ν_B [%]	97.46%	99.97%	100.0%

In the last case, the results of the evaluated $16 + \bar{P}$ scheme were published by Tables 6.10 and 6.11. In the same context, Table 6.10 shows the number of

feeder uplink outages in each NGW, whereas three PGWs (Veracruz, San Pedro Sula, and Belmopan) give support to them. The first $\bar{P}_1$ (Veracruz) provided support to the ground network in 97.72% of the time. Table 6.11 indicates the system availability of each $16+\bar{P}$ configuration scheme. To be precise, the scheme needed two PGWs (Veracruz and San Pedro Sula) to outperform the required system availability. Consequently, the optimal scheme resulted in $16 + 2$, providing a system availability of 99.99%.

Table 6.10: The Number of Outages of Each NGW for the $16 + \bar{P}$ Scheme.

Locations $[\bar{N}] = \{1, 2, \ldots, 16\}$	Veracruz $\bar{P}_1$	San Pedro Sula $\bar{P}_2$	Belmopan $\bar{P}_3$
Torreon	293	0	0
Cd. Juarez	412	0	0
La Paz, B.C.	444	0	0
Tijuana	548	1	0
Oaxaca	705	25	0
Queretaro	808	5	0
Mexico City	905	23	3
Guadalajara	1173	23	0
Monterrey	1664	34	0
Tegucigalpa	1882	40	0
Merida	2044	15	0
Tuxtla, Gtz.	2409	50	0
La Habana	2653	39	1
Kingston	2973	95	0
San Jose	3025	82	1
Cancun	3124	148	0
Total Outages	25062	580	5

Finally, for better visualization, these results can be presented in an unavailability graph. Figure 6.5 depicts the different $\bar{N} + \bar{P}$ schemes, where the minimum reference is 1×10^{-3} (99.9%). Hence, it is possible to perceive the best schemes that overcome the reference 1×10^{-3}, which are: $4 + 1$, $8 + 1$, $12 + 1$, and $16 + 2$. However, it is impossible to have an ideal system availability, that is, an availability of 100.0%. Although it is theoretically possible to obtain 100.0% of availability, a more realistic scenario could be as the best unavailability reaches a value of 1×10^{-7}.

For the Markov Chain method, it was necessary to obtain the probability of rain of each GW-site, P_{0_i}, by the ITU Recommendation ITU-R P.837, as can be seen in the subsection 6.3.1. Then, the operation (no-rain) probabilities were sorted from the result of the expression $1 - P_{0_i}$, i.e., from the highest to the lowest. Table 6.12 shows the sorted operation probability of each GW-site. Here, the best $\bar{N}$ GWs became part of the ground network according to the $\bar{N}$ schemes, $4, 8, 12$, and 16.

By applying the switching strategy of Section 6.3, the stationary distribution, π, of each $1+\bar{P}$ scheme was obtained from the state transition matrix, Eq. 6.10. For this purpose, the system outage probability, P_{out}, was set in 1×10^{-4}. Table 6.13 presents

Table 6.11: The System Availability for the $16 + \bar{P}$ Scheme.

Locations $[\bar{N}] = \{1, 2, \ldots, 16\}$	$16 + 0$	$16 + 1$	$16 + 2$	$16 + 3$
Torreon	0.9994	1.0000	1.0000	1.0000
Cd. Juarez	0.9992	1.0000	1.0000	1.0000
La Paz, B.C.	0.9992	1.0000	1.0000	1.0000
Tijuana	0.9990	0.9999	1.0000	1.0000
Oaxaca	0.9986	0.9999	1.0000	1.0000
Queretaro	0.9985	0.9999	1.0000	1.0000
Mexico City	0.9982	0.9998	0.9999	1.0000
Guadalajara	0.9977	0.9999	1.0000	1.0000
Monterrey	0.9968	0.9999	1.0000	1.0000
Tegucigalpa	0.9963	0.9999	1.0000	1.0000
Merida	0.9961	0.9999	1.0000	1.0000
Tuxtla, Gtz.	0.9953	0.9999	1.0000	1.0000
La Habana	0.9949	0.9998	0.9999	1.0000
Kingston	0.9942	0.9999	1.0000	1.0000
San Jose	0.9941	0.9998	0.9999	1.0000
Cancun	0.9938	0.9999	1.0000	1.0000
ν_B [%]	95.23%	99.89%	99.99%	100.0%
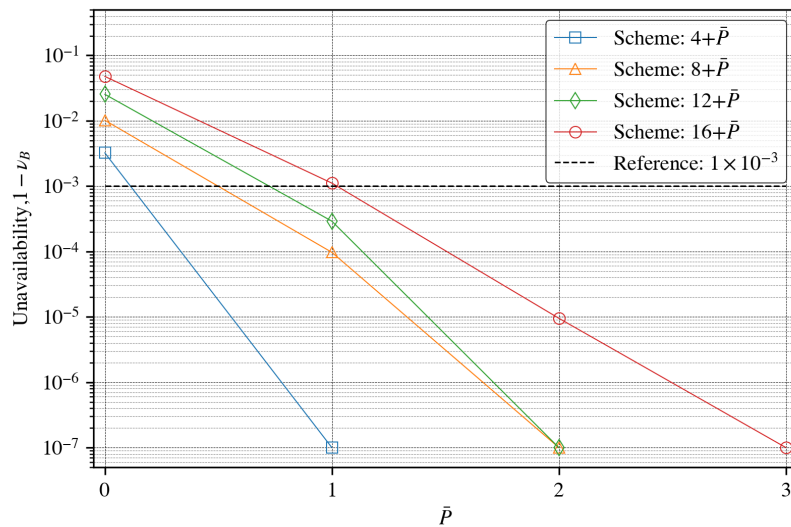
Figure 6.5: Performance of the $\bar{N} + \bar{P}$ schemes, as a function of system unavailability and the number of $\bar{P}$.

Table 6.12: The Operation Probability of Gateways.

Locations $[N] = \{1, 2, \ldots, 24\}$	Operation Probability $1 - P_{0_i}$	$\bar{N} = 4$	$\bar{N} = 8$	$\bar{N} = 12$	$\bar{N} = 16$
La Paz, B.C.	0.9962	$\bar{N}_1$	$\bar{N}_1$	$\bar{N}_1$	$\bar{N}_1$
Torreon	0.9945	$\bar{N}_2$	$\bar{N}_2$	$\bar{N}_2$	$\bar{N}_2$
Cd. Juarez	0.9920	$\bar{N}_3$	$\bar{N}_3$	$\bar{N}_3$	$\bar{N}_3$
Merida	0.9840	$\bar{N}_4$	$\bar{N}_4$	$\bar{N}_4$	$\bar{N}_4$
Monterrey	0.9835	$\bar{P}_{\bar{N}+1}$	$\bar{N}_5$	$\bar{N}_5$	$\bar{N}_5$
Tijuana	0.9826	$\bar{P}_{\bar{N}+2}$	$\bar{N}_6$	$\bar{N}_6$	$\bar{N}_6$
Queretaro	0.9797	$\bar{P}_{\bar{N}+3}$	$\bar{N}_7$	$\bar{N}_7$	$\bar{N}_7$
Cancun	0.9752	$\bar{P}_{\bar{N}+4}$	$\bar{N}_8$	$\bar{N}_8$	$\bar{N}_8$
Oaxaca	0.9738	$\bar{P}_{\bar{N}+5}$	$\bar{P}_{\bar{N}+1}$	$\bar{N}_9$	$\bar{N}_9$
La Habana	0.9729	$\bar{P}_{\bar{N}+6}$	$\bar{P}_{\bar{N}+2}$	$\bar{N}_{10}$	$\bar{N}_{10}$
Tegucigalpa	0.9728	$\bar{P}_{\bar{N}+7}$	$\bar{P}_{\bar{N}+3}$	$\bar{N}_{11}$	$\bar{N}_{11}$
Tuxtla, Gtz.	0.9727	$\bar{P}_{\bar{N}+8}$	$\bar{P}_{\bar{N}+4}$	$\bar{N}_{12}$	$\bar{N}_{12}$
Guadalajara	0.9723	$\bar{P}_{\bar{N}+9}$	$\bar{P}_{\bar{N}+5}$	$\bar{P}_{\bar{N}+1}$	$\bar{N}_{13}$
Kingston	0.9714	$\bar{P}_{\bar{N}+10}$	$\bar{P}_{\bar{N}+6}$	$\bar{P}_{\bar{N}+2}$	$\bar{N}_{14}$
Veracruz	0.9709	$\bar{P}_{\bar{N}+11}$	$\bar{P}_{\bar{N}+7}$	$\bar{P}_{\bar{N}+3}$	$\bar{N}_{15}$
St. Domingo	0.9671	$\bar{P}_{\bar{N}+12}$	$\bar{P}_{\bar{N}+8}$	$\bar{P}_{\bar{N}+4}$	$\bar{N}_{16}$
San Juan	0.9671	$\bar{P}_{\bar{N}+13}$	$\bar{P}_{\bar{N}+9}$	$\bar{P}_{\bar{N}+5}$	$\bar{P}_{\bar{N}+1}$
Mexico City	0.9645	$\bar{P}_{\bar{N}+14}$	$\bar{P}_{\bar{N}+10}$	$\bar{P}_{\bar{N}+6}$	$\bar{P}_{\bar{N}+2}$
San Salvador	0.9638	$\bar{P}_{\bar{N}+15}$	$\bar{P}_{\bar{N}+11}$	$\bar{P}_{\bar{N}+7}$	$\bar{P}_{\bar{N}+3}$
San Pedro Sula	0.9614	$\bar{P}_{\bar{N}+16}$	$\bar{P}_{\bar{N}+12}$	$\bar{P}_{\bar{N}+8}$	$\bar{P}_{\bar{N}+4}$
Panama	0.9592	$\bar{P}_{\bar{N}+17}$	$\bar{P}_{\bar{N}+13}$	$\bar{P}_{\bar{N}+9}$	$\bar{P}_{\bar{N}+5}$
Belmopan	0.9568	$\bar{P}_{\bar{N}+18}$	$\bar{P}_{\bar{N}+14}$	$\bar{P}_{\bar{N}+10}$	$\bar{P}_{\bar{N}+6}$
Pto. Cabezas	0.9473	$\bar{P}_{\bar{N}+19}$	$\bar{P}_{\bar{N}+15}$	$\bar{P}_{\bar{N}+11}$	$\bar{P}_{\bar{N}+7}$
San Jose	0.9356	$\bar{P}_{\bar{N}+20}$	$\bar{P}_{\bar{N}+16}$	$\bar{P}_{\bar{N}+12}$	$\bar{P}_{\bar{N}+8}$
System Operation Probability, [%]		96.70%	89.28%	80.03%	70.97%

the stationary distribution of each NGW for the $4 + \bar{P}$ scheme. Although each π has 63 states, only the first 12 states were necessary for this analysis as the next probabilities were practically negligible. Table 6.14 displays the system operation probabilities for each $4 + \bar{P}$ scheme. In this case, the scheme $4 + 2$ overcame the required system availability of 99.9% in terms of probability. The two picked redundant GWs were Monterrey and Tijuana. It is important to note that the inactive states were not considered to determine the operation probability.

Table 6.15 and Table 6.16 indicate the stationary distribution and the system operation probabilities for the $8 + \bar{P}$ Scheme, respectively. In this case, each stationary distribution had 51 states, but only the first 12 states were useful to determine the number of PGWs to be added to the ground network. As a result, the scheme $8 + 3$ was the most suitable scheme (99.92%) to work above the reference (99.9%), in terms of probability. The three picked redundant GWs were Oaxaca, La Habana, and Tegucigalpa.

Table 6.13: The Stationary Distribution of Each NGW for the $4 + \bar{P}$ Scheme.

States	$\bar{N}_1$	$\bar{N}_2$	$\bar{N}_3$	$\bar{N}_4$
s_1	0.8114	0.7473	0.6705	0.4996
s_2	8.1449×10^{-5}	7.5146×10^{-5}	6.7586×10^{-5}	5.0776×10^{-5}
s_3	0.0030	0.0041	0.0053	0.0080
s_4	0.1818	0.2432	0.3164	0.4768
s_5	1.8485×10^{-5}	2.4726×10^{-5}	3.2171×10^{-5}	4.8480×10^{-5}
s_6	0.0030	0.0041	0.0053	0.0080
s_7	6.5697×10^{-4}	1.2762×10^{-3}	2.4081×10^{-3}	7.3383×10^{-3}
s_8	6.5704×10^{-8}	1.2764×10^{-7}	2.4084×10^{-7}	7.3390×10^{-7}
s_9	1.1356×10^{-5}	2.2061×10^{-5}	4.1626×10^{-5}	1.2685×10^{-4}
s_{10}	2.1016×10^{-6}	5.9290×10^{-6}	1.6224×10^{-5}	9.9978×10^{-5}
s_{11}	2.1018×10^{-10}	5.9296×10^{-10}	1.6226×10^{-9}	9.9988×10^{-9}
s_{12}	4.2484×10^{-8}	1.1986×10^{-7}	3.2797×10^{-7}	2.0211×10^{-6}

Table 6.14: The System Operation Probabilities for the $4 + \bar{P}$ Scheme.

Locations $[\bar{N}] = \{1, 2, 3, 4\}$	$4 + 0$	$4 + 1$	$4 + 2$	$4 + 3$
La Paz, B.C.	0.9962	0.9992	0.9999	0.9999
Torreon	0.9945	0.9986	0.9999	0.9999
Cd. Juarez	0.9920	0.9974	0.9999	0.9999
Merida	0.9840	0.9923	0.9998	0.9999
Operation Probability, [%]	96.70%	98.76%	99.95%	99.96%

Table 6.17 and Table 6.18 provide the results of the stationary distribution and the system operation probabilities for the $12 + \bar{P}$ Scheme, respectively. The total number of states of each stationary distribution was 39. However, the first 15 states of each distribution were required to evaluate the operation probability of the system. Consequently, the scheme $12 + 3$ obtained an operation probability of 99.90%, achieving the minimum requirement in terms of probability. The three picked redundant GWs were Guadalajara, Kingston, and Veracruz.

Finally, Table 6.19 and Table 6.20 give the outcomes obtained from the stationary distribution and the system operation probabilities for the $16 + \bar{P}$ Scheme, respectively. Each stationary distribution vector had a length of 27 elements or states, where the only first 15 states were necessary to obtain the operation probability of the system. To sum up, the scheme $16 + 4$ provided an operation probability of 99.91%, which outperformed the reference of 99.9%, in terms of probability. The four picked redundant GWs were San Juan, Mexico City, San Salvador, and San Pedro Sula.

It is important to note that all evaluated state-transition-matrices were ergodic and irreducibles. In other words, a Markov chain is ergodic if it is both irreducible and aperiodic. This condition is equivalent to the state transition matrix being a primitive non-negative matrix. In this context, ergodicity means the long-term proportion of time spent by the chain in state s_i, corresponding to the steady-state probability.

Table 6.15: The Stationary Distribution of Each NGW for the $8 + \bar{P}$ Scheme.

States	$\bar{N}_1$	$\bar{N}_2$	$\bar{N}_3$	$\bar{N}_4$	$\bar{N}_5$	$\bar{N}_6$	$\bar{N}_7$	$\bar{N}_8$
s_1	0.8714	0.8234	0.7623	0.6114	0.6041	0.5916	0.5526	0.5020
s_2	8.7480×10^{-5}	8.2793×10^{-5}	7.6842×10^{-5}	6.2140×10^{-5}	6.1426×10^{-5}	6.0208×10^{-5}	5.6407×10^{-5}	5.1473×10^{-5}
s_3	0.0033	0.0045	0.0060	0.0097	0.0099	0.0102	0.0112	0.0124
s_4	0.1215	0.1667	0.2238	0.3630	0.3696	0.3810	0.4162	0.4613
s_5	1.2474×10^{-5}	1.7116×10^{-5}	2.2982×10^{-5}	3.7277×10^{-5}	3.7961×10^{-5}	3.9127×10^{-5}	4.2740×10^{-5}	4.7369×10^{-5}
s_6	0.0033	0.0045	0.0060	0.0097	0.0099	0.0102	0.0112	0.0124
s_7	0.0005	0.0009	0.0018	0.0057	0.0060	0.0065	0.0084	0.0113
s_8	4.5125×10^{-8}	8.9921×10^{-8}	1.7509×10^{-7}	5.7431×10^{-7}	6.0280×10^{-7}	6.5392×10^{-7}	8.3537×10^{-7}	1.1296×10^{-6}
s_9	1.2197×10^{-5}	2.4306×10^{-5}	4.7327×10^{-5}	1.5524×10^{-4}	1.6294×10^{-4}	1.7675×10^{-4}	2.2580×10^{-4}	3.0532×10^{-4}
s_{10}	1.6812×10^{-6}	4.8653×10^{-6}	1.3739×10^{-5}	9.1128×10^{-5}	9.8584×10^{-5}	1.1256×10^{-4}	1.6816×10^{-4}	2.7742×10^{-4}
s_{11}	1.6813×10^{-10}	4.8658×10^{-10}	1.3740×10^{-9}	9.1137×10^{-9}	9.8594×10^{-9}	1.1257×10^{-8}	1.6818×10^{-8}	2.7744×10^{-8}
s_{12}	4.5630×10^{-8}	1.3205×10^{-7}	3.7289×10^{-7}	2.4734×10^{-6}	2.6757×10^{-6}	3.0550×10^{-6}	4.5641×10^{-6}	7.5296×10^{-6}

Table 6.16: The System Operation Probabilities for the $8 + \bar{P}$ Scheme.

Locations $[\bar{N}] = \{1, 2, \ldots, 8\}$	$8 + 0$	$8 + 1$	$8 + 2$	$8 + 3$
La Paz, B.C.	0.9962	0.9994	0.9999	0.9999
Torreon	0.9945	0.9990	0.9999	0.9999
Cd. Juarez	0.9920	0.9981	0.9999	0.9999
Merida	0.9840	0.9939	0.9998	0.9999
Monterrey	0.9835	0.9936	0.9998	0.9999
Tijuana	0.9826	0.9931	0.9998	0.9999
Queretaro	0.9797	0.9911	0.9997	0.9999
Cancun	0.9752	0.9880	0.9996	0.9999
Operation Probability, [%]	89.28%	95.70%	99.84%	99.92%

Table 6.17: The Stationary Distribution of Each NGW for the $12 + \bar{P}$ Scheme.

States	$\bar{N}_1$	$\bar{N}_2$	$\bar{N}_3$	$\bar{N}_4$	$\bar{N}_5$	$\bar{N}_6$	$\bar{N}_7$	$\bar{N}_8$	$\bar{N}_9$	$\bar{N}_{10}$	$\bar{N}_{11}$	$\bar{N}_{12}$
s_1	0.8773	0.8310	0.7718	0.6240	0.6168	0.6044	0.5657	0.5153	0.5004	0.4918	0.4907	0.4902
s_2	8.8067×10^{-5}	8.3559×10^{-5}	7.7801×10^{-5}	6.3418×10^{-5}	6.2714×10^{-5}	6.1511×10^{-5}	5.7747×10^{-5}	5.2838×10^{-5}	5.1388×10^{-5}	5.0550×10^{-5}	5.0449×10^{-5}	5.0396×10^{-5}
s_3	0.0033	0.0045	0.0061	0.0099	0.0101	0.0104	0.0114	0.0127	0.0131	0.0133	0.0133	0.0133
s_4	0.1156	0.1590	0.2142	0.3502	0.3568	0.3680	0.4028	0.4476	0.4607	0.4682	0.4691	0.4696
s_5	1.1889×10^{-5}	1.6355×10^{-5}	2.2029×10^{-5}	3.6018×10^{-5}	3.6693×10^{-5}	3.7845×10^{-5}	4.1426×10^{-5}	4.6035×10^{-5}	4.7380×10^{-5}	4.8155×10^{-5}	4.8248×10^{-5}	4.8297×10^{-5}
s_6	0.0033	0.0045	0.0061	0.0099	0.0101	0.0104	0.0114	0.0127	0.0131	0.0133	0.0133	0.0133
s_7	0.0004	0.0009	0.0017	0.0056	0.0058	0.0063	0.0081	0.0110	0.0120	0.0126	0.0127	0.0127
s_8	4.3083×10^{-8}	8.6069×10^{-8}	1.6813×10^{-7}	5.5587×10^{-7}	5.8367×10^{-7}	6.3359×10^{-7}	8.1107×10^{-7}	1.0997×10^{-6}	1.1995×10^{-6}	1.2608×10^{-6}	1.2683×10^{-6}	1.2723×10^{-6}
s_9	1.2279×10^{-5}	2.4530×10^{-5}	4.7917×10^{-5}	1.5843×10^{-4}	1.6635×10^{-4}	1.8058×10^{-4}	2.3116×10^{-4}	3.1342×10^{-4}	3.4188×10^{-4}	3.5934×10^{-4}	3.6149×10^{-4}	3.6263×10^{-4}
s_{10}	1.5841×10^{-6}	4.5960×10^{-6}	1.3020×10^{-5}	8.7049×10^{-5}	9.4207×10^{-5}	1.0763×10^{-4}	1.6113×10^{-4}	2.6654×10^{-4}	3.0815×10^{-4}	3.3496×10^{-4}	3.3831×10^{-4}	3.4011×10^{-4}
s_{11}	1.5843×10^{-10}	4.5964×10^{-10}	1.3021×10^{-9}	8.7057×10^{-9}	9.4217×10^{-9}	1.0764×10^{-8}	1.6115×10^{-8}	2.6657×10^{-8}	3.0818×10^{-8}	3.3499×10^{-8}	3.3835×10^{-8}	3.4014×10^{-8}
s_{12}	4.5936×10^{-8}	1.3327×10^{-7}	3.7754×10^{-7}	2.5242×10^{-6}	2.7318×10^{-6}	3.1211×10^{-6}	4.6725×10^{-6}	7.7292×10^{-6}	8.9357×10^{-6}	9.7130×10^{-6}	9.8104×10^{-6}	9.8624×10^{-6}
s_{13}	5.2411×10^{-9}	2.2083×10^{-8}	9.0723×10^{-8}	1.2266×10^{-6}	1.3682×10^{-6}	1.6453×10^{-6}	2.8805×10^{-6}	5.8133×10^{-6}	7.1231×10^{-6}	8.0072×10^{-6}	8.1201×10^{-6}	8.1806×10^{-6}
s_{14}	5.2416×10^{-13}	2.2086×10^{-12}	9.0732×10^{-12}	1.2267×10^{-10}	1.3684×10^{-10}	1.6454×10^{-10}	2.8808×10^{-10}	5.8139×10^{-10}	7.1238×10^{-10}	8.0080×10^{-10}	8.1209×10^{-10}	8.1814×10^{-10}
s_{15}	1.7185×10^{-10}	7.2408×10^{-10}	2.9746×10^{-9}	4.0218×10^{-8}	4.4862×10^{-8}	5.3946×10^{-8}	9.4446×10^{-8}	1.9061×10^{-7}	2.3355×10^{-7}	2.6254×10^{-7}	2.6624×10^{-7}	2.6823×10^{-7}

Table 6.18: The System Operation Probabilities for the $12 + \bar{P}$ Scheme.

Locations $[\bar{N}] = \{1, 2, \ldots, 12\}$	$12 + 0$	$12 + 1$	$12 + 2$	$12 + 3$	$12 + 4$
La Paz, B.C.	0.9962	0.9995	0.9999	0.9999	0.9999
Torreon	0.9945	0.9990	0.9999	0.9999	0.9999
Cd. Juarez	0.9920	0.9982	0.9999	0.9999	0.9999
Merida	0.9840	0.9941	0.9998	0.9999	0.9999
Monterrey	0.9835	0.9938	0.9998	0.9999	0.9999
Tijuana	0.9826	0.9933	0.9998	0.9999	0.9999
Queretaro	0.9797	0.9914	0.9997	0.9999	0.9999
Cancun	0.9752	0.9883	0.9996	0.9999	0.9999
Oaxaca	0.9738	0.9872	0.9996	0.9999	0.9999
La Habana	0.9729	0.9866	0.9995	0.9999	0.9999
Tegucigalpa	0.9728	0.9865	0.9995	0.9999	0.9999
Tuxtla, Gtz.	0.9727	0.9865	0.9995	0.9999	0.9999
Operation Probability, [%]	80.03%	90.82%	99.66%	99.90%	99.91%

Table 6.19: The Stationary Distribution of Each NGW for the $16 + \bar{P}$ Scheme.

States	N_1	N_2	N_3	N_4	N_5	N_6	N_7	N_8	N_9	N_{10}	N_{11}	N_{12}	N_{13}	N_{14}	N_{15}	N_{16}
s_1	0.8942	0.8532	0.7999	0.6624	0.6555	0.6437	0.6064	0.5570	0.5423	0.5337	0.5327	0.5322	0.5283	0.5202	0.5158	0.4842
s_2	8.9761×10^{-5}	8.5790×10^{-5}	8.0635×10^{-5}	6.7323×10^{-5}	6.6656×10^{-5}	6.5511×10^{-5}	6.1898×10^{-5}	5.7118×10^{-5}	5.5691×10^{-5}	5.4863×10^{-5}	5.4763×10^{-5}	5.4710×10^{-5}	5.4340×10^{-5}	5.3550×10^{-5}	5.3123×10^{-5}	5.0063×10^{-5}
s_3	0.0033	0.0046	0.0063	0.0106	0.0108	0.0111	0.0123	0.0137	0.0142	0.0144	0.0145	0.0145	0.0146	0.0148	0.0150	0.0159
s_4	0.0987	0.1367	0.1859	0.3114	0.3176	0.3282	0.3616	0.4052	0.4181	0.4256	0.4265	0.4269	0.4303	0.4373	0.4412	0.4683
s_5	1.0203×10^{-5}	1.4138×10^{-5}	1.9224×10^{-5}	3.2194×10^{-5}	3.2837×10^{-5}	3.3937×10^{-5}	3.7387×10^{-5}	4.1901×10^{-5}	4.3234×10^{-5}	4.4005×10^{-5}	4.4098×10^{-5}	4.4147×10^{-5}	4.4490×10^{-5}	4.5222×10^{-5}	4.5616×10^{-5}	4.8417×10^{-5}
s_6	0.0033	0.0046	0.0063	0.0106	0.0108	0.0111	0.0123	0.0137	0.0142	0.0144	0.0145	0.0145	0.0146	0.0148	0.0150	0.0159
s_7	0.0004	0.0007	0.0014	0.0048	0.0050	0.0054	0.0070	0.0096	0.0105	0.0110	0.0111	0.0111	0.0114	0.0119	0.0123	0.0147
s_8	3.5367×10^{-8}	7.1172×10^{-8}	1.4034×10^{-7}	4.7527×10^{-7}	4.9964×10^{-7}	5.4348×10^{-7}	7.0021×10^{-7}	9.5743×10^{-7}	1.0470×10^{-6}	1.1021×10^{-6}	1.1089×10^{-6}	1.1125×10^{-6}	1.1380×10^{-6}	1.1942×10^{-6}	1.2255×10^{-6}	1.4708×10^{-6}
s_9	1.2515×10^{-5}	2.5186×10^{-5}	4.9662×10^{-5}	1.6818×10^{-4}	1.7681×10^{-4}	1.9232×10^{-4}	2.4778×10^{-4}	3.3880×10^{-4}	3.7051×10^{-4}	3.9000×10^{-4}	3.9240×10^{-4}	3.9367×10^{-4}	4.0272×10^{-4}	4.2259×10^{-4}	4.3366×10^{-4}	5.2046×10^{-4}
s_{10}	1.2968×10^{-6}	3.7901×10^{-6}	1.0838×10^{-5}	7.4224×10^{-5}	8.0424×10^{-5}	9.2073×10^{-5}	1.3873×10^{-4}	2.3143×10^{-4}	2.6823×10^{-4}	2.9199×10^{-4}	2.9497×10^{-4}	2.9656×10^{-4}	3.0795×10^{-4}	3.3361×10^{-4}	3.4829×10^{-4}	4.7264×10^{-4}
s_{11}	1.2970×10^{-10}	3.7905×10^{-10}	1.0839×10^{-9}	7.4231×10^{-9}	8.0432×10^{-9}	9.2082×10^{-9}	1.3874×10^{-8}	2.3145×10^{-8}	2.6826×10^{-8}	2.9202×10^{-8}	2.9500×10^{-8}	2.9659×10^{-8}	3.0798×10^{-8}	3.3365×10^{-8}	3.4832×10^{-8}	4.7268×10^{-8}
s_{12}	4.6819×10^{-8}	1.3683×10^{-7}	3.9129×10^{-7}	2.6797×10^{-6}	2.9035×10^{-6}	3.3241×10^{-6}	5.0084×10^{-6}	8.3553×10^{-6}	9.6840×10^{-6}	1.0542×10^{-5}	1.0649×10^{-5}	1.0707×10^{-5}	1.1118×10^{-5}	1.2044×10^{-5}	1.2574×10^{-5}	1.7063×10^{-5}
s_{13}	4.5534×10^{-9}	1.9327×10^{-8}	8.0148×10^{-8}	1.1100×10^{-6}	1.2396×10^{-6}	1.4936×10^{-6}	2.6318×10^{-6}	5.3567×10^{-6}	6.5801×10^{-6}	7.4077×10^{-6}	7.5134×10^{-6}	7.5701×10^{-6}	7.9793×10^{-6}	8.9241×10^{-6}	9.4781×10^{-6}	1.4543×10^{-5}
s_{14}	4.5539×10^{-13}	1.9329×10^{-12}	8.0157×10^{-12}	1.1101×10^{-10}	1.2397×10^{-10}	1.4938×10^{-10}	2.6321×10^{-10}	5.3572×10^{-10}	6.5808×10^{-10}	7.4085×10^{-10}	7.5142×10^{-10}	7.5709×10^{-10}	7.9801×10^{-10}	8.9250×10^{-10}	9.4791×10^{-10}	1.4545×10^{-9}
s_{15}	1.7515×10^{-10}	7.4341×10^{-10}	3.0830×10^{-9}	4.2695×10^{-8}	4.7682×10^{-8}	5.7453×10^{-8}	1.0124×10^{-7}	2.0605×10^{-7}	2.5311×10^{-7}	2.8494×10^{-7}	2.8901×10^{-7}	2.9119×10^{-7}	3.0693×10^{-7}	3.4327×10^{-7}	3.6458×10^{-7}	5.5942×10^{-7}

Table 6.20: The System Operation Probabilities for the $16 + \bar{P}$ Scheme.

Locations $[\bar{N}] = \{1, 2, \ldots, 16\}$	$16 + 0$	$16 + 1$	$16 + 2$	$16 + 3$	$16 + 4$
La Paz, B.C.	0.9962	0.9995	0.9999	0.9999	0.9999
Torreon	0.9945	0.9992	0.9999	0.9999	0.9999
Cd. Juarez	0.9920	0.9984	0.9999	0.9999	0.9999
Merida	0.9840	0.9949	0.9998	0.9999	0.9999
Monterrey	0.9835	0.9946	0.9998	0.9999	0.9999
Tijuana	0.9826	0.9942	0.9998	0.9999	0.9999
Queretaro	0.9797	0.9925	0.9998	0.9999	0.9999
Cancun	0.9752	0.9897	0.9997	0.9999	0.9999
Oaxaca	0.9738	0.9888	0.9996	0.9999	0.9999
La Habana	0.9729	0.9882	0.9996	0.9999	0.9999
Tegucigalpa	0.9728	0.9881	0.9996	0.9999	0.9999
Tuxtla, Gtz.	0.9727	0.9881	0.9996	0.9999	0.9999
Guadalajara	0.9723	0.9878	0.9996	0.9999	0.9999
Kingston	0.9714	0.9872	0.9995	0.9999	0.9999
Veracruz	0.9709	0.9868	0.9995	0.9999	0.9999
St. Domingo	0.9671	0.9842	0.9994	0.9999	0.9999
Operation Probability, [%]	70.97%	87.06%	99.50%	99.85%	99.91%

Meanwhile, the Markov chain is irreducible when the state s_i of the Markov chain is accessible from another state s_j by a finite sequence of the transition of s_i to s_j with positive probability [83].

In summary, Figure 6.6 depicts the obtained schemes $\bar{N} + \bar{P}$ in terms of system outage probability, P_{out}. Here, it is possible to appreciate the best schemes that outperform the reference 1×10^{-3}, which are: $4 + 2$, $8 + 3$, $12 + 3$, and $16 + 4$.
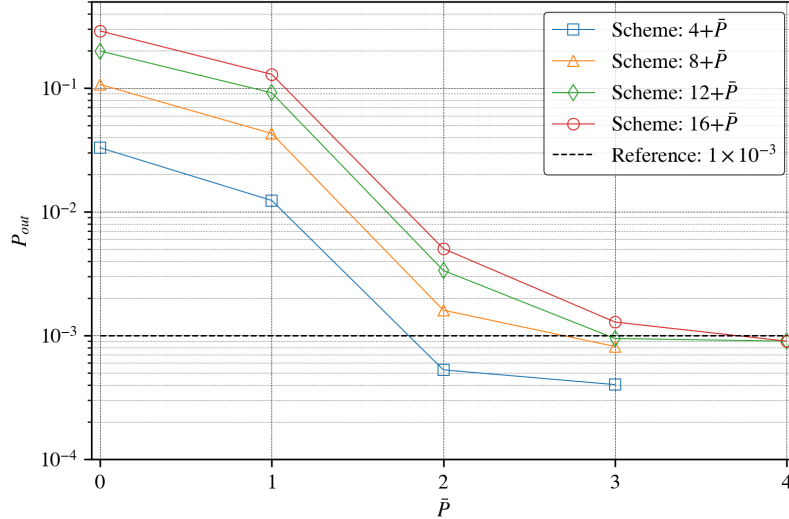
Figure 6.6: Performance of the $\bar{N} + \bar{P}$ schemes, as a function of system outage probability, P_{out}, and the number of $\bar{P}$.

6.5 Discussions

There are remarkable differences between the availabilities and probabilities of each GW. For instance, the sorted list of Table 6.3 is different in comparison with the sorted list of Table 6.12. Naturally, the difference lies in the methods to define the availability (deterministic approach) and probability (probabilistic approach) at each GW. Nevertheless, this difference is not a big problem as the analysis of each feeder uplink was rigorous, following the steps aforementioned of both methods. Therefore, both sorted lists are theoretically reliable according to their mathematical nature.

In both smart predictive and Markov chain $1 + \bar{P}$ strategy methods, the first PGW backs up the most of feeder uplink outages of NGWs. For this reason, the mechanism has a direct approach when an NGW feeder uplink is in an outage in terms of assignation, backing up immediately the affected NGW with the first PGW. On the other hand, if the first PGW has its feeder uplink in an outage or busy with another NGW, then the mechanism picks out the next available PGW. Motivated by this, the method encourages to avoid correlated rain in two or more GWs at the same time by a separation between them based on the correlation coefficient ρ_a obtained

from ITU-R P.1815. As a result, all GWs are separated by a distance > 80 km, reducing the risk of simultaneous rain in two or more sites at the same time, and increasing the chances of the first PGW is available in most of the time. Moreover, it was necessary to assume spatially independent and identically distributed (i.i.d) feeder uplinks.

The main aim of this study is to define the most suitable ground network to manage a satellite system of 1 Tb/s and beyond. According to Table 6.2, 12 NGWs are needed to manage a satellite system of about 1 Tb/s. In a sense, for capacities of 1 Tb/s and beyond, we have coined the term Ultra High Throughput Satellite Systems (UHTS). To be specific, the ground networks of 4 and 8 NGWs are for HTS systems, whereas the ground networks of 12 and 16 NGWs are for UHTS systems.

In this context, these 4 configurations of NGWs were tested by both switching strategies to determine their effectiveness, as deterministically (smart predictive method) as probabilistically (Markov chain method). Figure 6.7 shows the results of both proposed methods in this study to find $\bar{N} + \bar{P}$ schemes, in addition to Gharanjik's method [25]. The results obtained from the smart predictive method were highly superior compared with the Markov Chain method and the Gharanjik's method. That is, the smart predictive method gave the following results: $4+1$, $8+1$, $12+1$, and $16+2$, whereas the Markov Chain method: $4+2$, $8+3$, $12+3$, and $16+4$. Gharanjik's method provided linear results, that is, $\bar{N}/\bar{P} = 4$, so that the scheme results are the following: $4+1$, $8+2$, $12+3$, and $16+4$.
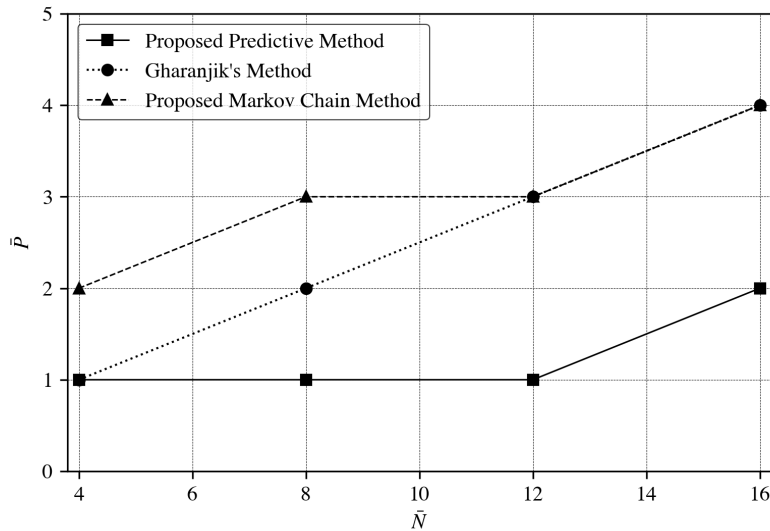
Figure 6.7: $\bar{N} + \bar{P}$ configuration schemes obtained from the three aforementioned methods.

The efficiency of the smart predictive method is, on average, 41.67% and 58.34% better than Gharanjik's model and Markov chain model, respectively. Therefore, the $1 + \bar{P}$ switching strategy based on the smart method for forecasting rain attenuation and CNIR at each GW is highly efficient and reliable, optimizing the ground segment network as much as possible. Indeed, for a 1 Tb/s UHTS, the optimized ground

network is $12 + 1$, rather than $12 + 3$ obtained from Gharanjik's method, reducing the network complexity and generating economic savings on the ground segment.

Despite the ground network could be not optimized by the Markov chain method, each stationary distribution obtained from this method gave us a panorama on the switching probability between the affected NGW and the first PGW. No doubt, this parameter could help to get more information about the ground network behavior when there is a switching between an NGW and PGW under different weather conditions. In other words, the switching probability could be determinant to define the most suitable technology to implement on the ground network, that is, the network infrastructure to communicate GWs to each other.

6.6 Contributions of the Research

The proposed methods and found results in this chapter will be submitted to a IEEE Transactions on Reliability Journal to be reviewed and published later. Furthermore, the previous study was exposed to a specialized conference: *"2020 IEEE 11th Latin American Symposium on Circuits and Systems, LASCAS 2020,"* at San Jose, Costa Rica.

- Andres Cornejo, Salvador Landeros-Ayala, Jose M. Matias, and Ramon Martinez. Applying Learning Methods to Optimize the Ground Segment for HTS Systems. *2020 IEEE 11th Lat. Am. Symp. Circuits Syst. LASCAS 2020*, pages 1–4, 2020

Chapter 7

Conclusions, Future Work, and Contributions

7.1 Conclusions

In this thesis, we designed, allocated, and optimized the ground segment by using novel methods and procedures with excellent results. The obtained feeder link was designed in the Q/V band, whose performance was determined by numerical evaluations. Further, the designed satellite antenna was based on an offset-parabolic-reflector antenna to evaluate the interferences that could influence the satellite links, directly or indirectly. As a result, we found excellent levels of the carrier-to-noise and interference (CNIR) of each analyzed feeder uplink in clear-sky conditions, which reached out to the uplink expectations for our system. However, for a more realistic scenario, each feeder uplink was evaluated by applying a dynamic rain attenuation based on the ITU Recommendation P.1853, defining the upper and lower limits of feeder uplinks operation under the rain conditions.

For this purpose, we have successfully developed a method to generate, train, and validate rain-attenuation prediction models based on LSTM networks. Two Experiments were carried out to determine the best models, where Experiment 2 was found to be the most complete and accurate. In this sense, Machine Learning methods can be beneficial for solving a specific problem whether the adaptation is correct. In this case, deep learning networks based on LSTM regression models were adequately adapted to our study, thereby, they were able to predict rain attenuation events more accurately. In order to validate our proposal, this method was compared with other predictive methods, where our proposal obtained a higher accuracy and a better performance.

Furthermore, real rain-attenuation data were difficult to obtain due to the lack of historical database, however, ITU Recommendation (ITU-R P.1853) was able to compute artificial rain-attenuation, providing a plethora of data. Indeed, a lot of data is required to train LSTM networks due to they are notably ubiquitous. Here, it was possible to split data into both training and validation subsets because each rain attenuation time series had hundreds of thousands of samples.

The processing of data was essential for obtaining good results as the answer lies in the data. For this reason, subsets were carefully processed in terms of normalization, partitioning, training, and validation. Thus, the model accuracy, on average, is about 87.83%, where the best model reaches out to the accuracy of 92.24%. All evaluated GW-sites indicate good performance, giving solid predictions of rain attenuation.

In this context, the found results are successful to determine in advance how the feeder uplink will be affected by weather impairments. This certainly leads to better decision-making under rain-attenuation events, thereby, mechanisms such as ULPC, traffic switching between GWs with extra resources, and satellite-link switching towards backup gateway stations, can be improved by CNIR predictions obtained from this proposal in order to assure high availability on satellite links.

To be precise, we focus on the optimization of the ground network by the switching strategies of traffic between GWs. In this context, two switching strategy mechanisms were proposed by a smart-predictive-method based on the deep learning model and a Markov chain method. As a result, the proposed smart-predictive method reaches a superior efficiency, on average, of 41.67% vs Gharanjik's method, and 58.34% vs the proposed Markov chain method, optimizing the ground network with excellent performance. For instance, for a UHTS system of 1 Tb/s, Gharanjik's method provided a ground network scheme of $12 + 3$ to operate above the required network availability of 99.9%. Meanwhile, the proposed smart-predictive method gave, as a result, an optimized scheme of $12 + 1$, which was 66.67% more efficient than the previous configuration scheme. In other words, the success of the smart-predictive method lies in the ability to detect, in advance, a feeder uplink in outage due to the rain, anticipating the switching between the affected NGW and an available PGW. To sum up, this prediction method leads to optimizing the ground segment by the smart gateway diversity, reducing the number of gateway stations, that is, the network complexity.

7.2   Future Work

As a result of this thesis, some interesting topics have been branched for future research work in both Machine Learning and Satellite Communication fields, which comprise,

- Although the artificial data were useful to develop this proposal, rain attenuation from a historical database could help to tune up and to improve models. Further studies are necessary to determine much more accurate models by employing real and artificial data together.

- By using Cloud Computing, the prediction method could be accessed from any GW station, to be specific, the prediction method could be implemented by software as a service (SaaS). No doubt that the prediction method as a cloud service will guarantee to manage data in real-time, in addition to providing flexibility and security.

- Finally, the stationary distributions obtained from the Markov chain method provide worth information (the switching rate) to define the best infrastructure capable of transferring data traffic between GWs, reducing latency and delays. In this context, the best option is the network infrastructure based on optical fiber, but it is not the cheapest choice. Hence, other options could be considered to simplify the terrestrial network and reduce costs by the analysis of the switching probability and rate, e.g., microwave links.

7.3 Contributions and Production

The research results of each topic of this thesis have been published or have been submitted for publications in journals and conference proceedings, as indicated in the following. It is worth to mention that the main ideas, the problem formulations, the analysis, simulations, and numerical assessments for all publications are contributions of the author of this thesis.

Journals

- [103] Andres Cornejo, Salvador Landeros-Ayala, Ramon Martinez, and Jose M Matias. Analysis to Quantify and Optimize Spot Beams for a High Throughput Satellite in Ka and Q/V Bands. *IEEE Lat. Am. Trans.*, 17(02):219–227, feb 2019

- [104] Andres Cornejo, Salvador Landeros-Ayala, Ramon Martínez Rodríguez-Osorio, and Jose M Matias. A method for designing an offset-parabolic-reflector antenna for a ultra-high throughput satellite. In *Rev. Tecnol. e Inf.*, volume 16, pages 84–87, Lima, Peru, 2018. Universidad Inca Garcilaso de la Vega

- [105] Andres Cornejo, Salvador Landeros-Ayala, Ramon Martinez-Rodriguez, and Jose M Matias. Interference Evaluations in Frequency Reuse by Using Offset- Parabolic-Reflector Antennas for a UHTS System. *Int. J. Eng. Sci.*, 7(8):34–45, 2018

- Andres Cornejo, Salvador Landeros-Ayala, Jose M. Matias, Flor Ortiz-Gomez, Ramon Martinez, and Miguel Salas-Natera. Method of Rain Attenuation Prediction Based On Long-Short Term Memory Network. *In Review.*, 1(1):1–35, 2020

- Andres Cornejo, Salvador Landeros-Ayala, and Jose Maria Matias. Optimization of the Ground Network Segment by Implementing Machine Learning. *To be Submitted*, 1(1):30, 2020

Conferences

- [106] Andres Cornejo, Salvador Landeros-Ayala, Ramon Martinez Rodriguez-Osorio, and Jose Maria Matias. Optimization of the Ground Segment for an UHTS System through Neural Networks. In *XXXIII Simp.*

Nac. la Unión Científica Int. Radio (URSI 2018), pages 1–5, Granada, Spain, 2018

- [107] Andres Cornejo, Salvador Landeros-Ayala, Jose M. Matias, and Ramon Martinez. Applying Learning Methods to Optimize the Ground Segment for HTS Systems. *2020 IEEE 11th Lat. Am. Symp. Circuits Syst. LASCAS 2020*, pages 1–4, 2020

- [108] Andres Cornejo, Flor Ortiz-Gomez, Jose M. Matias, Ramon Martinez, and Miguel Salas-Natera. Quantum Cryptography for Satellite Communication Systems. In *Congr. Nac. Act. Espac. 2020-Agencia Espac. Mex.*, Mexico City, 2020

Finally, all code scripts employed in this thesis will remain in the Github repository permanently, https://github.com/KunaCornejo. All code scripts were developed by the author of this thesis using Python® and Matlab®, except for the ITU-R P.1853 script, which was written in Matlab by ONERA®, French Aerospace Lab.

Appendix A

List of Geographic Coordinates for Gateway (GW) Locations

A.1 List of Geographic Coordinates for Gateway (GW) Locations, Chapter 3

A.2 List of Geographic Coordinates for Gateway (GW) Locations, Chapter 5

The clear sky carrier-to-noise ratio (γ_{cs}) for each feeder uplink was calculated by using the geographic coordinates regarding its location, geostationary satellite position at 92.0° West, roll-off of 5%, and the frequency band at 50 GHz (V-band). Furthermore, the transmitter power of each GW is about 16.0 W, and the antenna diameter of 5.0 m, as can be seen in Chapter 3.

A.3 Distance Matrix Between Pairs of Locations, Chapter 6

The distance between a pair of gateway locations was calculated by their geographic coordinates. For this purpose, the geographic coordinates for each GW location were provided by Table A.2. Finally, each computed value was stored in the distance matrix **D**.

Table A.1: List of Geographic Coordinates for GW Locations, Chapter 3

Location	Country	Latitude [deg]	Longitude [deg]	Height (a.m.s.l.) [m]
Buenos Aires	Argentina	-34.611758	-58.430232	25.0
Santiago	Chile	-33.458205	-70.666972	567.0
Montevideo	Uruguay	-34.81721	-56.188972	43.0
Asuncion	Paraguay	-25.298939	-57.636595	43.0
La Paz	Bolivia	-16.503502	-68.124903	3625.0
Sao Paulo	Brazil	-23.572845	-46.623028	760.0
Lima	Peru	-12.052542	-77.043969	154.0
Guayaquil	Ecuador	-2.185092	-79.908501	4.0
Quito	Ecuador	-0.178182	-78.482904	2700.0
Rio de Janeiro	Brazil	-22.904847	-43.219689	11.0
Bogota	Colombia	4.696189	-74.077603	2640.0
Caracas	Venezuela	10.474799	-66.905474	900.0
Panama	Panama	9.010642	-79.509318	2.0
San Jose	Costa Rica	9.924622	-84.094463	1300.0
Tegucigalpa	Guatemala	14.069427	-87.201883	1000.0
Mexico City	Mexico	19.336688	-99.165822	2250.0
Monterrey	Mexico	25.707672	-100.334175	530.0
Guadalajara	Mexico	20.65853	-103.347001	1556.0
Cordoba	Argentina	-31.408778	-64.196749	390.0
Iquique	Chile	-20.232089	-70.134301	1.0
Manaus	Brazil	-3.11014	-60.000065	92.0
Belo Horizonte	Brazil	-19.925298	-43.940535	760.0
Tijuana	Mexico	32.505354	-116.971508	31.0
Arequipa	Peru	-16.405163	-71.541072	2335.0
Cuzco	Peru	-13.527847	-71.964484	3399.0
Mar del Plata	Argentina	-38.030257	-57.604656	38.0
Rosario	Argentina	-32.953004	-60.687002	25.0
Porto Alegre	Brazil	-30.079685	-51.231157	10.0
Valdivia	Chile	-39.838558	-73.23594	14.0
Cali	Colombia	3.4074	-76.533906	1018.0
Cartagena	Colombia	10.401403	-75.51452	2.0
Pto. Concordia	Colombia	1.252249	-70.232856	201.0
Maracaibo	Venezuela	10.6808	-71.635416	15.0
Barinas	Venezuela	8.603336	-70.229713	200.0
La Habana	Cuba	23.104927	-82.286028	59.0
St. Domingo	Dominican. Rep.	18.48892	-69.935325	14.0
Chiclayo	Peru	-6.784283	-79.858654	27.0
San Salvador	El Salvador	13.697313	-89.219673	658.0
San Juan	Puerto Rico	18.401754	-66.036714	7.9
Brasilia	Brazil	-15.811467	-47.874582	1172.0
Ushuaia	Argentina	-54.817684	-68.329799	58.0
Recife	Brazil	-8.043475	-34.955255	58.0
Pto. Baquerizo	Ecuador	-0.907203	-89.604353	2.0

Table A.2: List of Geographic Coordinates for GW Locations, Chapter 5

i	Location	Country	Latitude [deg]	Longitude [deg]	Height (a.m.s.l.) [m]	γ_{cs} [dB]
1	Panama	Panama	9.010642	-79.509318	2.0	32.44
2	San Jose	Costa Rica	9.924622	-84.094463	1300.0	32.46
3	Tegucigalpa	Guatemala	14.069427	-87.201883	1000.0	32.45
4	Mexico City	Mexico	19.336688	-99.165822	2250.0	32.39
5	Monterrey	Mexico	25.707672	-100.334175	530.0	32.31
6	Guadalajara	Mexico	20.65853	-103.347001	1566.0	32.36
7	Tijuana	Mexico	32.505354	-116.971508	31.0	32.09
8	La Habana	Cuba	23.104927	-82.286028	59.0	32.34
9	St. Domingo	Dominican Rep.	18.48892	-69.935325	14.0	32.29
10	San Salvador	El Salvador	13.697313	-89.219673	658.0	32.45
11	San Juan	Puerto Rico	18.401754	-66.036714	7.9	32.24
12	Torreon	Mexico	25.560636	-103.374418	1120.0	32.30
13	La Paz, B.C.	Mexico	24.129867	-110.292943	27.0	32.27
14	Veracruz	Mexico	19.170373	-96.181209	10.0	32.40
15	Cancun	Mexico	21.12228	-86.840371	11.0	32.38
16	Queretaro	Mexico	20.614965	-100.411033	2017.0	32.37
17	Tuxtla, Gtz.	Mexico	16.705306	-93.173516	522.0	32.43
18	Cd. Juarez	Mexico	31.761652	-106.526185	1137.0	32.19
19	San Pedro Sula	Honduras	15.517251	-87.992356	83.0	32.43
20	Belmopan	Belize	17.265146	-88.768523	76.0	32.42
21	Kingston	Jamaica	18.013036	-76.811471	9.0	32.36
22	Merida	Mexico	20.970434	-89.608201	10.0	32.39
23	Pto. Cabezas	Nicaragua	14.047875	-83.407334	7.0	32.43
24	Oaxaca	Mexico	17.113126	-96.74277	1555.0	32.42

$$D =$$

	Panama	San Jose	Tegucigalpa	Mexico City	Monterrey	Guadalajara	Tijuana	La Habana	St. Domingo	San Salvador	San Juan	Torreon
Panama	–	513.06	1009.08	2406.67	2877.85	2865.14	4649.56	1594.88	1475.49	1179.59	1789.57	3121.00
San Jose	513.06	–	571.48	1927.83	2451.35	2381.31	4201.78	1478.14	1797.36	697.87	2160.74	2674.78
Tegucigalpa	1009.08	571.48	–	1401.67	1884.22	1861.93	3645.40	1130.09	1906.28	221.71	2308.73	2116.46
Mexico City	2406.67	1927.83	1401.67	–	718.50	460.93	2299.18	1797.89	3072.64	1231.31	3482.09	815.93
Monterrey	2877.85	2451.35	1884.22	718.50	–	640.28	1781.48	1848.77	3224.94	1769.17	3615.80	305.22
Guadalajara	2865.14	2381.31	1861.93	460.93	640.28	–	1886.18	2188.17	3502.81	1687.32	3909.72	545.10
Tijuana	4649.56	4201.78	3645.40	2299.18	1781.48	1886.18	–	3550.15	4927.56	3506.11	5296.02	1528.98
La Habana	1594.88	1478.14	1130.09	1797.89	1848.77	2188.17	3550.15	–	1381.90	1275.85	1767.36	2151.68
St. Domingo	1475.49	1797.36	1906.28	3072.64	3224.94	3502.81	4927.56	1381.90	–	2126.61	411.34	3525.35
San Salvador	1179.59	697.87	221.71	1231.31	1769.17	1687.32	3506.11	1275.85	2126.61	–	2529.85	1981.34
San Juan	1789.57	2160.74	2308.73	3482.09	3615.80	3909.72	5296.02	1767.36	411.34	2529.85	–	3918.01
Torreon	3121.00	2674.78	2116.46	815.93	305.22	545.10	1528.98	2151.68	3525.35	1981.34	3918.01	–
La Paz, B.C.	3672.73	3192.28	2666.25	1266.22	1019.21	811.55	1137.19	2850.95	4213.30	2497.05	4611.56	715.90
Veracruz	2120.80	1656.64	1111.83	313.85	842.78	767.13	2546.62	1505.23	2760.68	959.71	3170.58	1025.22
Cancun	1559.00	1279.27	785.18	1300.86	1467.24	1714.81	3232.37	518.34	1791.70	863.29	2196.29	1757.18
Queretaro	2586.31	2112.85	1578.56	192.71	566.34	305.55	2107.17	1889.58	3197.52	1415.25	3604.71	627.87
Tuxtla, Gtz.	1709.37	1237.81	704.03	697.83	1245.52	1157.89	2966.55	1341.57	2469.34	540.20	2880.52	1444.07
Cd. Juarez	3763.32	3350.49	2780.94	1565.34	903.84	1274.48	986.61	2571.28	3944.69	2672.36	4310.31	754.87
San Pedro Sula	1171.31	751.87	182.04	1258.76	1710.82	1719.60	3478.37	1034.25	1947.37	241.64	2355.58	1949.70
Belmopan	1358.53	959.69	392.93	1121.34	1519.49	1578.12	3294.90	937.43	1996.79	399.66	2407.98	1769.03
Kingston	1042.55	1193.84	1193.47	2357.80	2569.07	2796.58	4316.74	803.19	728.01	1410.78	1138.77	2862.10
Merida	1714.58	1362.52	808.60	1013.91	1214.53	1427.97	2992.64	791.01	2076.14	809.78	2482.04	1494.98
Pto. Cabezas	702.82	464.53	409.30	1777.34	2190.03	2237.96	3968.92	1013.99	1519.79	628.64	1915.66	2444.76
Oaxaca	2070.79	1582.90	1076.23	355.83	1025.26	798.71	2655.00	1648.70	2839.71	891.27	3251.04	1163.09

$$D =$$

	La Paz, B.C.	Veracruz	Cancun	Queretaro	Tuxtla, Gtz.	Cd. Juarez	San Pedro Sula	Belmopan	Kingston	Merida	Pto. Cabezas	Oaxaca
Panama	3672.73	2120.80	1559.00	2586.31	1709.37	3763.32	1171.31	1358.53	1042.55	1714.58	702.82	2070.79
San Jose	3192.28	1656.64	1279.27	2112.85	1237.81	3350.49	751.87	959.69	1193.84	1362.52	464.53	1582.90
Tegucigalpa	2666.25	1111.83	785.18	1578.56	704.03	2780.94	182.04	392.93	1193.47	808.60	409.30	1076.23
Mexico City	1266.22	313.85	1300.86	192.71	697.83	1565.34	1258.76	1121.34	2357.80	1013.91	1777.34	355.83
Monterrey	1019.21	842.78	1467.24	566.34	1245.52	903.84	1710.82	1519.49	2569.07	1214.53	2190.03	1025.26
Guadalajara	811.55	767.13	1714.81	305.55	1157.89	1274.48	1719.60	1578.12	2796.58	1427.97	2237.96	798.71
Tijuana	1137.19	2546.62	3232.37	2107.17	2966.55	986.61	3478.37	3294.90	4316.74	2992.64	3968.92	2655.00
La Habana	2850.95	1505.23	518.34	1889.58	1341.57	2571.28	1034.25	937.43	803.19	791.01	1013.99	1648.70
St. Domingo	4213.30	2760.68	1791.70	3197.52	2469.34	3944.69	1947.37	1996.79	728.01	2076.14	1519.79	2839.71
San Salvador	2497.05	959.71	863.29	1415.25	540.20	2672.36	241.64	399.66	1410.78	809.78	628.64	891.27
San Juan	4611.56	3170.58	2196.29	3604.71	2880.52	4310.31	2355.58	2407.98	1138.77	2482.04	1915.66	3251.04
Torreon	715.90	1025.22	1757.18	627.87	1444.07	754.87	1949.70	1769.03	2862.10	1494.98	2444.76	1163.09
La Paz, B.C.	–	1558.14	2427.31	1088.29	1963.42	925.56	2517.27	2362.09	3531.16	2150.95	3032.19	1610.17
Veracruz	1558.14	–	998.78	470.51	419.94	1740.97	959.17	811.00	2044.43	715.00	1474.76	236.33
Cancun	2427.31	998.78	–	1410.70	827.46	2283.47	634.99	474.27	1105.86	287.73	866.60	1131.47
Queretaro	1088.29	470.51	1410.70	–	877.48	1380.75	1429.21	1279.46	2491.09	1123.47	1945.27	548.21
Tuxtla, Gtz.	1963.42	419.94	827.46	877.48	–	2148.85	569.01	472.55	1742.01	604.66	1087.78	382.42
Cd. Juarez	925.56	1740.97	2283.47	1380.75	2148.85	–	2604.64	2406.97	3348.59	2064.47	3066.98	1903.93
San Pedro Sula	2517.27	959.17	634.99	1429.21	569.01	2604.64	–	211.26	1222.07	629.90	519.30	950.42
Belmopan	2362.09	811.00	474.27	1279.46	472.55	2406.97	211.26	–	1269.56	421.34	676.28	847.20
Kingston	3531.16	2044.43	1105.86	2491.09	1742.01	3348.59	1222.07	1269.56	–	1380.60	831.27	2114.31
Merida	2150.95	715.00	287.73	1123.47	604.66	2064.47	629.90	421.34	1380.60	–	1012.02	863.70
Pto. Cabezas	3032.19	1474.76	866.60	1945.27	1087.78	3066.98	519.30	676.28	831.27	1012.02	–	1468.02
Oaxaca	1610.17	236.33	1131.47	548.21	382.42	1903.93	950.42	847.20	2114.31	863.70	1468.02	–

Bibliography

[1] Gerard Maral and Michel Bousquet. *Satellite Communications Systems.* John Wiley & Sons, Ltd, Chichester, UK, 5th edition, dec 2009.

[2] Rodolfo Neri and Salvador Landeros. *Comunicaciones por satélite.* Editorial Veracruzana, 1st edition, 2015.

[3] Ahmad Gharanjik. *Transmission Optimization for High Throughput Satellite Systems.* PhD thesis, Royal Institue of Technology, 2016.

[4] ITU. Radio Regulations. Technical report, International Telecommunication Union, ITU, Geneve, Switzerland, 2016.

[5] Darren Chang and Olivier de Weck. Basic Capacity Calculation Methods and Benchmarking for MF-TDMA and MF-CDMA Communication Satellites. In *21st Int. Commun. Satell. Syst. Conf. Exhib.*, pages 1–9, Reston, Virigina, apr 2003. American Institute of Aeronautics and Astronautics.

[6] EN ETSI. Digital Video Broadcasting (DVB); Second generation framing structure, channel coding and modulation systems for Broadcasting, Interactive Services, News Gathering and other broadband satellite applications; Part 2: DVB-S2 Extensions (DVB-S2X). Technical report, European Telecommunications Standards Institute (ETSI), France, 2014.

[7] EN ETSI. Digital Video Broadcasting (DVB); Second Generation DVB Interactive Satellite System (DVB-RCS2); Part 1: Overview and System Level specification. Technical report, European Telecommunications Standards Institute (ETSI), France, 2014.

[8] Barry Evans and Paul Thompson. Key issues and technologies for a Terabit/s satellite. In *28th AIAA Int. Commun. Satell. Syst. Conf.*, pages 1–11, Anaheim, CA, aug 2010. American Institute of Aeronautics and Astronautics.

[9] Sudhakar Rao, Minh Tang, and Chih Chien Hsu. Multiple beam antenna technology for satellite communications payloads. *Appl. Comput. Electromagn. Soc. J.*, 21(3):353–363, 2006.

[10] Rajeev Gopal, David Whitefield, and Steve Arnold. Technology readiness of future generation networks leveraging regenerative satellite mesh architecture -

A spaceway perspective. *Proc. - IEEE Mil. Commun. Conf. MILCOM*, pages 1–7, 2007.

[11] Hughes Inc. Hughes High-Throughput Satellite Constellation. https://www.hughes.com/technologies/hughes-high-throughput-satellite-constellation, 2019.

[12] Echostar Corporation. Brochure: Connecting The World. http://www.echostarsatelliteservices.com, 2019.

[13] Hector Fenech, Alessia Tomatis, Sonya Amos, Viphakone Soumpholphakdy, and Jose Luis Serrano-Merino. Eutelsat HTS Systems. *Int. J. Satell. Commun. Netw.*, 34(January):1–6, 2011.

[14] Paul Thompson, Barry Evans, Michel Bousquet, and Laurent Castenet. Concepts and Technologies for a Terabit/s Satellite Supporting future broadband services via satellite. *Third Int. Conf. Adv. Satell. Sp. Commun. Concepts, SPACOMM*, pages 12–19, 2011.

[15] Isabelle Dahman, Philippe Arbogast, Nicolas Jeannin, and Bouchra Benammar. Rain attenuation prediction model for satellite communications based on the Météo-France ensemble prediction system PEARP. *Nat. Hazards Earth Syst. Sci.*, 18(12):3327–3341, 2018.

[16] ITU-R Recomendation S.1557. Operational requirements and characteristics of fixed-satellite service systems operating in the 50/40 GHz bands for use in sharing studies between the fixed-satellite service and the fixed service. Technical report, International Telecommunication Union, Geneve, Switzerland, 2002.

[17] Peter Balling. Analytical high-efficiency spot-beam model for high throughput satellites. *Radioengineering*, 21(4):1078–1084, 2012.

[18] Argyrios Kyrgiazos, Barry Evans, Paul Thompson, P. Takis Mathiopoulos, and Stylianos Papaharalabos. A terabit/second satellite system for European broadband access: a feasibility study. *Int. J. Satell. Commun. Netw.*, 32(2):63–92, mar 2014.

[19] Richard Swinford and Bertrand Grau. High Throughput Satellites: Delivering future capacity needs. Technical report, Arthur D. Little, 2015.

[20] Russell Ju Fu Fang. Spatial diversity satellite communications system with error control. US Patent 4,099,121, 1978.

[21] Ahmad Gharanjik, Bhavani Shankar Mysore Rama Rao, Pantelis Daniel Arapoglou, and Björn Ottersten. Gateway switching in Q/V band satellite feeder links. *IEEE Commun. Lett.*, 17(7):1384–1387, 2013.

[22] Muhammad Muhammad, Giovanni Giambene, and Tomaso De Cola. Channel prediction and network coding for smart gateway diversity in terabit satellite networks. *2014 IEEE Glob. Commun. Conf. GLOBECOM 2014*, pages 3549–3554, 2014.

[23] Giovanni Giambene, Doanh Kim Luong, Van Anh Le, and Tomaso De Cola. Gateway handover implications on transport layer performance in terabit satellite networks. *2014 7th Adv. Satell. Multimed. Syst. Conf. 13th Signal Process. Sp. Commun. Work. ASMS/SPSC 2014*, 2014-Janua:9–16, 2014.

[24] Andra Pastrav, Tudor Palade, and Emanuel Puschita. A proposed mechanism for traffic management during gateway outage periods in high throughput satellite systems. *2015 38th Int. Conf. Telecommun. Signal Process. TSP 2015*, pages 200–204, 2015.

[25] Ahmad Gharanjik, Bhavani Shankar, Pantelis-daniel Arapoglou, and Bjorn Ottersten. Multiple Gateway Transmit Diversity in Q/V Band Feeder Links. *IEEE Trans. Commun.*, 63(3):916–926, mar 2015.

[26] Zoltán Katona, Federico Clazzer, Kevin Shortt, Simon Watts, Hans Peter Lexow, and Ratna Winduratna. Performance, cost analysis, and ground segment design of ultra high throughput multi-spot beam satellite networks applying different capacity enhancing techniques. *Int. J. Satell. Commun. Netw.*, 34(4):547–573, jul 2016.

[27] ITU-R Recommendation P.1815-1. Differential rain attenuation. Technical Report October, International Telecommunication Union, Geneve, Switzerland, 2009.

[28] ITU-R Recommendation P.618-13. Propagation data and prediction methods required for the design of Earth-space telecommunication systems. Technical Report December, International Telecommunication Union, Geneve, Switzerland, 2017.

[29] ITU-R Recomendation P.837-7. Characteristics of precipitation for propagation modelling. Technical report, International Telecommunication Union, Geneve, Switzerland, 2017.

[30] ITU-R Recomendation P.838-3. Specific attenuation model for rain. Technical report, International Telecommunication Union, Geneve, Switzerland, 2005.

[31] ITU-R Recomendation P.839-4. Rain Height Model for Prediction Methods. Technical report, International Telecommunication Union, Geneve, Switzerland, 2013.

[32] ITU-R Recomendation P.841-5. Conversion of annual statistics to worst-month statistics. Technical report, International Telecommunication Union, Geneve, Switzerland, 2016.

[33] ITU-R Recomendation P.1144-9. Guide to the application of the propagation methods of Radiocommunication Study Group 3. Technical report, International Telecommunication Union, Geneve, Switzerland, 2017.

[34] ITU-R Recomendation P.1510-1. Mean surface temperature. Technical report, International Telecommunication Union, Geneve, Switzerland, 2017.

[35] ITU-R Recomendation P.1511-1. Topography for Earth-space propagation modelling. Technical report, International Telecommunication Union, Geneve, Switzerland, 2015.

[36] S. H. Lin. Statistical Behavior of Rain Attenuation. *Bell Syst. Tech. J.*, 52(4):557–581, 1973.

[37] Torleiv Maseng and Petter M. Bakken. A Stochastic Dynamic Model of Rain Attenuation. *IEEE Trans. Commun.*, 29(5):660–669, 1981.

[38] ITU-R Recommendation P.1853-1. Tropospheric Attenuation Time Series. Technical Report February, International Telecommunication Union, Geneve, Switzerland, 2012.

[39] ITU-R Recommendation P.1057-6. Probability distributions relevant to radiowave propagation modelling. Technical Report August, International Telecommunication Union, Geneve, Switzerland, 2019.

[40] Edwin Fernando Rojas, Laura Poveda, and Nicolás Grimblatt. Estado de la Banda Ancha en América Latina y el Caribe. Technical report, United Nations, Santiago, Chile, 2016.

[41] ITU and UNESCO. The State of Broadband 2016: Broadband catalyzing sustainable development. Technical Report September, International Telecommunication Union, ITU, Geneve, Switzerland, 2016.

[42] SATNEWS. SatMagazine: Special SmallSat Symposium. *SATNEWS*, 17(February):39–44, feb 2019.

[43] CISCO. Cisco Visual Networking Index: Forecast Methodology, 2016–2021. *White Pap.*, .(June):1–17, 2017.

[44] CISCO. The Zettabyte Era: Trends and Analysis. *White Pap.*, .(May):1–29, 2015.

[45] 5G AMERICAS. Spectrum Recommendations for the U.S. Technical report, 5G Americas, 2018.

[46] DTVE. Industry Survey 2018. Technical Report February, Digital TV Europe, London, 2018.

[47] BMI Research. Latin America Investment Opportunities In Telecoms : Risk / Reward Analysis. Technical report, BMI Research, London, 2018.

[48] VIA SATELLITE. Space 2.0: Taking AI Far Out. Technical Report December, Via Satellite, Rockville, MD - US, 2019.

[49] Andres Cornejo and Salvador Landeros. Simulation Model and Comparison for Satellite Links in Ku and Ka Bands for Standards-based on DVB-S2 and NS3. *IEEE Lat. Am. Trans.*, 14(4):1689–1697, apr 2016.

[50] Louis Ippolito. *Satellite Communications Systems Engineering*. John Wiley & Sons, Ltd, Chichester, UK, sep 2008.

[51] ITU-R Recommendation P.676-12. Attenuation by atmospheric gases and related effects. Technical report, International Telecommunication Union, Geneve, Switzerland, 2019.

[52] ITU-R Recommendation P.834-9. Effects of tropospheric refraction on radiowave propagation. Technical report, International Telecommunication Union, Geneve, Switzerland, 2017.

[53] ITU-R Recommendation P.840-8. Attenuation due to clouds and fog. Technical report, International Telecommunication Union, Geneve, Switzerland, 2019.

[54] R. Gallager. Low-density parity-check codes. *IEEE Trans. Inf. Theory*, 8(1):21–28, jan 1962.

[55] Sarah J Johnson. Introducing Low Density Parity Check (LDPC) Codes. Technical Report October, The University of Newcastle, Australia, 2015.

[56] EN ETSI. Digital Video Broadcasting (DVB); modulation systems for Broadcasting , other broadband satellite applications (DVB-S2). Technical report, European Telecommunications Standards Institute (ETSI), France, 2009.

[57] Claude Berrou and Alain Glavieux. Near optimum error correcting coding and decoding: Turbo-codes. *IEEE Trans. Commun.*, 44(9):1261–1271, 1996.

[58] Dirk P. Kroese, Tim Brereton, Thomas Taimre, and Zdravko I. Botev. Why the Monte Carlo method is so important today. *Wiley Interdiscip. Rev. Comput. Stat.*, 6(6):386–392, 2014.

[59] S.K. Rao. Design and analysis of multiple-beam reflector antennas. *IEEE Antennas Propag. Mag.*, 41(4):53–59, 1999.

[60] W. Stutzman and M. Terada. Design of offset-parabolic-reflector antennas for low cross-pol and low sidelobes. *IEEE Antennas Propag. Mag.*, 35(6):46–49, dec 1993.

[61] Thomas A. Milligan. *Modern Antenna Design*. John Wiley & Sons, Inc., Hoboken, NJ, USA, jun 2005.

[62] Dimitri Serrano-Velarde, Emmanuel Lance, Hector Fenech, and Georges E. Rodriguez-Guisantes. Novel dimensioning method for high-throughput satellites: Forward link. *IEEE Trans. Aerosp. Electron. Syst.*, 50(3):2146–2163, 2014.

[63] Warren L. Stutzman and Gary A. Thiele. *Antenna Theory and Design.* John Wiley & Sons., Blacksburg, Virginia, US, 3rd edition, 1998.

[64] Erich Lutz, Markus Werner, and Axel Jahn. *Satellite Systems for Personal and Broadband Communications.* Springer Berlin Heidelberg, Berlin, Heidelberg, 2000.

[65] D. Tipper. Fundamentals of Cellular Networks. University of Pittsburgh, available at: http://www.pitt.edu/~dtipper/2720/2720_Slides4.pdf, 2018.

[66] ITU-R Recommendation S.1328-4. Satellite system characteristics to be considered in frequency sharing analyses within the fixed-satellite service ANNEX 1. Technical report, International Telecommunication Union, Geneve, Switzerland, 2002.

[67] TICRA. GRASP: Analysis and Design of Reflector Antennas. Trial Version. Available at: http://www.ticra.com/software/grasp. Copenhagen, Denmark, 2020.

[68] Pantelis-Daniel Arapoglou, Konstantinos P. Liolis, and Athanasios D. Panagopoulos. Railway satellite channel at Ku band and above: Composite dynamic modeling for the design of fade mitigation techniques. *Int. J. Satell. Commun. Netw.*, 30(1):1–17, jan 2012.

[69] Georgios A. Karagiannis, Athanasios D. Panagopoulos, and John D. Kanellopoulos. Multidimensional rain attenuation stochastic dynamic modeling: Application to earth-space diversity systems. *IEEE Trans. Antennas Propag.*, 60(11):5400–5411, 2012.

[70] O. Koudelka, M. Schmidt, and J. Ebert. Design of a 40/50 GHz satellite ground station for fade mitigation experiments. *Acta Astronaut.*, 86:68–76, 2013.

[71] Tommaso Rossi, Mauro De Sanctis, and Fabio Maggio. Evaluation of outage probability for satellite systems exploiting smart gateway configurations. *IEEE Commun. Lett.*, 21(7):1541–1544, 2017.

[72] Tomaso De Cola and Maurizio Mongelli. Adaptive Time Window Linear Regression for Outage Prediction in Q/V Band Satellite Systems. *IEEE Wirel. Commun. Lett.*, 7(5):808–811, 2018.

[73] Nicolas Jeannin, Laurent Castanet, Isabelle Dahman, Vivien Pourret, and Béatrice Pouponneau. Smart gateways switching control algorithms based on tropospheric propagation forecasts. *Int. J. Satell. Commun. Netw.*, 37(1):43–55, 2019.

[74] D.G. Sweeney and C.W. Bostian. Implementing adaptive power control as a 30/20-GHz fade countermeasure. *IEEE Trans. Antennas Propag.*, 47(1):40–46, 1999.

[75] K. Kastamonitis, B. Gremont, and M. Filip. Short-term prediction of rain attenuation based on fade slope. *Electron. Lett.*, 39(8):687, 2003.

[76] Y. Vasavada, Y. Liu, J. Sanchez, P. Kapoor, Y. Antia, J. Rozmaryn, and J. Border. An Uplink Power Control driven compensation of wideband, semi-static, rain or interference induced link impairments affecting satellite feeder links operating at Ka band and above. In *MILCOM 2016 - 2016 IEEE Mil. Commun. Conf.*, pages 373–378. IEEE, nov 2016.

[77] Sepp Hochreiter and Jürgen Schmidhuber. Long Short-Term Memory. *Neural Comput.*, 9(8):1735–1780, nov 1997.

[78] Steven Elsworth and Stefan Güttel. Time Series Forecasting Using LSTM Networks: A Symbolic Approach. *ArXiv*, 1(2003.05672):1–12, 2020.

[79] Alex Sherstinsky. Fundamentals of Recurrent Neural Network (RNN) and Long Short-Term Memory (LSTM) network. *Phys. D Nonlinear Phenom.*, 404(March):1–43, 2020.

[80] The Mathworks. Introducing Machine Learning. Technical Report January 2016, The MathWorks, Inc., Natick, Massachusetts, USA, 2016.

[81] Keras. Dense layer. https://keras.io/api/layers/core_layers/dense/, 2020.

[82] Martin T. Hagan, Howard B. Demuth, Mark H. Beale, and Orlando De Jesus. *Neural Network Design*. Oklahoma State University, Stillwater, OK, United States, Stillwater, OK, 2nd editio edition, sep 2014.

[83] Simon Haykin. *Neural Networks and Learning Machines*. McMaster University, Hamilton, Ontario, Canada, 3rd edition, 2009.

[84] Kevin P Murphy. *Machine Learning: A Probabilistic Perspective*. The MIT Press, Cambridge, Massachusetts, 1st edition, 2012.

[85] Keras. Layer activation functions. https://keras.io/api/layers/activations/, 2020.

[86] Günter Klambauer, Thomas Unterthiner, Andreas Mayr, and Sepp Hochreiter. Self-normalizing neural networks. *Adv. Neural Inf. Process. Syst.*, 2017-Decem(12):972–981, 2017.

[87] Diederik P. Kingma and Jimmy Ba. Adam: A Method for Stochastic Optimization. In *3rd Int. Conf. Learn. Represent.*, pages 1–15, San Diego, CA, USA, dec 2015.

[88] Gábor Petneházi. Recurrent Neural Networks for Time Series Forecasting. *Handb. Nat. Comput.*, 1-4:461–477, dec 2018.

[89] Rob J. Hyndman and Anne B. Koehler. Another look at measures of forecast accuracy. *Int. J. Forecast.*, 22(4):679–688, oct 2006.

[90] John O. Rawlings, Sastry G. Pantula, and David A. Dickey. *Applied Regression Analysis*. Springer Texts in Statistics. Springer-Verlag, New York, may 1998.

[91] M. C. Peel, B. L. Finlayson, and T. A. McMahon. Updated world map of the Köppen-Geiger climate classification. *Hydrol. Earth Syst. Sci.*, 11(5):1633–1644, 2007.

[92] Roger G. Barry. *Atmosphere, Weather and Climate*. Routledge, London, 1st editio edition, oct 2009.

[93] S. Poornima and M. Pushpalatha. Prediction of rainfall using intensified LSTM based recurrent Neural Network with Weighted Linear Units. *Atmosphere (Basel).*, 10(11):1–18, 2019.

[94] Dhaval P. Patel, Mitul M. Patel, and Devendra R. Patel. Implementation of ARIMA model to predict Rain Attenuation for Ku-band 12 Ghz Frequency. *IOSR J. Electron. Commun. Eng.*, 9(1):83–87, 2014.

[95] Yan Jun Puah, Yuk Feng Huang, Kuan Chin Chua, and Teang Shui Lee. River catchment rainfall series analysis using additive holt–Winters method. *J. Earth Syst. Sci.*, 125(2):269–283, 2016.

[96] Ricardo Aguasca-Colomo, Dagoberto Castellanos-Nieves, and Máximo Méndez. Comparative analysis of rainfall prediction models using machine learning in islands with complex orography: Tenerife Island. *Appl. Sci.*, 9(22):1–17, 2019.

[97] Riccardo De Gaudenzi, Emiliano Re, and Piero Angeletti. Smart Gateways Concepts for High-Capacity Multi-beam Networks. In *30th AIAA Int. Commun. Satell. Syst. Conf.*, pages 1–18, Reston, Virigina, sep 2012. American Institute of Aeronautics and Astronautics.

[98] Hong Chuan Yang and Mohamed Slim Alouini. Markov chains and performance comparison of switched diversity systems. *IEEE Trans. Commun.*, 52(7):1113–1125, 2004.

[99] Jiahao Yang, Wenkai Zhang, Mingchuan Yang, and Yanyong Su. A New Gateway Switching Strategy in Q/V Band High Throughput Satellite Communication Systems Feeder Links. In Weixiao Meng, editor, *10th EAI Int. Conf. WiSATS 2019, Part II*, pages 506–514, Harbin, China, 2019. Springer.

[100] Zhuoming Li, Huiyun Xia, Yu Zhang, Junqing Qi, Shaohua Wu, and Shushi Gu. Multi-objective network optimization combining topology and routing algorithms in multi-layered satellite networks. *Sci. China Inf. Sci.*, 61(8):1–3, 2018.

[101] Roberto Nebuloni, Carlo Riva, Lorenzo Luini, Tommaso Rossi, Mauro De Sanctis, Marina Ruggieri, Giuseppe Codispoti, and Giorgia Parca. Optimization of Q/V-band Smart Gateway Switching in the framework of Q/V-Lift Project. *IEEE Aerosp. Conf. Proc.*, 2019-March:1–8, 2019.

[102] Rohani Hoda and Roosta Azad Kamali. Calculating Total System Availability. Technical report, KLM-Air France, 2014.

[103] Andres Cornejo, Salvador Landeros-Ayala, Ramon Martinez, and Jose M Matias. Analysis to Quantify and Optimize Spot Beams for a High Throughput Satellite in Ka and Q/V Bands. *IEEE Lat. Am. Trans.*, 17(02):219–227, feb 2019.

[104] Andres Cornejo, Salvador Landeros-Ayala, Ramon Martínez Rodríguez-Osorio, and Jose M Matias. A method for designing an offset-parabolic-reflector antenna for a ultra-high throughput satellite. In *Rev. Tecnol. e Inf.*, volume 16, pages 84–87, Lima, Peru, 2018. Universidad Inca Garcilaso de la Vega.

[105] Andres Cornejo, Salvador Landeros-Ayala, Ramon Martinez-Rodriguez, and Jose M Matias. Interference Evaluations in Frequency Reuse by Using Offset-Parabolic-Reflector Antennas for a UHTS System. *Int. J. Eng. Sci.*, 7(8):34–45, 2018.

[106] Andres Cornejo, Salvador Landeros-Ayala, Ramon Martinez Rodriguez-Osorio, and Jose Maria Matias. Optimization of the Ground Segment for an UHTS System through Neural Networks. In *XXXIII Simp. Nac. la Unión Científica Int. Radio (URSI 2018)*, pages 1–5, Granada, Spain, 2018.

[107] Andres Cornejo, Salvador Landeros-Ayala, Jose M. Matias, and Ramon Martinez. Applying Learning Methods to Optimize the Ground Segment for HTS Systems. *2020 IEEE 11th Lat. Am. Symp. Circuits Syst. LASCAS 2020*, pages 1–4, 2020.

[108] Andres Cornejo, Flor Ortiz-Gomez, Jose M. Matias, Ramon Martinez, and Miguel Salas-Natera. Quantum Cryptography for Satellite Communication Systems. In *Congr. Nac. Act. Espac. 2020-Agencia Espac. Mex.*, Mexico City, 2020.

STATEMENT

The presented information in this thesis was obtained from several sources that were considered trustworthy and punctually consigned to the references. The nature of used information is strictly for academic research and disclosure, non-profit, or another characteristic. It has also been done the best effort to acknowledge data properly, opinions, and presented content in this work, so any mistakes or omissions can be totally involuntary.

Mexico City, November 2020

-

IVAN ANDRES CORNEJO GAIBOR